International Journal of Acoustics and Vibration

A quarterly publication of the International Institute of Acoustics and Vibration

Volume 18, Number 4, December 2013

EDITORIAL

ARTICLES

INFORMATION

Editor's Space

Statistical Analysis in Acoustics and Vibration

Statistics is an important field of mathematics. It is used to study the collection, analysis, and interpretation of experimental data. Acoustics and vibration data are essentially random in nature. Examples include the vibration and noise induced by tire-road interactions. Tire types and road surface conditions are all random variables. In addition, any experimental data inevitably contain environmental noise which is also random. Therefore, statistics is very commonly used in acoustics and vibration research in experimental design and data analysis. Some theoretical models have been developed, such as the statistical energy analysis (SEA) and random vibration. With the rapid development of computer technologies, many modern statistical tools, such as Monte Carlo simulation and functional ANOVA (analysis of variance), have also been frequently applied to acoustics and vibration problems.

Data are collected in experimental studies either from one system or a family of systems. In both cases, data can be classified as deterministic or random. Deterministic data can be modelled using explicit mathematical equations, while random data cannot. Some researchers, however, argue that deterministic data only exist in theory because there are always some uncertainties and variations in physical systems along with environmental and operational effects. Even changes in temperature may significantly alter measured noise and vibration levels. Therefore, statistics should be used to allow for these factors and their effects. As a matter of fact, some commonly used parameters in acoustics and vibration are based on statistics. For example, the audible human frequency range (20 Hz to 20 kHz), the hearing threshold (20 μPa), and allowable vibration levels for rotating and non-rotating machines, found in ISO standards, are all based on averages since there are considerable individual variations.

Data collected from a single system can also be treated as a random variable. As time goes by, wear and other changes may develop. Several statistical parameters from the time series analysis have been used in condition monitoring. The basic idea is that if one parameter has changed significantly over time, it may indicate some defects that have developed in the system. Setting alarm thresholds and making decisions require careful data analysis and tests of hypotheses. For example, in the last few decades, more than ten single-value statistical measures mostly based on even-order moments, including the RMS value, crest factor, and kurtosis, etc. have been proposed for damage detection of gear transmissions. Other time-series analysis tools such as ARMA (autoregressive moving averages) and correlation procedures are also commonly used to model acoustical and vibration signals.

Analyses in the frequency domain are often performed using time series. Two widely used spectral approaches use the power spectrum density (PSD) and bi-spectrum. A PSD uses the normalized power spectrum in order to remove the effects of the frequency interval. There are two main categories of PSD algorithms: (1) parametric methods, which are based on models such as ARMA and MUSIC (multiple signal classification), and (2) non-parametric methods, such as the periodogram and Welch methods. Unlike the PSD, which represents the power distribution (the second moment) of a signal, the bi-spectrum decomposes skewness (the third moment) of a time series over frequency. The bi-spectrum can detect asymmetric nonlinearities and thus is useful in vibration fault diagnosis.

Although a normal distribution may be the most assumed probability distribution in statistical modeling, one should be aware that it is not always the case. For example, the Weibull distribution has been applied very successfully in failure analysis even though the number of samples may be small. Additionally, it can be proven that Fourier spectra are random variables following an exponential distribution. Since the spectra are not normally distributed, the expected value is not suitable to characterize the signals. In a recent study, the minimum spectrum was chosen to characterize the signal and the statistics satisfied the Laplace distribution. Extensive computation efforts including Monte Carlo simulation have also been investigated.

A major challenge is the statistical inference of non-stationary vibration data as both the amplitudes and frequencies may vary with time. Statistical inference, also known as statistical induction, is a procedure used to draw conclusions from data sets which are affected by random variables. In such cases, the statistical properties are more localized in time. Also, the modeling requires an infinite number of parameters to account for time-varying properties. The statistical inferences may require new methods for dimension reduction, model selection and hypothesis tests. The SLEX (Smooth Localized Complex Exponentials) method may prove to be useful for non-stationary acoustics and vibration data analysis in the future.

Zhuang Li
Associate Professor,
McNeese State University, Louisiana, U.S.A.

Obituary Notice of Professor Zbigniew Witold Engel, 1933–2013

Zbigniew Witold Engel was born on April 1, 1933 in Zavady, near Zhovkva. He began his studies in 1952 in the Department of Technical Mechanics of the AGH University of Science and Technology (AGH-UST.) He obtained his PhD in 1962 and D.Sc. in 1966. He was granted the title of professor in 1977. Professor Engel held a number of responsible functions at the AGH-UST. For many years he was the Deputy Dean of the Faculty of Machines for Mining and Metallurgy, AGH-UST. Professor Engel also organized and directed the Institute of Mechanics and Vibroacoustics at AGH-UST, and then, later, he became the head of the Department of Mechanics and Vibroacoustics.

Professor Engel created a new discipline—vibroacoustics—during the 1960s and he is considered to be the founder of that discipline. Vibroacoustics unites the theory of vibrations of mechanical systems with the mechanics of acoustical phenomena in coupled mechanical-acoustic systems. Professor Engel formulated the basic ideas and objectives of vibroacoustics.

Professor Engel had more than 580 publications, including monographs, published lectures, textbooks, scientific papers, and presentations at conferences and symposia. Papers by or co-authored by Professor Engel include those on: mechanics, environmental protection against vibration and noise, basics of industrial vibroacoustics, methods for active noise control, noise-insulated enclosures, design guidelines for the use of barriers in industrial halls, vibroacoustics of machines, protection of the environment against noise, and fundamentals of acoustics of sacred buildings.

Professor Engel held 15 patents and a large number of unpublished works prepared for industry. A significant part of Professor Engel's work was related to education. He supervised 40 doctoral dissertations. Twelve of his colleagues received post-doctoral degrees, and many of them hold the title of professor. Professor Engel worked with many research centres in Poland and around the world, including those in Austria, Czech Republic, Denmark, Japan, Russia, Slovakia, the Ukraine and the USA.

Professor Engel was a member of many professional societies, including the Academy of Engineering in Poland, the New York Academy of Sciences, the St. Petersburg Academy of Sciences, the Institute of Noise Control Engineering, and the International Institute of Acoustics and Vibration (IIAV.) He was a past Director of the IIAV.

Professor Engel held honorary doctorates from the AGH-UST, the Krakov University of Technology, the Kielce University of Technology. He also held an honorary professorship of the Warsaw University of Technology. His many honours awards include the gold medal of the Krizik's Czechoslovak Academy of Science and the Hungarian "Pro Silentia." He also received the following Polish state awards: the Golden Cross of Merit, the Knight's Cross of the Order of Polonia Restituta, the Officer's Cross of the Order of Polonia Restituta, the Commande's Cross of the Order of Polonia Restituta, and the Medal of the National Education Commission.

He took part in the establishment of several scientific journals and served as the Editor-in-Chief of the AGH Mechanics. He was a member of the editorial boards of the Noise Control Engineering Journal, the Archives of Acoustics, the Occupational Safety and Ergonomics Journal, and the Dynamics of Machines.

Professor Engel actively participated in the organization of national and international congresses, conferences, and symposia. He was a member of the scientific committees of conferences and congresses including 13 Inter-Noise Congresses. He was the chair of the scientific committees of the Noise and Vibration in Transportation Conference in St. Petersburg in 2000, 2002, and 2004.

Professor Engel held several important positions, among them the Vice Chair of the Central Scientific Research and Higher Education (1989–1990), Chairman of the Committee of Acoustics of the Polish Academy of Sciences (2007–2011), and Chairman of the Commission of Applied Mechanics of Krakov Department of Polish Academy of Sciences. Professor Engel was also the initiator and organizer of the construction of the vibroacoustic laboratories at AGH-UST. Thanks to his efforts, these unique laboratories possess reverberation and anechoic chambers and the latest equipment.

Professor Engel was the initiator and one of the main founders of the Engel Family Foundation, which, among others, grants awards to young scientists under the age of 35 for outstanding achievements in basic research.

Professor Zbigniew Witold Engel was a distinguished scholar, teacher, academic, educator, and organizer. The prominent role he played for the development of Polish science earned him a national and international reputation.

A Two-Stage Adaptive Algorithm in the Frequency Domain for a Multichannel Feedforward Active Noise Control System

Min Zhu[†]

Computer Center, East China Normal University, Zhongshan North Rd., Shanghai, 200062, P.R. China
System Science and Technology, Akita Prefectural University, Yurihonjo, 015-0055, Japan

Huigang Wang

College of Marine, Northwestern Polytechnical University, Xi'an, Shaanxi, 710072, P.R. China
System Science and Technology, Akita Prefectural University, Yurihonjo, 015-0055, Japan

Guoyue Chen

System Science and Technology, Akita Prefectural University, Yurihonjo, 015-0055, Japan

Kenji Muto

College of Engineering, Shibaura Institute of Technology, Tokyo, 135-8548, Japan

The reference paths between original sources and reference sensors in multichannel feedforward active noise control (ANC) systems are often ignored by most ANC algorithms. Therefore, a two-stage adaptive algorithm in the frequency domain is proposed to deal with several of the more complicated cases, specifically addressing instances when the reference sensors must be placed far away from the noise sources. This two-stage system includes a blind pre-processing system cascaded with a traditional MFxLMS system; both systems operate in the frequency domain. The new algorithm can eliminate the effect of reference paths by performing blind pre-processing independently. The MFxLMS algorithm in the following stage can achieve faster convergence than the traditional algorithm without blind pre-processing. The computational complexity of the proposed algorithm is analysed and a numerical simulation using impulse responses measured in a real reverberant room is performed to verify the convergence performance of the proposed algorithm.

1. INTRODUCTION

Multichannel feedforward active noise control (ANC) systems have many potential applications in aircrafts, engines, and mechanics. Many successful algorithms, such as the multichannel filtered-x LMS (MFxLMS) algorithm, have been developed; these algorithms are summarized in the work of Elliot,[1] and Haykin.[2] The convergence performance of the MFxLMS algorithm, however, is limited by the properties of the reference signals and the structure of the secondary paths, phenomena that have been analysed in past work.[3–7] Most multichannel ANC algorithms operate in the time domain; however, their computational complexity appears to increase with the length of the controller. A fast and efficient MFxLMS algorithm that operates in the frequency domain is also desirable and some block filter-x LMS algorithms for single channel or multichannel systems have been proposed to improve the computational efficiency of ANC systems with fast Fourier transform (FFT).[14–16]

Most existing algorithms are focused on the online or offline modelling and estimation of secondary paths; however, reference paths between the original sources and the reference sensors are often ignored because the reference sensors are assumed to be located close to the original noise sources. In many practical applications, the reference sensors cannot be placed close to the original noise sources because of physical environmental limitations. Therefore, because of the lack of reference paths, the data received by the reference sensors has a high correlation each other. A simple example can be used to explain the effect of the reference paths. If all of the original sources are uncorrelated noise, the data received by the reference sensors will be the combination of the original noise sources via their respective reference paths. Thus, the correlation properties of the reference signals are completely determined by the reference paths. A detailed theoretical analysis of the effect of reference paths and secondary paths on the performance of the MFxLMS algorithm in the frequency domain was presented in our previous paper.[9]

Elliott[8] proposed an optimal controller in the frequency domain to improve the MFxLMS convergence by including prior information about the reference signals—namely, the cross
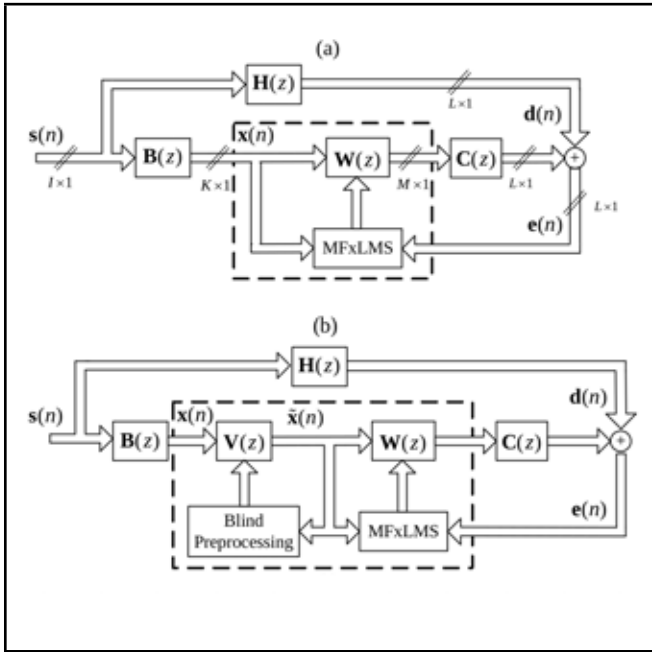
Figure 1. A block diagram of a multichannel ANC system based on (a) the standard MFxLMS algorithm, and (b) the proposed two-stage adaptive algorithm.

spectral density matrix of the reference signals—but this information was difficult to obtain in a time-varying environment or for non-stationary noise sources. Chen et al.[9] analysed the structure of the correlation matrix of the filtered reference signals in the MFxLMS algorithm and pointed out that the reference paths had the same effect on the MFxLMS algorithm as the secondary paths. An adaptive blind pre-processing method for the reference signals in the time domain was proposed to eliminate the effect of the reference paths and improve the performance of the following MFxLMS algorithm.[10]

In this paper, a two-stage adaptive algorithm operating in the frequency domain is proposed to address the difficulties of a complicated multichannel ANC system. Because the reference paths and primary paths will be simple for periodic noise sources, only broadband uncorrelated random noise sources are considered in this study. In our two-stage system, a new adaptive algorithm is added between the reference signals and the traditional MFxLMS algorithm, and the outputs of the first stage are expected to recover the original uncorrelated noise sources. In the second stage, the recovered noise sources become the inputs of the MFxLMS algorithm and the effect of the reference paths on the MFxLMS algorithm is eliminated. To improve the computational efficiency of our system, both filtering operation and coefficient updating are performed in the frequency domain.

The structure of this paper is as follows. In section two, our two-stage model and the optimal solution for the multichannel ANC system are introduced. Each stage of the adaptive algorithm in the frequency domain is then discussed in detail during section three, and a basic evaluation of the computational complexity of the two-stage system is presented in section four. Section five uses an example to show the convergence performance of the two-stage adaptive algorithm in the frequency domain, and conclusions are drawn in section six.

2. THE MODEL AND OPTIMAL SOLUTION FOR A MULTICHANNEL ANC SYSTEM

Figure 1(a) presents a multichannel ANC system with K reference sensors and L error sensors that receive signals from I noise sources via the reference path $\mathbf{B}(z)$ and the primary path $\mathbf{H}(z)$. The controller $\mathbf{W}(z)$ receives the reference signals as inputs, to control M loudspeakers and minimize noise. Such a system is referred to as $CASE[I, K, M, L]$. The filter $\mathbf{W}(z)$ of the controller is updated adaptively according to one specific algorithm, such as the MFxLMS algorithm.

Elliot[8] has analysed the performance of the MFxLMS algorithm in the frequency domain and given the optimal solution for the controller, which is

$$\mathbf{W}_{\text{opt}}(z) = - \left[\mathbf{C}^H(z)\mathbf{C}(z) \right]^{-1} \mathbf{C}^H(z)\mathbf{R}_{xd}(z)\mathbf{R}_{xx}^{-1}(z); \quad (1)$$

where $\mathbf{R}_{xx}(z)$ is the power spectral density matrix of the inputs, $\mathbf{R}_{xd}(z)$ is the cross spectral density matrix between the inputs and the desired data received by error sensors from noise sources, and $\mathbf{C}(z)$ is the secondary path from the microphones to the error sensors. If a causal constraint of $\mathbf{W}(z)$ is considered and the minimum phase decomposition of $\mathbf{C}(z)$ is

$$\mathbf{C}(z) = \mathbf{C}_{\text{all}}(z)\mathbf{C}_{\text{min}}(z); \quad (2)$$

while the spectral factorization of $\mathbf{R}_{xx}(z)$ is

$$\mathbf{R}_{xx}(z) = \mathbf{F}(z)\mathbf{F}^H(z); \quad (3)$$

the optimal controller in the frequency domain can be simplified as

$$\mathbf{W}_{\text{opt}}(z) = -\mathbf{C}_{\text{min}}^{-1}(z) \left[\mathbf{C}_{\text{all}}^T(z^{-1})\mathbf{R}_{xd}(z)\mathbf{F}^{-H}(z) \right]_+ \mathbf{F}^{-1}(z); \quad (4)$$

where $[\cdot]_+$ defines the z-transform of the causal parts of the quantity in brackets. $\mathbf{F}(z)$ is often called the shaping filter of $\mathbf{x}(n)$; the inverse filter matrix $\mathbf{F}^{-1}(z)$ is called the whitening filter.

In practice, the power spectral density matrix of inputs $\mathbf{R}_{xx}(z)$ is determined by two factors: the noise sources and the reference path $\mathbf{B}(z)$. Based on Fig. 1(a), $\mathbf{R}_{xx}(z)$ can be written simply as

$$\mathbf{R}_{xx}(z) = \mathbf{B}(z)\mathbf{R}_{ss}(z)\mathbf{B}^H(z); \quad (5)$$

which includes the power spectral density matrix of noise sources $\mathbf{s}(n)$ and the reference paths. For broadband uncorrelated noise sources, $\mathbf{R}_{ss}(z)$ can be approximated by a diagonal matrix, while $\mathbf{R}_{xx}(z)$ is completely dependent upon the reference path $\mathbf{B}(z)$. According to one analysis in the frequency domain proposed by Chen and Wang et al.,[9] the convergence properties of the traditional MFxLMS algorithm are completely determined by the cross spectral density matrix of the filtered reference signals, implying that the effect of the reference paths cannot be ignored. For a detailed theoretical analysis of the reference path to the ANC MFxLMS algorithm, readers are referred to Chen et al.'s work.[9]

The whitening filter matrix $\mathbf{F}^{-1}(z)$ of the optimal controller in Eq. (4) is essential to reducing the effect of the reference

path $\mathbf{B}(z)$. The reference signals filtered by $\mathbf{F}^{-1}(z)$ approximate the uncorrelated white noise, that is,

$$\mathbf{F}^{-1}(z)\mathbf{R}_{xx}(z)\mathbf{F}^{-H}(z) = \mathbf{I}. \tag{6}$$

There are many studies that describe offline and online secondary path modelling, but very few papers consider the estimation of $\mathbf{F}(z)$. If the power spectral density matrix of the inputs $\mathbf{R}_{xx}(z)$ is known for certain or can be estimated accurately based on the reference sensors, it is easy to estimate $\mathbf{F}(z)$ directly, using the spectral decomposition theorem. However, this method is impractical in time varying environments, for slowly moving noise sources, and for non-stationary inputs; therefore, an adaptive algorithm is preferred when estimating $\mathbf{F}(z)$.

A two-stage adaptive processing system is proposed to eliminate the effects of the reference paths on the following MFxLMS algorithm, as shown in Fig. 1(b). The difference between Figs. 1(a) and 1(b) is that a new blind adaptive algorithm is added between the reference signals and the traditional ANC algorithm. The new stage assumes that all noise sources are independent broadband noises. Based on this assumption, an adaptive algorithm is proposed to pre-process the reference signals to recover the original noise sources. Thus, the effect of the reference paths can be eliminated automatically. Because noise sources and the reference paths cannot be measured *a priori* (and may be time varying in some practical cases), a blind pre-processing adaptive algorithm is preferred. Each stage in the two-stage adaptive processing system has a different goal. The first stage is blind pre-processing of the reference sensor data $\mathbf{x}(n)$, which is the whitening filter $\mathbf{F}^{-1}(z)$. Therefore, the ideal outputs of the first stage, $\widetilde{\mathbf{x}}(n)$, recover the original noise sources. The next stage includes the traditional MFxLMS algorithm with the whitened signals, $\widetilde{\mathbf{x}}(n)$, as inputs. To improve the computational efficiency of the two-stage ANC system, both adaptive algorithms operate in the frequency domain.

3. THE TWO-STAGE ADAPTIVE ALGORITHMS IN THE FREQUENCY DOMAIN

3.1. The Blind Pre-Processing Algorithm in the First Stage

As stated above, either the noise sources or the reference path may be time varying, and certain information about sources and reference paths cannot be obtained in advance; therefore, the accurate estimation of $\mathbf{F}(\omega)$ is impossible, a situation that is called blind in ANC systems. Blind processing has been successfully applied to speech signal separation and biomedical signal processing.[11,12] The basic principle of blind processing requires the statistical independence assumption for noise sources, or some other special temporal or frequency structure of signals. Details about blind processing theory can be found in Cichocki and Amari's work.[13] In this study, we develop an adaptive blind pre-processing algorithm, in which the filter coefficients are updated in the frequency domain using FFT.

For broadband noise sources $\mathbf{s}(n)$, which are assumed to be independent from each other in most cases, the received signals $\mathbf{x}(n)$ at the reference sensors can be given by

$$\mathbf{x}(n) = [\mathbf{B}(z)]\mathbf{s}(n); \tag{7}$$

where $[\mathbf{B}(z)]$ is defined as the filtering operation in a system, with a transfer function $\mathbf{B}(z)$. The primary reason for using a blind pre-processing system is to design an order-Q FIR filter matrix $\mathbf{V}(z)$ for the reference data $\mathbf{x}(n)$ such that the outputs $\widetilde{\mathbf{x}}(n)$ approximate the original noise sources. The outputs of the blind pre-processing system in Fig. 1(b) are

$$\widetilde{\mathbf{x}}(n) = [\mathbf{V}(z)]\mathbf{x}(n) = \sum_{q=0}^{Q} \mathbf{V}_q(n)\mathbf{x}(n-q). \tag{8}$$

Because of the independence assumption regarding the original noise sources, the recovered outputs $\widetilde{\mathbf{x}}(n)$ can also be considered to be independent from each other. The common statistical independence measure of signals is the Kullback-Leibler divergence, which is the ratio of the joint probability density function (PDF), $p(\widetilde{\mathbf{x}}(n))$, to the product of each marginal PDF, $p_1(\widetilde{x}_1(n)) \ldots p_K(\widetilde{x}_K(n))$,

$$KL(\widetilde{\mathbf{x}}(n)) = \int p(\widetilde{\mathbf{x}}(n)) \ln \frac{p(\widetilde{\mathbf{x}}(n))}{p_1(\widetilde{x}_1(n)) \ldots p_K(\widetilde{x}_K(n))} d\widetilde{x}(n); \tag{9}$$

and $KL(\widetilde{\mathbf{x}}(n)) \geq 0$. It is equal to zero only if all of the components of $\widetilde{\mathbf{x}}(n)$ are independent. Minimizing $KL(\widetilde{\mathbf{x}}(n))$ will yield the optimal filter $\mathbf{V}(z)$, making the outputs $\widetilde{\mathbf{x}}(n)$ as independent as possible. Once exact minimization has been achieved, the covariance matrix of outputs $\widetilde{\mathbf{x}}(n)$

$$\mathbf{R}_{\widetilde{x}}(n) = E\{\widetilde{\mathbf{x}}(n)\widetilde{\mathbf{x}}^H(n)\} \approx \mathbf{I} \tag{10}$$

is diagonal approximately, which means that the final outputs are also whitened and independent. Comparing Eq. (6) to Eq. (10), we can see that the blind pre-processing system $\mathbf{V}(z)$ fills the same role as $\mathbf{F}^{-1}(z)$, and that the effect of the reference path $\mathbf{B}(z)$ can be eliminated completely.

Many adaptive and batch algorithms have been proposed to find the optimal filter matrix $\mathbf{V}(z)$ by minimizing KL divergence in Eq. (9), the most popular being the natural gradient algorithm by Amari,[13]

$$\mathbf{V}_q(n+1) = \mathbf{V}_q(n) + \mu \left[\mathbf{V}_q(n) - f(\widetilde{\mathbf{x}}(n))\mathbf{u}^T(n-q) \right];$$

$$\mathbf{u}(n) = \sum_{r=0}^{Q} \mathbf{V}_{Q-r}(n)\widetilde{\mathbf{x}}(n-r); \quad q = 0, \ldots, Q; \tag{11}$$

where the nonlinear function $f(\widetilde{x}) = -\partial \ln p(\widetilde{x})/\partial\widetilde{x}$ is called the score function of the PDF $p(\widetilde{x})$, and all noise sources are assumed to have the same distribution. The updating process for each filter coefficient is very simple, only requiring about four multiplication/addition operations per adaptive filter coefficient. However, the additional computation of $\mathbf{u}(n)$ costs the most computational time within the natural gradient algorithm in Eq. (11); therefore, a simple and efficient implementation of Eq. (11) in the frequency domain with fast Fourier transform (FFT) is desirable.

The algorithm in Eq. (11) computes the optimal filter coefficients iteratively, sample by sample, and the computational efficiency is very low. To save computational time with the help of the FFT, a block adaptive algorithm of Eq. (11) is required. Redefining the $K(Q+1)$ input signal column vector

$$\mathbf{\underline{x}}(n) = \left[\mathbf{x}^T(n) \cdots \mathbf{x}^T(n-Q)\right]^T; \qquad (12)$$

and the $K \times K(Q+1)$ filter coefficient matrix

$$\mathbf{\underline{V}}(n) = [\mathbf{V}_0(n) \cdots \mathbf{V}_Q(n)]; \qquad (13)$$

we can rewrite the output of the blind pre-processing in Eq. (8) as

$$\widetilde{\mathbf{x}}(n) = \mathbf{\underline{V}}(n)\mathbf{\underline{x}}(n). \qquad (14)$$

The natural gradient algorithm in Eq. (11) can also be expressed, in a more compact form, as

$$\mathbf{\underline{V}}(n+1) = (1+\mu)\mathbf{\underline{V}}(n) - \mu f(\widetilde{\mathbf{x}}(n))\mathbf{\underline{u}}^T(n); \qquad (15)$$

where the $K(Q+1)$ temporary vector $\mathbf{\underline{u}}(n)$ is defined as

$$\widetilde{\mathbf{u}}(n) = \mathbf{\underline{R}}(n)\mathbf{\underline{x}}(n). \qquad (16)$$

The $K(Q+1) \times K(Q+1)$ block Toeplitz symmetric matrix $\mathbf{\underline{R}}(n)$ is

$$\mathbf{\underline{R}}(n) = \text{toeplitz}\left([\mathbf{R}_0(n) \cdots \mathbf{R}_L(n)]\right); \qquad (17)$$

where $\text{toeplitz}[\mathbf{c}]$ denotes a symmetric Toeplitz matrix containing the vector or matrix $\mathbf{c}$. Each value of $\mathbf{R}_q(n)$, $q = 0, 1, \ldots, Q$ is related to the geometric manifold and is defined as

$$\mathbf{R}_q(n) = \sum_{l=0}^{Q} \mathbf{V}_p^T(n)\mathbf{V}_{p+l}(n); \quad q = 0, 1, \ldots, Q. \qquad (18)$$

The block-based implementation of this algorithm assumes that the filter matrix $\mathbf{\underline{V}}(n)$ for each block is fixed and is only updated at the end of the block based on

$$\mathbf{\underline{V}}(n+N+1) = (1+\mu)\mathbf{\underline{V}}(n) - \mu \sum_{l=0}^{N-1} f(\widetilde{\mathbf{x}}(n+l))\mathbf{\underline{u}}^T(n+l); \qquad (19)$$

where N is the block length, which is generally greater than or equal to the filter length L. It is noteworthy that the filter matrix $\mathbf{\underline{V}}(n)$ is fixed for each data block, meaning the sequence $\mathbf{R}_q(n)$, $q = 0, 1, \ldots, Q$ is also updated once for each data block.

Because there is a linear convolution in Eqs. (14) and (16), and the linear correlation in Eqs. (18) and (19) can be computed efficiently using the FFT, the block-based algorithm in Eq. (19) can be implemented efficiently in the frequency domain. The $2N$-points FFT and the overlap-save method are used, but the detailed derivation and the pseudo code for fast implementation are not shown here.

It is noteworthy that the fast implementation of Eq. (19) using the FFT is different from the blind deconvolution algorithm in the frequency domain, where all inputs are first transformed into the frequency domain and then blind processing is employed in each frequency bin, whereas the fast implementation of Eq. (19) only improves the computational efficiency of linear convolution and correlation with FFT. The filter coefficients are updated in the time domain.

3.2. The MFxLMS Algorithm in the Frequency Domain

The MFxLMS algorithm has been analysed by many researchers. The updating of the controller coefficients at the k-th data block for $CASE[I, K, M, L]$ can be expressed in the frequency domain as

$$\mathbf{e}(\omega, k) = \mathbf{d}(\omega, k) - \mathbf{U}(\omega, k)\mathbf{w}(\omega, k);$$
$$\mathbf{w}(\omega, k+1) = \mathbf{w}(\omega, k) - \mu_1 \mathbf{U}^H(\omega, k)\mathbf{e}(\omega, k); \qquad (20)$$

where the superscript H denotes the Hermitian transpose, and μ_1 is the fixed step size. $\mathbf{e}(\omega, k)$ and $\mathbf{d}(\omega, k)$ are the transformed vector of the $L \times 1$ error vector $\mathbf{e}(n)$ and the desired vector $\mathbf{d}(n)$ for the k-th data block, respectively. $\mathbf{w}(\omega, k)$ is the transformed vector of the controller $MK \times 1$ vector with FFT

$$\mathbf{w}(n) = [w_{11}(n) \cdots w_{M1}(n) \cdots w_{MK}(n)]^T.$$

$\mathbf{U}(\omega, k)$ is the $L \times MK$ filtered reference matrix for the k-th block, and can be written as

$$\mathbf{U}(\omega, k) = \widetilde{\mathbf{x}}^T(\omega, k) \otimes \hat{\mathbf{C}}(\omega); \qquad (21)$$

where $\otimes$ is the Kronecker product, and $\hat{\mathbf{C}}(\omega)$ is the $L \times M$ estimated secondary path matrix from loudspeakers to error sensors.

4. EVALUATION OF THE COMPUTATIONAL COMPLEXITY

The difference between our proposed algorithm and a traditional MFxLMS algorithm is that the traditional ANC controller is replaced by a new processing system, which is a cascade of two independent adaptive systems, as shown in the dashed frame in Fig. 1. Essentially, the two-stage system is more complicated than the traditional one because of the additional filtering operations required; however, the new two-stage system can improve the convergence of the entire ANC system at the cost of only a small amount of additional computational load, especially in broadband multichannel ANC systems. As stated,[9] the convergence speed of the MFxLMS algorithm is determined by the eigenvalue spread of $\mathbf{R}(\omega)$, and the correlation matrix of the filtered reference signals in the frequency domain,

$$\mathbf{R}(\omega) = [\mathbf{B}^H(\omega)\mathbf{B}(\omega)]^*[\hat{\mathbf{C}}^H(\omega)\hat{\mathbf{C}}(\omega)]. \qquad (22)$$

A large eigenvalue spread in Eq. (22) will result in long convergence time. The existence of the reference path $\mathbf{B}(\omega)$ will increase the eigenvalue spread of $\mathbf{R}(\omega)$. If the effect of the reference path $\mathbf{B}(\omega)$ can be eliminated by blind pre-processing, the convergence speed of the MFxLMS algorithm in the two-stage system will only be dependent upon the estimated secondary paths, and the convergence speed of the MFxLMS algorithm in the second stage will increase.

If two FFTs in the two-stage system have the same length $2N$, the outputs of the first stage in the frequency domain can be the direct inputs of the second stage; thus, the two stages can
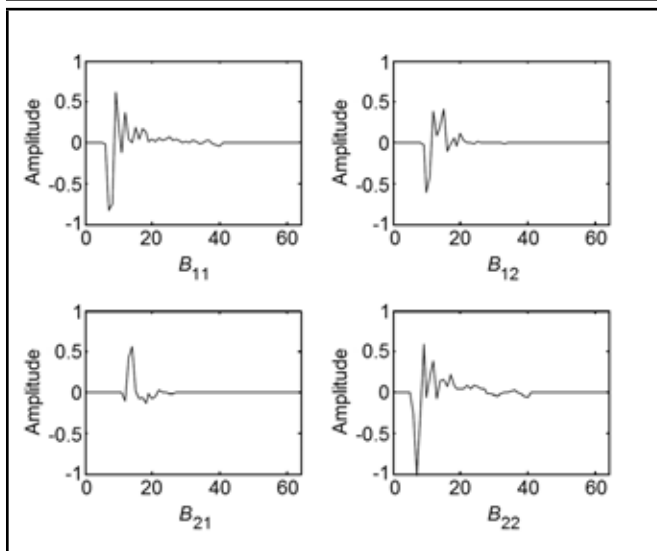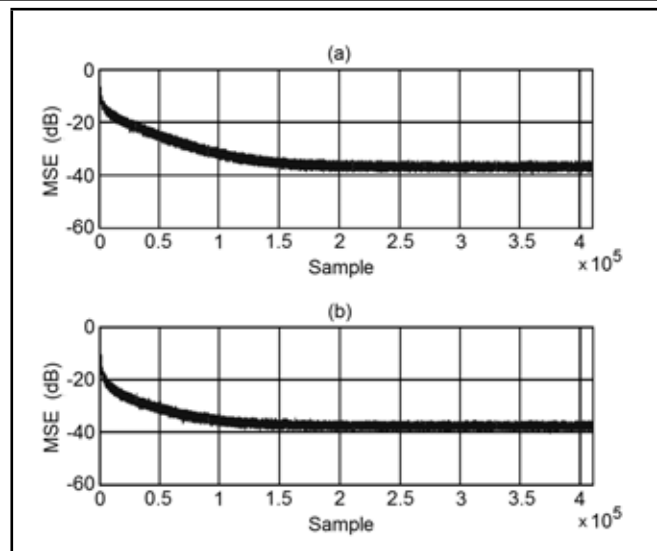
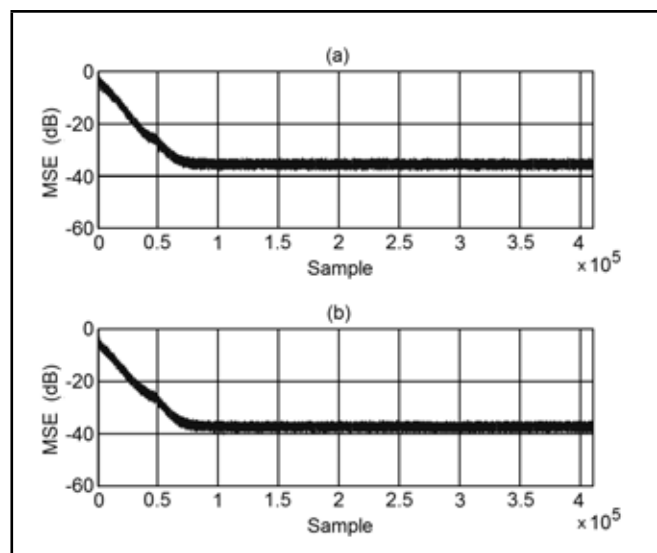**Figure 2.** Four measured reference path responses in a reverberant room with a sampling rate of 2 kHz.
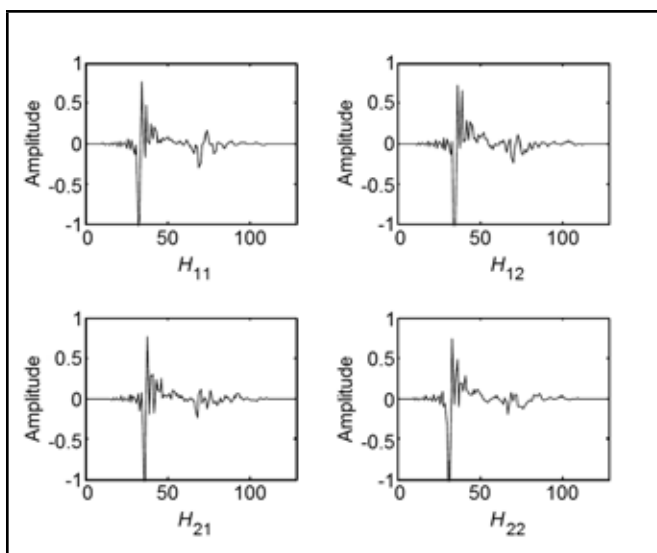
Figure 3. Four measured primary path responses in a reverberant room with a sampling rate of 2 kHz.

Figure 4. The convergence curve of the traditional MFxLMS algorithm in the frequency domain for two error sensors over a 100-iteration average.

Figure 5. The convergence curve of two-stage adaptive algorithm in the frequency domain for two error sensors over a 100-iteration average.

be cascaded, which reduces the complexity. The complexity of the blind pre-processing algorithm in the frequency domain has been analysed by Douglas et al.[12] This algorithm requires $4K^2 + 3K$ FFTs of length $2N$ and $1.5K^3 + 3.5K^2$ number of $2N$ point complex multiplications. If the two stages can be cascaded and the two FFTs can be reduced, there will be only $4K^2 + K$ additional FFTs in the cascaded system in Fig. 1(b). The computational complexity of the traditional MFxLMS algorithm in the frequency domain includes $K + M + 2KM + ML + L$ FFTs of length $2N$, and $KM + 2KML$ number of $2N$ point complex multiplications, which are simplified into $3K^2 + 3K$ FFTs and $2K^3 + K$ number of $2N$ point complex multiplication for a simple $CASE[K, K, K, K]$. Blind pre-processing has approximately the same complexity as the MFxLMS algorithm if an FFT with the same length is used; however, the complexity of the entire two-stage adaptive algorithm is twice that of the traditional MFxLMS algorithm.

5. NUMERICAL SIMULATIONS

A simple numerical computer simulation of $CASE[2, 2, 2, 2]$ is used to show the difference between the traditional MFxLMS algorithm and our two-stage adaptive algorithm in the frequency domain. Four measured impulse responses in a reverberant room with a sampling rate of 2 kHz are shown in Fig. 2, which are the reference path responses, and another four impulse responses shown in Fig. 3, are the primary path responses. The physical system layout for measurement of these room impulses is presented in Chen and Muto's work.[4] Because we are more concerned with reference path responses, a simple secondary path model is employed as

$$\mathbf{C}(:, 1, 1) = [0.5; 0.4; 0.1]; \quad \mathbf{C}(:, 2, 2) = [0.5; 0.4; 0.1];$$
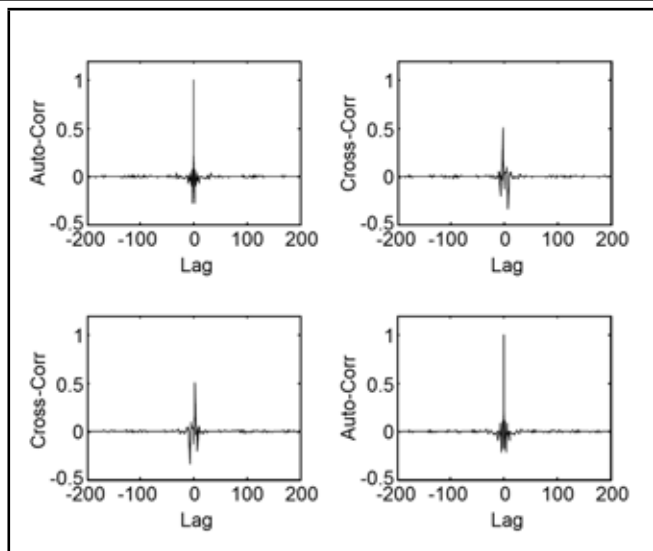(23)

the estimated secondary paths are accurate when $\hat{\mathbf{C}} = 0.95\mathbf{C}$. This model assumes that microphones are located near error sensors and that no cross secondary paths exist.

In the traditional multichannel ANC system shown in
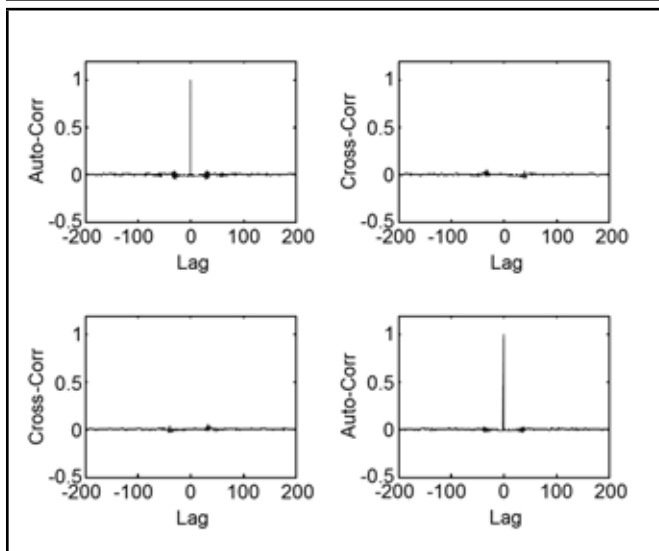
Figure 6. Normalized auto- and cross-correlation of outputs of blind pre-processing after convergence.


Figure 7. Normalized auto- and cross-correlation at the reference sensors before blind pre-processing.

Fig. 1(a), the controller length is 128; an additional 2×2 filter matrix with a length of $Q = 64$ is included in the two-stage ANC system in Fig. 1(b). A 256-point FFT and $\mu_1 = 0.0003$ are used for both algorithms. In this simulation, the two noise sources are uniform white noises with unit variance, the number of samples is 409600, and both algorithms are run 100 times to compute the averaged mean square error (MSE) of $e(n)$. The nonlinear function in Eq. (11) is $f(x) = x^3$, which is suitable for sub-Gaussian random signals such as uniform white noise. The MSE of the traditional MFxLMS algorithm and the two-stage adaptive algorithm for two error sensors are plotted in Figs. 4 and 5, respectively. The convergence speed of the two-stage algorithm is higher than that of the traditional MFxLMS algorithm, and both algorithms can obtain approximately the same final MSE.

To check the ability of blind pre-processing to eliminate the reference paths, the normalized auto-correlation and cross-correlation of $\widetilde{\mathbf{x}}(n)$ after convergence are given in Fig. 6, where $\widetilde{\mathbf{x}}(n)$ is whitened and the signals are uncorrelated to each other. For comparison, the corresponding correlation results of the reference signals before blind pre-processing are also shown in Fig. 7. Because the original noise sources are assumed to be independent white noise sources, the reference signals are completely dependent upon the reference paths $\mathbf{B}(z)$ from Eq. (5); therefore, the auto- and cross-correlation of the reference signals in Fig. 7 represent the effect of the reference paths $\mathbf{B}(z)$. From Fig. 6, we can see that the recovered outputs of blind processing can approximate the original noise sources and the effect of $\mathbf{B}(z)$ has been eliminated completely. This comparison can explain why the two-stage algorithm has faster convergence than the traditional MFxLMS algorithm.

An obvious advantage of using the two-stage MFxLMS algorithm in the frequency domain is that it has low computational complexity. Keeping the simulation conditions the same as those described above, but using the blind pre-processing filter and the traditional MFxLMS algorithm with the same length (which varies to 2048 from 32), the traditional MFxLMS algorithm with blind pre-processing in the time do-
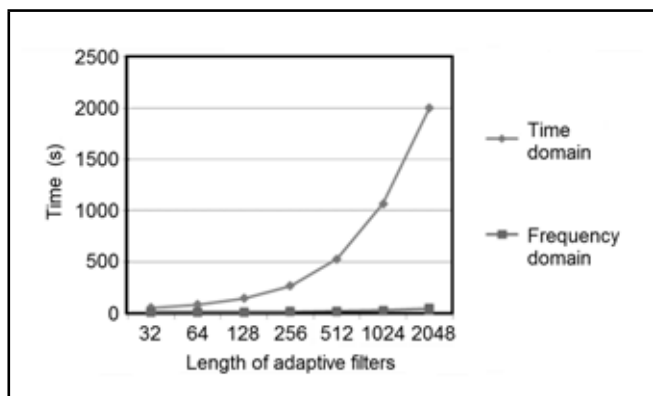
Figure 8. Computational time of the MFxLMS algorithm in the time domain and in the frequency domain for different filter lengths.

main[10] can be compared to our two-stage MFxLMS algorithm. The time consumed by the two algorithms over a 10-iteration average are listed in Table 1 and shown in Fig. 8, and the computational efficiency of the two-stage MFxLMS algorithm is clearly visible, especially for the long filter length.

The effect of blind pre-processing on the following MFxLMS algorithm will be more significant if the reference paths have longer response time or if there is a large eigenvalue spread of $\mathbf{R}(\omega)$ introduced by the reference paths. Furthermore, the two-stage adaptive algorithm in the frequency domain will have better tracking ability than the traditional MFxLMS algorithm in time-varying environments or for non-stationary noise sources.

6. CONCLUSIONS

A new blind pre-processing system is added before the traditional multichannel feedforward ANC controller to eliminate

Table 1. A comparison of the MFxLMS algorithm in the time domain and in the frequency domain.

Filter length	32	64	128	256	512	1024	2048
Time domain (s)	55	85	146	268	530	1068	2001
Frequency domain (s)	14	14	14	17	22	31	48

the effect of the reference paths on the traditional MFxLMS algorithm. The new pre-processing system is combining with the traditional MFxLMS system and results in the new two-stage adaptive system. The blind pre-processing system can whiten the reference signals based on the independence assumption for the noise sources; therefore, the convergence of the two-stage adaptive algorithm is faster than that of the traditional MFxLMS algorithm at the cost of twice the computational loading.

The two-stage adaptive algorithm operating in the frequency domain is proposed to improve the computational efficiency of the entire multichannel ANC system with the help of FFT. Especially for the reference paths with large filter length, the proposed two-stage algorithm saves the more computational time apparently in comparison with the conventional algorithm in time domain, as shown in Fig. 8.

REFERENCES

[1] Elliott, S. J. *Signal Processing for Active Control*, Academic Press, London, (2001).

[2] Haykin, S. *Adaptive Filter Theory* (4th ed.), Prentice-Hall, Upper Saddle River, NJ, (2004).

[3] Elliott, S. J., Stothers, I. M., and Nelson, P. A. A multiple error LMS algorithm and its application to the active control of sound and vibration, *IEEE Transactions on Acoustics, Speech, and Signal Processing*, **35**, 1423–1434 (1987).

[4] Chen, G. and Muto, K. A theoretical study of convergence characteristics of a multiple channel ANC system, *International Journal of Acoustics and Vibration*, **9** (4), 191–197, (2004).

[5] Elliott, S. J., Boucher, C. C., and Nelson, P. A. The behaviour of a multiple channel active control system, *IEEE Transactions on Signal Processing*, **40** (5), 1041–1052, (1992).

[6] Wang, K. and Ren, W. Convergence analysis of the multivariable filtered-x LMS algorithm with application to active noise control, *IEEE Transactions on Signal Processing*, **47** (4), 1166–1169, (1999).

[7] Chen, G., Abe, M., and Sone, T. Effects of multiple secondary paths on convergence properties in active noise control systems with LMS algorithm, *Journal of Sound and Vibration*, **195** (1), 217–228, (1996).

[8] Elliott, S. J. Optimal controllers and adaptive controllers for multichannel feedforward control of stochastic disturbances, *IEEE Transactions on Signal Processing*, **48** (4), 1053–1060, (2000).

[9] Chen, G., Wang, H., Chen, K., and Muto, K. The influence of path characteristics on multichannel feedforward active noise control system, *Journal of Sound and Vibration*, **311**, 729–736, (2008).

[10] Wang, H., Chen, G., Chen, K., and Muto, K. Blind pre-processing method for multichannel feedforward active noise control, *Acoustical Science and Technology*, **27** (5), 278–284, (2006).

[11] Joho, M., and Schniter, P. Frequency domain realization of a multichannel blind deconvolution algorithm based on the natural gradient, *ICA 2003*, April 4–6, Nara, Japan, 543–548, (2003).

[12] Douglas, S. C., Sawada, H., and Makino, S. Natural gradient multichannel blind deconvolution and speech separation using causal FIR filters, *IEEE Transactions on Speech and Audio Processing*, **13** (1), 92–103, (2005).

[13] Cichocki, A. and Amari, S. *Adaptive blind signal and image processing: learning algorithms and applications*, Wiley, NJ, (2002).

[14] Kajikawa, Y. and Nomura, Y. Frequency domain active noise control system using optimal step-size parameters, *IEEE ICASSP '01*, **5**, 3217–3220, (2001).

[15] Das, D., Panda, G., and Kuo, S. New block filtered-X LMS algorithms for active noise control systems, *IET Signal Processing*, **1** (2), 73–81, (2007).

[16] Das, K. and Satapathy, J. Frequency-domain block filtered-x NLMS algorithm for multichannel ANC, *First International Conference on Emerging Trends in Engineering and Technology ICETET '08*, 1293–1297, (2008).

On Parametric Response Characteristics of Beams With Multiple Transverse Cracks

U.K. Mishra and S.K. Sahu

Department of Civil Engineering, NIT, Rourkela—769008, India

This study deals with the parametric instability of a beam with multiple cracks. The variation of buckling load and dynamic stability regions, with respect to relative crack depth and position of cracks, are analysed using FEM. The loading on the beam is considered to be axial with a simple harmonic fluctuation with respect to time. The equation of motion represents a system of second order differential equations with periodic coefficients of the Mathieu-Hill type. The development of the regions of instability arises from Floquet's theory, and the periodic solution is obtained by Bolotin's approach using the finite element method. The stiffness matrix of the cracked beam element is obtained from the flexibility matrix of the intact beam, and the additional flexibility matrix due to the crack. The frequencies of vibration and buckling loads of the cracked cantilever beams reduce with the increase in crack depth and number of cracks. The onset of instability occurs earlier with the introduction of more cracks. The instability region for the crack location nearer to the fixed end occurs at a lower excitation frequency of the cracked beam. The vibration and instability results can be used as a technique for structural health monitoring or testing of structural integrity, performance, and safety.

1. INTRODUCTION

Many engineering structures may have structural defects, such as cracks, due to mechanical vibrations, environmental elements, corrosion, long term service, cyclic load, or etc. The presence of transverse cracks in beams may carry the potential risk of destruction and increases maintenance costs. This flexibility changes the dynamic behaviour of the structural member. Besides this, modern crack detection procedures, such as ultrasonic or X-rays, prove to be inoperative and unsuitable in many industrial situations due to detailed periodic inspections. Therefore, crack detection through vibration analysis is of tremendous technical importance. One of the most investigated approaches in detecting damage is the use of vibration data as a basis for structural health monitoring. Many considerations can contribute to the formation of a crack, and the potentially catastrophic consequences have made structural integrity testing an extremely active area of research. Hence, the dynamic characteristics of cracked beams are of considerable importance in many designs.

The effects of cracks upon the dynamic characteristics of beams are studied by many authors. Some details of earlier works on the topic has been reported in the review paper by Dimarogonas.[1] Kisa et al. analysed the free vibration characteristics of cracked beams by the finite elements and component mode synthesis method.[2] Yokoyama and Chen studied the vibration characteristics of a uniform Bernoulli-Euler beam with a single edge crack using a modified line-spring model.[3] Saavedra and Cuitino presented the theoretical and experimental dynamic behaviour of a free-free beam with a transverse crack using the finite element method.[4] Viola et al. proposed a procedure for identifying cracks in structures using model test data and the finite element method.[5] Sinha and Friswell examined the vibration behaviour of a free-free beam with a breath-

ing crack, simulated for a sinusoidal input force using the finite element method.[6] Krawczuk et al. studied the dynamic behaviour of a cracked Timoshenko beam using the spectral element method.[7] Zheng and Kessissoglu obtained the natural frequencies and mode shapes of a cracked beam using the finite element method.[8] Loya et al. obtained the natural frequencies of vibrations of simply supported Timoshenko beams with cracks using a perturbation method.[9]

However, most of these studies involved the dynamic characteristics of beams with a single crack. Shifrin et al. proposed a new method for calculating the natural frequencies of a vibrating beam with an arbitrary finite number of transverse open cracks.[10] Khiem et al. studied the free vibration characteristics of a beam with an arbitrary number of cracks,[11] while Behera et al. used an analytical method for solving the frequency equation of an elastic beam with single and multiple cracks.[12] Kisa and Gurel proposed a numerical model that combines the finite element and the component mode synthesis method for modal analysis of circular beams with non-propagating open crack.[13] Kisa and Gurel further extended their study to the free vibration analysis of uniform and stepped circular beams with cracks using the same approach.[14] Orhan studied free vibration analysis of a cracked beam in order to identify the crack in a cantilever beam by using the analytical method and finite element modelling in ANSYS.[15] Viola et al. conducted a free vibration analysis of an axially loaded, cracked Timoshenko beam using the dynamic stiffness method.[16]

But the stability studies involving beams with cracks are scarce. Zheng and Fan investigated the vibration and stability of cracked hollow beams by applying Hamilton's principle and a modified Fourier series representing the vibration and buckling modes.[17] Kishen and Kumar examined the behaviour of cracked beam-columns of different slenderness ratios subjected to axial and lateral loads using the finite ele-
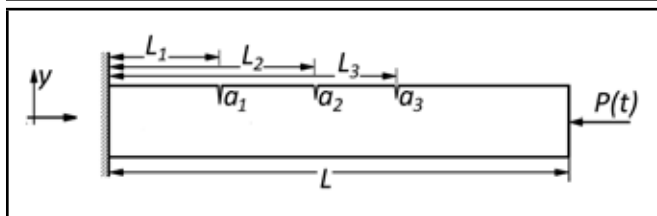
Figure 1. A cantilever beam with multiple cracks subjected to an in-plane periodic load.

ment method.[18] Jiki investigated on the buckling analysis of a pre-cracked beam with Liapunov's second method.[19] Skrinar discussed the implementation of a simplified computational model for transversely cracked beams for buckling analysis.[20]

Structural elements subjected to in-plane periodic forces may undergo unstable transverse vibrations, leading to parametric resonance. As per Bolotin,[21] the first analysis of parametric resonance of a column without a crack was studied by Beliav. Bolotin presented the general theory of dynamic stability and studied the parametric resonance problems of various kinds of structural components without cracks. Thomas and Abbas[22] developed a finite element model for the stability analysis of Timoshenko beams.[23] Chen and Shen studied the dynamic stability of a cracked rotating beam of general orthotropy using the finite element method.[24] Briseghella et al. used the finite element method to find the regions of dynamic stability of beams and frames without cracks.[25] Recently, Dai and Chen analysed the dynamic stability of a nonlinear cracked rotor system with unsymmetrical viscoelastic supports, adopting the Rayleigh model.[26] The linear and nonlinear dynamic stabilities of the system are investigated on the basis of the HBM method, utilizing Lyapunov theory and the Floquet criterion. However, no work has been reported on the instability behaviour of beams with multiple cracks subjected to in-plane periodic forces. The distinction between good and bad vibration regimes of cracked beams subjected to in-plane periodic loading can be distinguished through calculation of dynamic instability regions. The calculation of these spectra is often studied in the form of natural frequencies and static buckling load. In this study, vibration, buckling, and parametric resonance characteristics of a cracked beam with multiple edge cracks is studied using the finite element method. The variations of the different parameters, with respect to relative crack depth and position crack, are studied.

2. MATHEMATICAL FORMULATION

The basic configuration of the problem investigated is a beam of any boundary condition with a transverse crack subjected to periodic in-plane edge load $P(t)$. However, a typical cantilever beam subjected to in-plane harmonic load is considered here and shown in Fig. 1.

2.1. The Methodology

The loading on the beam is considered as axial, with a simple harmonic fluctuation with respect to time. The analysis is assumed to be linear and all damping effects are neglected. The equation of motion represents a system of second order differential equations with periodic coefficients of the Mathieu-Hill

variety. The development of the regions of instability arise from Floquet's theory and the solution is obtained by Bolotin's approach using the finite element method.[21] The equation of motion for the vibration of cracked beams subjected to in-plane load $P(t)$ reduces to matrix form as

$$[M]\{\ddot{q}\} + \big[[K_e] - P(t)[K_g]\big]\{q\} = 0; \quad (1)$$

where q is the vector of degrees of freedom. $[M]$, $[K_e]$ and $[K_g]$ are the mass, elastic stiffness, and geometric stiffness matrices of the beam. The in-plane load $P(t)$ may be harmonic and can be expressed in terms of static component of load P_s and dynamic component of load P_t, where P_s is the static portion of load $P(t)$, and P_t is the amplitude of the dynamic portion of $P(t)$. Considering the static and dynamic component of load as a function of the critical load P_{cr},

$$P_s = \alpha P_{cr}, \text{ and } P_t = \beta P_{cr}; \quad (2)$$

where α and β are the static and dynamic load factors, respectively. Therefore,

$$P(t) = P_s + P_t \cos \Omega t; \quad (3)$$

where Ω is the frequency of the excitation.

The stress distribution in the beam may be periodic. Substituting Eqs. (2) and (3) in Eq. (1), the equation of motion for a beam with cracks under periodic loads may be reduced to

$$[M]\{\ddot{q}\} + \big[[K_e] - \alpha P_{cr}[K_g] - \beta P_{cr}[K_g] \cos \Omega t\big]\{q\} = 0. \quad (4)$$

Equation (4) represents a system of differential equations with periodic coefficients of the Mathieu-Hill type. The development of regions of instability arises from Floquet's theory, which establishes the existence of periodic solutions of periods T and $2T$. The boundaries of the primary instability regions with the period $2T$, where $T = 2\pi/\Omega$, are of practical importance and the solution can be achieved in the form of the trigonometric series as suggested by Bolotin:[21]

$$q(t) = \sum_{k=1,3,5,\ldots}^{\infty} \left(\{a_k\} \sin \frac{k\Omega t}{2} + \{b_k\} \cos \frac{k\Omega t}{2} \right). \quad (5)$$

Substituting the value of q, Eq. (4) reduces to

$$[M] \sum_{k=1,3,5,\ldots}^{\infty} - \left(\frac{k\Omega}{2} \right)^2 \left(\{a_k\} \sin \frac{k\Omega t}{2} + \{b_k\} \cos \frac{k\Omega t}{2} \right) +$$
$$\big[[K_e] - \alpha P_{cr}[K_g] - \beta P_{cr}[K_g] \cos \Omega t\big] \cdot$$
$$\cdot \left(\{a_k\} \sin \frac{k\Omega t}{2} + \{b_k\} \cos \frac{k\Omega t}{2} \right) = 0. \quad (6)$$

Equating the coefficients of sine and cosine leads to a series of algebraic equations for the vectors a_k and b_k for determining instable regions. For nontrivial solutions, the infinite determinants of the coefficients of the groups of homogenous equations are set equal to zero. Approximate solutions are obtained by truncating the determinants. The principal instability region, which is of practical interest, corresponds to $k = 1$ and for this, the instability condition is in-line with Bolotin as[21]

$$\big[[K_e] - \alpha P_{cr}[K_g] \pm \frac{1}{2}\beta P_{cr}[K_g] - \frac{\Omega^2}{4}[M]\big]\{q\} = 0. \quad (7)$$
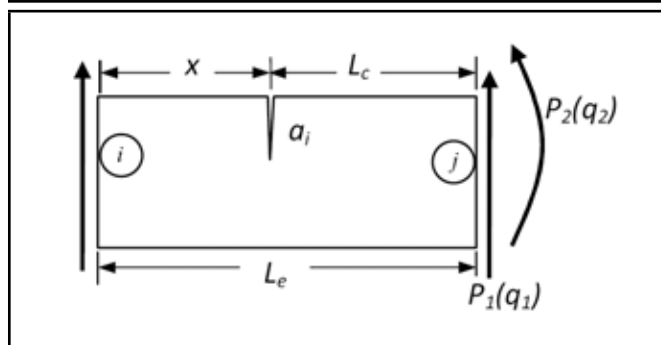
Figure 2. A typical cracked beam element with nodal forces and displacements.

Equation (7) represents an eigenvalue problem for the known values of α, β and P_{cr}. The two conditions under the plus and minus sign correspond to two boundaries of the dynamic instability region. The eigenvalues are Ω, which give the boundary frequencies of the instability regions for the given values of α and β. In this analysis, the computed static buckling load of the beam with cracks is considered as the reference load.

The following equations represent the solution to the related problems. For free vibration with $\alpha = 0$, $\beta = 0$, $\omega = \frac{\Omega}{2}$:

$$\left[[K_e] - \omega^2[M]\right]\{q\} = 0; \qquad (8)$$

and for static stability with $\alpha = 1$, $\beta = 0$, $\Omega = 0$:

$$\left[[K_e] - P_{cr}[K_g]\right]\{q\} = 0. \qquad (9)$$

2.2. The Stiffness Matrix for the Cracked Beam Element

The method used to obtain the stiffness matrix of a cracked beam element is to take the total flexibility matrix and invert it. The total flexibility matrix of the cracked beam element includes two parts. The first part is original flexibility matrix of the intact beam element and the second part is the additional flexibility matrix of the beam element due to the presence of the crack. The element bending stiffness matrix of the intact beam of two noded Timoshenko beams with shear deformation used in this analysis, in line with Kisa et al., is[2]

$$[k_e] = \frac{EI}{L(L^2 + 12\beta)} \begin{bmatrix} 12 & 6L & -12 & 6L \\ 6L & 4L^2 & -6L & 2L^2 \\ -12 & -6L & 12 & -6L \\ 6L & 2L^2 & -6L & 4L^2 \end{bmatrix}; \quad (10)$$

where $\beta = \frac{EI}{\kappa GA}$, EI equals the flexural rigidity of the beam, and G equals the shear modulus of the beam material.

Figure 2 shows a typical cracked beam element with a rectangular cross section of breadth b and depth h, with a crack of depth a. The left hand side end node i is assumed to be fixed, while the right hand side end node j is subjected to the shearing force P_1 and the bending moment P_2. The corresponding generalized displacements are denoted as q_1 and q_2. L_c equals the distance between the right hand side of end node j and the crack location, L_e equals the length of the beam element, and A equals the area of the element.

The total strain energy of the beam is equal to the strain energy of uncracked (intact) beam plus the additional strain energy due to crack:

$$U = U_{vc} + U_c. \qquad (11)$$

According to Zheng and Kessissoglou, the additional strain energy existence of the crack can be expressed as[8]

$$U_c = \int_{A_c} G_s dA_c; \qquad (12)$$

where G_s equals the strain energy release rate and A_c equals the effective cracked area.

$$G_s = \frac{1}{E'}\left[\left(\sum_{n=1}^2 K_{In}\right)^2 + \left(\sum_{n=1}^2 K_{IIn}\right)^2 + k\left(\sum_{n=1}^2 K_{IIIn}\right)^2\right]; \qquad (13)$$

where $E' = E$ for plane stress, $E' = E/1-\nu^2$ for plane strain case, $k = 1 + \nu$, and K_I, K_{II}, and K_{III} are stress intensity factors for opening, sliding, and tearing type cracks.

The strain energy release rate for an open crack neglecting axial deformation is given by

$$G_s = \frac{1}{E'}\left[(K_{I1} + K_{I2})^2 + K_{II1}^2\right]; \qquad (14)$$

The stress intensity factors for the cracked beam in line with Zheng and Kessissoglou are given by[14]

$$K_{I1} = \frac{6P_1 L_c}{bh^2}\sqrt{\pi\xi F_1(s)};$$
$$K_{I2} = \frac{6P_2}{bh^2}\sqrt{\pi\xi F_1(s)}; \quad \text{and}$$
$$K_{II1} = \frac{P_2}{bh}\sqrt{\pi\xi F_2(s)}; \qquad (15)$$

where $s = \frac{\xi}{h}$ and ξ is the crack depth during the process of penetrating from initially zero depth to the final depth (a), where

$$F_1(s) = \sqrt{\frac{\tan\frac{\pi s}{2}}{\frac{\pi s}{2}}}\left[0.923 + 0.199\frac{\left(1 - \sin\frac{\pi s}{2}\right)^4}{\cos\frac{\pi s}{2}}\right]; \quad (16)$$

and

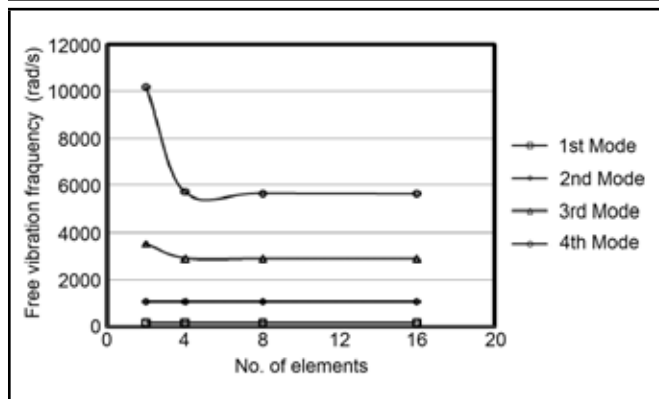$$F_{II}(s) = 1.122 - 0.561s + 0.085s^2 + \frac{0.180s^3}{\sqrt{1-s}}. \qquad (17)$$

From definition, the elements of the overall additional flexibility matrix C_{ij} can be expressed as

$$C_{11} = \frac{2\pi}{E'b}\left[\frac{36L_c^2}{h^2}\int_0^{\frac{a}{h}} xF_1^2(x)dx + \int_0^{\frac{a}{h}} F_{II}^2(x)dx\right]; \quad (18a)$$
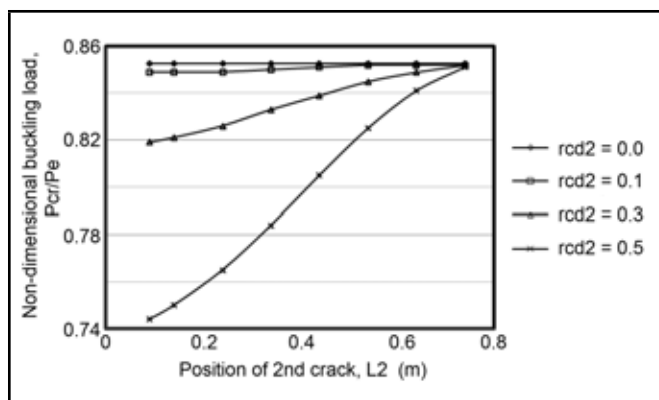
$$C_{12} = \frac{72\pi L_c}{E'bh^2}\left[\int_0^{\frac{a}{h}} xF_1^2(x)dx\right] = C_{21}; \qquad (18b)$$

and

$$C_{22} = \frac{72\pi}{E'bh^2}\left[\int_0^{\frac{a}{h}} xF_1^2(x)dx\right]. \qquad (18c)$$

Figure 3. The variation of the natural frequency of a cracked beam with respect to the number of elements.

Figure 4. The variation of the non-dimensional buckling load of a cantilever beam with two cracks at $L_1 = 0.04$ m (rcd1 $= 0.5$) and $L_2 = 0.09$ to 0.74 m (rcd2 $= 0.0, 0.1, 0.3,$ and 0.5).

Then,

$$C_{\text{total}} = C_{\text{intact}} + C_{\text{ovl}} \quad \text{and} \quad K_{\text{crack}} = LC_{\text{total}}^{-1}L^T; \quad (19)$$

where L equals the transformation matrix given by

$$L = \begin{bmatrix} -1 & 0 \\ L_e & -1 \\ 1 & 0 \\ 0 & 1 \end{bmatrix}. \quad (20)$$

Standard procedure is carried out to obtain the mass and geometric matrix of the intact and cracked beam in line with Cook et al.,[27] as the element mass matrix

$$[m_e] = \frac{\rho AL}{420} \begin{bmatrix} 156 & 22L & 54 & -13L \\ 22L & 4L^2 & 13L & -3L^2 \\ 54 & 13L & 156 & -22L \\ -13L & -3L^2 & -22L & 4L^2 \end{bmatrix}; \quad (21)$$

and the element geometric stiffness matrix

$$[k_{g_e}] = \frac{P}{10} \begin{bmatrix} \frac{12}{L} & 1 & -\frac{12}{L} & 1 \\ 1 & \frac{4L}{3} & -1 & -\frac{L}{3} \\ -\frac{12}{L} & -1 & \frac{12}{L} & -1 \\ 1 & -\frac{L}{3} & -1 & \frac{4L}{3} \end{bmatrix}. \quad (22)$$

2.3. The Computer Program

A computer program is developed to perform all the necessary computations in MATLAB. The mass and geometric

Table 1. Comparison of the first non-dimensional natural frequencies (ω_1/ω_{01}) of a beam with two cracks for different crack locations and relative crack depths.

Location of second crack	rcd = 0.1		rcd = 0.2		rcd = 0.3	
	Present analysis using FEM	Analytical method of Shifrin et al.[10]	Present analysis using FEM	Analytical method of Shifrin et al.[10]	Present analysis using FEM	Analytical method of Shifrin et al.[10]
0.05	0.9924	0.994	0.980	0.984	0.960	0.968
0.1	0.9932	0.995	0.983	0.986	0.966	0.973
0.2	0.9945	0.996	0.988	0.991	0.977	0.981
0.3	0.9955	0.996	0.992	0.994	0.986	0.989
0.4	0.9961	0.997	0.994	0.995	0.991	0.993
0.5	0.9965	0.997	0.996	0.997	0.995	0.996
0.6	0.9967	0.997	0.997	0.997	0.996	0.997
0.7	0.9967	0.997	0.997	0.997	0.997	0.997

stiffness matrix are developed using standard procedure. The stiffness matrix of the cracked beam is obtained by the inverse of the total flexibility matrix, which is obtained by adding the flexibility matrix of the intact beam to the overall flexibility matrix due to the crack.

3. RESULTS AND DISCUSSION

Quantitative results on the effects of various parameters on the vibration, buckling, and dynamic stability of the cracked beams are presented. A shear correction factor of 5/6 is used for all numerical results. The results are presented in the following order:

3.1. The Convergence Study,

3.2. A Comparison with Previous Studies, and

3.3. Numerical Results.

3.1. The Convergence Study

The convergence study is carried out for the free vibration of a cracked beam. Variations of four modes of natural frequency are plotted for a beam with a crack in Fig. 3 for different discretization of elements. Based on this study, the frequencies of the vibration of a beam discretized into 16 elements seem to have yielded converged results. All further results are computed using this discretization.

3.2. A Comparison with Previous Studies

The finite element analysis is carried out for the free vibration of cracked beams for various crack positions and crack depths of the example problem considered by Shifrin et al. in their new model.[10] The ratio between the first natural frequencies of the cracked and uncracked beam is shown in Table 1 with the results of Shifrin et al.[10] The values are interpolated using the graph analysis software Windig 2.5. It is clear that there exists an excellent agreement between the results based on the present FEM with previous studies.

3.3. Numerical Results

The study is extended to find the variations of buckling loads and parametric resonance behaviour due to multiple transverse cracks in a beam. The cantilever beam under analysis has the
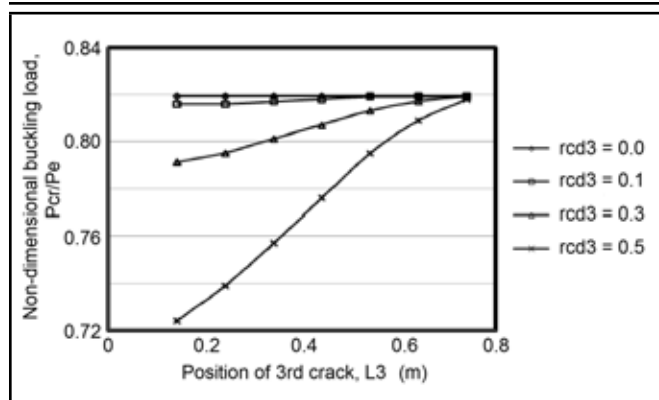
Figure 5. The variation of the non-dimensional buckling load of a cantilever beam with three cracks at $L_1 = 0.04$ m (rcd1 = 0.5), $L2 = 0.09$ m (rcd2 = 0.3), and $L_3 = 0.14$ to 0.74 m (rcd3 = 0.1, 0.3, and 0.5).

following properties: length $L = 0.8$ m, rectangular cross-section with width $b = 0.02$ m, and height $h = 0.02$ m. $E = 210 \times 10^9$ N/m², Poisson's ratio $= 0.28$, and mass density $= 7800$ kg/m³.

3.3.1. Buckling of a Beam with Multiple Cracks

The non-dimensional buckling loads are computed for a cantilever beam with the above geometry and material properties with two or three cracks. For the cantilever beam subjected to two cracks, the first crack is considered at 0.04 m of relative depth 0.5, and the position of the second crack is varied between 0.09 m to 0.74 m from the fixed end for a relative depth of 0.0, 0.1, 0.3, and 0.5. The variation of the non-dimensional buckling load of the above is computed and plotted in Fig. 4. From the above figure it is observed that the non-dimensional buckling load reduces by 14.71%, 15.07%, 18.07%, and 25.57% for the second crack at 0.09 m for the relative depths of 0.0, 0.1, 0.3, and 0.5 respectively. This implies that the non-dimensional buckling load reduces by 14.71% when the relative depth of the second crack at 0.09 m is 0.0, i.e., the second crack is absent. But as the depth of the second crack increases, the buckling load decreases further due to reduction in stiffness of the sections. When the second crack moves away from the fixed end, the buckling load gradually increases, and for the second crack at 0.74 m, the non-dimensional buckling loads P_{cr}/P_e are reduced by 14.71%, 14.77%, 14.77%, and 14.87% for the relative depths of the second crack (rcd2) are equal to 0.0, 0.1, 0.3, and 0.5 respectively, for the intact beam. It is also observed that as the second crack approaches the free end, its effect on the buckling load reduces and for the second crack, close to free end, this effect almost vanishes. The critical load of the beam is such as if it is subjected to only one crack, i.e., the first crack.

Now a third crack of relative depth 0.1, 0.3, and 0.5 is introduced between 0.14 m to 0.74 m from the fixed end of the beam, keeping the first crack at 0.04 m of relative depth 0.5 and the second crack at 0.09 m of relative depth 0.3. Non-dimensional buckling loads are computed for the above beam and plotted in Fig. 5 for different location and depth of the third crack. From the figure, it shows that the introduction of the third crack at 0.14 m from the fixed end decreases the non-dimensional critical buckling load P_{cr}/P_e by 18.07%,

18.37%, 20.87%, and 27.57%, respectively, for third relative crack depths (rcd3) of 0.0, 0.1, 0.3, and 0.5. This implies there is a decrease of 18.07% in the buckling load of the beam when the relative depth of the third crack is 0.0, i.e., when there is no third crack. But as the location of the third crack shifts away from the fixed end, the buckling load increases; for its position at 0.74 m from the fixed end, the buckling loads reduce by 18.07%, 18.07%, 18.07%, and 18.17% of the intact beam for relative crack depths of 0.0, 0.1, 0.3 and 0.5. This shows that the effect of the third crack gradually decreases as it shifts farther away from fixed end and that the crack near the free end nearly vanishes. This may be due to the fact that for cracks near fixed end, the effect of end restraint is more than the cracks away from it. A crack near the fixed end makes the beam more flexible than it is at the free end.

The effects of the cracks on the mode shapes of vibration were discussed by many investigators, including Behera et al.,[12] along with the same research group. The changes in the mode shapes of cracked beams compared to those of an uncracked beam are quite significant, except for the crack position at the nodal points. This is due to the stress singularity phenomenon. The amplitude of vibration is heightened in the case of cracked cantilever beams when the crack is near the fixed end. The amplitude of vibration is nearly the same when the crack is near the free end. The slope of the mode shape of the cracked beam is changing at the point of the crack, unlike the intact beam.

3.3.2. Parametric Instability of a Beam with Multiple Cracks

The study is further extended to find the variation of the excitation frequencies and regions of the instability of the same cantilever beam for intact and cracked conditions with single and multiple cracks. The instability regions of an intact beam and a cracked cantilever beam with a crack at 0.04 m from the fixed end for different depths of cracks and dynamic load factors is plotted in Fig. 6, where the static load factor is 0.2. It is observed that the excitation frequency for instability decreases by 0.52%, 4.40%, and 14.00% for the intact beam for a relative crack depth of 0.1, 0.3, and 0.5, respectively, when the dynamic load factor is 0.0. This excitation frequency decreased by 1.07%, 9.26%, and 32.04%, respectively, for relative depths of 0.1, 0.3, and 0.5 when the dynamic load factor is 1.0. From the above observations, it can be concluded that as the depth of the crack increases, the rate of decrease in the excitation frequency increases. Similarly, with the increase in dynamic load factor, the rate of reduction in excitation frequency for dynamic instability also increases. The dynamic stability regions of the intact beam and the cracked beam with a relative crack depth of 0.1 occurring closely to each other suggests that the crack of relative depth of 0.1 has little effect in reducing the excitation frequency than does other depths.

The variation of the excitation frequency for the dynamic instability for a cracked beam subjected to in-plane periodic loads for different static load factors ($\alpha = 0.0, 0.2,$ and 0.4) are shown in Fig. 7. Refering to the above figure, it is observed that the excitation frequency for the dynamic instability decreases as the static load factor (α) increases. The excitation frequency
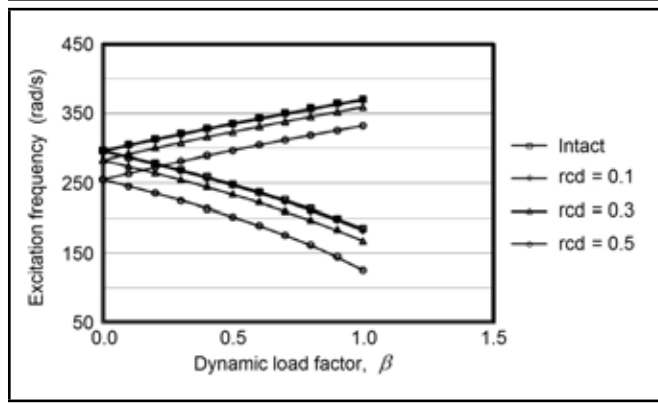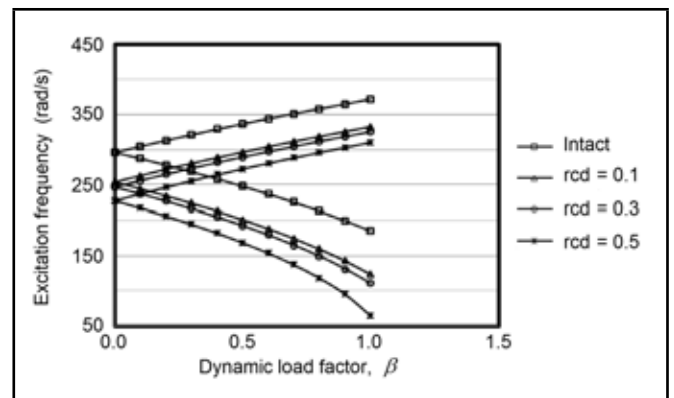
Figure 6. The variation of the dynamic instability regions with respect to the relative crack depth for a crack located 0.04 m from the fixed end when the static load factor 0.2.
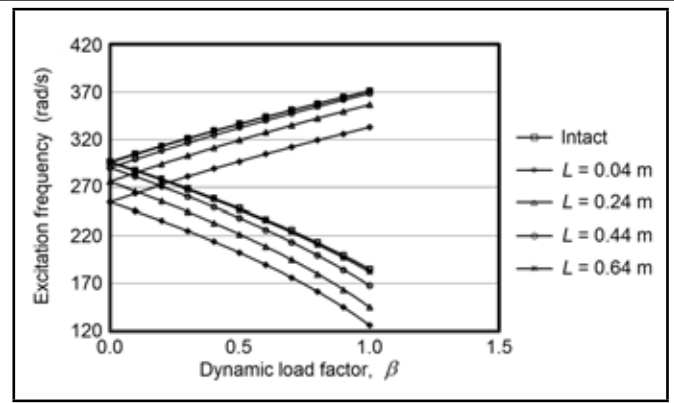
Figure 8. The variation of the dynamic instability region of a cracked beam for a different location of a crack of relative depth 0.5 and static load factor 0.2.
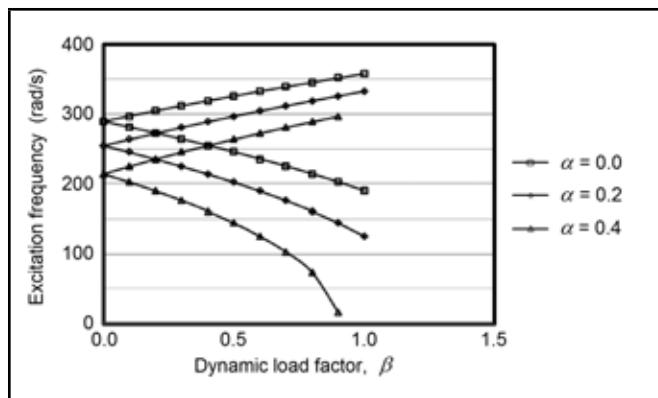
Figure 7. The variation of the dynamic instability regions of a cantilever beam with respect to the static load factor ($\alpha = 0, 0.2$, and 0.4) for a crack at $L = 0.04$ m with relative depth 0.5.

Figure 9. The variation of the dynamic instability regions of an intact beam and a beam with two cracks for different relative depths (rcd = $0.1, 0.3$, and 0.5) of a second crack located 0.09 m from the fixed end.

for dynamic instability, with respect to dynamic load factor for different crack location for a crack of relative depth 0.5, is plotted in Fig. 8 for static load factor 0.2. It is observed that excitation frequency of the cracked beam due to instability is decreased by 14%, 7.03%, 2.07%, and 0.18% than that of intact beam when the crack is at position $L = 0.04$ m, 0.24 m, 0.44 m, and 0.64 m from the fixed end for dynamic load factor 0.0. But when the dynamic load factor is 1.0 with a static load factor 0.2, the same is reduced by 32.04%, 21.78%, 9.54%, and 1.62% for the above positions of the crack. From the above observations and Fig. 8, it is clear that the excitation frequency for dynamic instability increases as the crack moves away from the fixed end towards the free end. The effect of the crack is felt more with the increase in load factors. When the crack is near the free end, the instability region almost approaches the intact beam, suggesting that the crack near the free end is least more vulnerable in terms of instability than a crack at any other location.

The introduction of a second crack at 0.09 m, with the first crack at 0.04 m of relative crack depth 0.5 m, is analysed for different crack depths. In Fig. 9, dynamic instability regions with a static load factor of 0.2 are plotted for an intact beam and a beam with two cracks at $L_1 = 0.04$ m of relative crack depth $= 0.5$, and $L_2 = 0.09$ m for different relative crack depths. It is observed that for a beam with two cracks close to the fixed end, the excitation frequencies of dynamic instabil-

ity decrease more rapidly as the depth of the crack increases. This decrease is 14.32%, 16.78%, and 23.16% for beams with the relative crack depth of the second cracks as 0.1, 0.3, and 0.5, respectively, with first crack of relative depth of 0.5. The decrease in the excitation frequency was 14.00% for a beam with the first crack only at 0.04 m of relative depth of 0.5. This implies the effect of the second crack reducing the excitation frequency is minimal for small depths, and as the depth of the second crack increases, this effect is more pronounced.

The same cantilever beam is then analysed with the introduction of a third crack of different depths than the first two cracks, measuring 0.04 m and 0.09 m of relative depth as 0.5 and 0.4, respectively. The variation of the dynamic instability frequencies for the various relative depths of the third crack at 0.14 m from the fixed end is plotted in Fig. 10 for the different dynamic load factors and the static load factor 0.2. The decrease in excitation frequency for the dynamic instability is found to be 19.30%, 21.05%, and 25.77% for the relative depth of the third as 0.1, 0.3, and 0.5, respectively, when the static load factor is 0.2 and the dynamic load factor is zero. The same decreased by 49.20%, 56.75%, and 94.88% for the same static load factor and dynamic load factor of 1.0.

Similar to the beam of two cracks, the excitation frequencies for dynamic instability decrease rapidly as the depth of the cracks increase, and this decrease is more rapid with an increase in dynamic load factors. As the depth of the crack
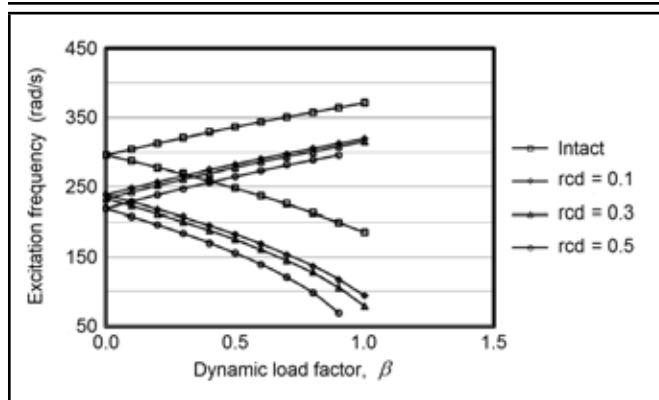
Figure 10. The variation of the dynamic instability regions of an intact beam and a beam with three cracks for different relative depths of the third crack located 0.14 m from the fixed end.
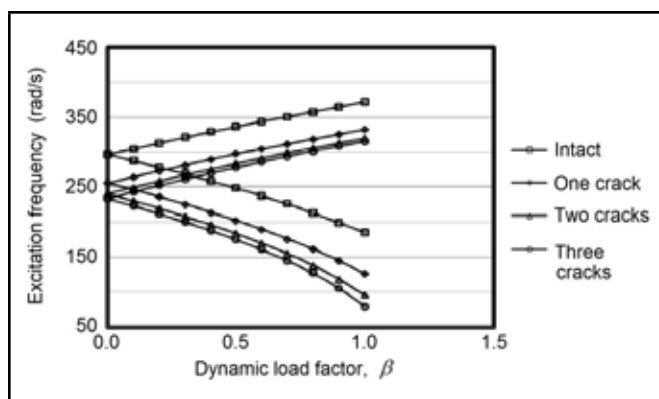
Figure 11. The variation of the dynamic instability regions for a different number of cracks.

at any location is a function of the bending moment (except for material effectiveness), the depth of the crack generally decreases as the location of the crack moves away from the fixed end. The effect of the number of cracks is studied considering the above facts; i.e., the crack farther from the fixed end has a lesser effect than the crack nearer. The regions of dynamic instability for the intact beam and the cracked beam due to in-plane loads with different numbers of cracks are studied. The effect of the crack on the beam is studied for a static load factor of 0.2 and dynamic load factors varying from 0.0 to 1.0. The beam with one crack is considered to be a crack at 0.04 m from the fixed end of 0.5 relative depth. The beam with two open cracks is considered to be at 0.04 m and 0.09 m from the fixed end of relative depths at 0.5 and 0.4, respectively. The beam with three cracks is considered to be at 0.04 m, 0.09 m, and 0.14 m from the fixed end with relative depths of 0.5, 0.4, and 0.3, respectively.

The regions of dynamic instability of the above beams with the intact beam are plotted in Fig. 11. It is observed that there is a drop in the excitation frequency of the beam by 14% for one crack, 19.24% for two cracks, and 21.36% for three cracks from that of intact beam for a static load factor of 0.2 and a dynamic load factor of 0.0. From the excitation frequency of the dynamic instability of the intact beam, the same dropped by 32.04%, 48.53%, and 57.30%, respectively, for the beam subjected to one, two, and three cracks, when the static load factor is 0.2 and the dynamic load factor is 1.0. Refering to Fig. 11, it

can also be concluded that the rate of drop in the excitation frequency decreases as the number of cracks increases, because the increase in the number of cracks is associated with a decrease in their relative depths and their positions move away from the fixed end, as well. Hence, it can be concluded that the crack close to the fixed end and its depth has a bigger impact on dynamic instability. A higher quantity of cracks reduces the dynamic instability frequencies of a beam more, but their intensity decreases with their positions nearing the free end of the beam.

4. CONCLUSION

The frequencies of vibration and the buckling loads of cracked beams decrease with an increase in crack depth for a crack at any location, due to the reduction in stiffness of the section containing the crack. The effect of the crack is more pronounced near the fixed end than at the far free end. The first natural frequency of free vibration, as well as the buckling load, decreases along with an increase in the number of cracks. The instability region for a cracked beam occurs at lower frequency compared to an intact beam. For any crack location, the instability region for the maximum relative crack depth occurs at lower excitation frequency compared to other relative crack depths. For any depth of the crack, the instability region for the crack nearer to fixed end occurs at lower frequency than the crack away from it. The instability region of a beam with crack near the free end almost coincides with the instability region for the intact beam. The static load component has a destabilizing effect in terms of the shifting of the instability regions towards lower frequencies of excitation, and increases the area of instability. The instability region for a beam with more than one crack occurs at a lower excitation frequency compared to a beam with single crack located at the other position. The increase in the number of cracks has a destabilizing effect in terms of the shifting of instability regions towards lower frequencies of excitation.

REFERENCES

[1] Dimarogonas, A. D. Vibration of cracked structures: a state of the art review, *Engineering Fracture Mechanics*, **55**, 831–857, (1996).

[2] Kisa, M., Brandon, J., and Topcu, M. Free vibration analysis of cracked beams by a combination of finite elements and component mode synthesis methods, *Computers and Structures*, **67**, 215–223, (1998).

[3] Yokoyama, T. and Chen, M. C. Vibration analysis of edge-cracked beams using a line-spring model, *Engineering Fracture Mechanics*, **59**, 403–409, (1998).

[4] Saavedra, P. N. and Cuitino, L. A. Crack detection and vibration behaviour of cracked beams, *Computers and Structures*, **79**, 1451–1459, (2001).

[5] Viola, E., Federici, L., and Nobile, L. Detection of crack location using cracked beam element method for structural analysis, *Theoretical and Applied Fracture Mechanics*, **36**, 23–35, (2001).

6   Sinha, J. K. and Friswell, M. I. Simulation of the dynamic response of a cracked beam, *Computers and Structures*, **80**, 1473–1476, (2002).

7   Krawczuk, M., Palacz, M., and Ostachowicz, W. The dynamic analysis of a cracked Timoshenko beam by the Spectral element method, *Journal of Sound and Vibration*, **264**, 1139–1153, (2003).

8   Zheng, D. Y and Kessissoglu, N. J. Free vibration analysis of a cracked beam by finite element method, *Journal of Sound and Vibration*, **273**, 457–475, (2004).

9   Loya, J. A., Rubio, L., and Fernández-Sáez, J. Natural frequencies for bending vibrations of Timoshenko cracked beams, *Journal of Sound and Vibration*, **290**, 640–653, (2006).

10 Shifrin, E. I. and Ruotolo, R. Natural frequencies of a beam with an arbitrary number of cracks, *Journal of Sound and Vibration*, **222** (3), 409–423, (1999).

11 Khiem, N. T. and Lien, T. V. A simplified method for natural frequency analysis of a multiple cracked beam, *Journal of Sound and Vibration*, **245** (4), 737–751, (2001).

12 Behera, R. K., Parhi, D. R. K., and Sahu, S. K. Dynamic characteristics of a cantilever beam with transverse cracks, *International Journal of Acoustics and Vibration*, **11**, 3–18, (2006).

13 Kisa, M. and Gurel, M. A. Modal analysis of multi-cracked beams with circular cross section, *Engineering Fracture Mechanics*, **73**, 963–977, (2006).

14 Kisa, M. and Gurel, M. A. Free vibration analysis of uniform and stepped cracked beams with circular cross sections, *International Journal of Engineering Science*, **45**, 364–380, (2007).

15 Orhan, S. Analysis of free and forced vibration of a cracked cantilever beam, *NDT&E International*, **40**, 443–450, (2007).

16 Viola, E., Ricci, P., and Aliabadi, M. H. Free vibration analysis of axially loaded cracked Timoshenko beam structures using the dynamic stiffness method, *Journal of Sound and Vibration*, **304**, 124–153, (2007).

17 Zheng, D. Y. and Fan, S. C. Vibration and stability of cracked hollow-sectional beams, *Journal of Sound and Vibration*, **267**, 933–954, (2003).

18 Kishen, J. M. C. and Kumar, A. Finite element analysis for fracture behaviour of cracked beam-columns, *Finite Elements in Analysis and Design*, **40**, 1773–1789, (2004).

19 Jiki, P. N. Buckling analysis of pre-cracked beams by Liapunov's second method, *Journal of Mechanics A/Solids*, **26**, 503–518, (2007).

20 Skrinar, M. On critical buckling load estimation for slender transversely cracked beam-columns by the application of a simple computational model, *Computational Material Science*, **43**, 190–198, (2007).

21 Bolotin, V. V. *The Dynamic Stability of Elastic Systems*, San Francisco, CA, Holden Day, (1964).

22 Thomas, J. and Abbas, B. A. H. Dynamic stability of Timoshenko beams by finite element method, *J. Engineering for Industry*, **98**, 1145–1151, (1976).

23 Timoshenko, S. P. and Gere, J. M. *Theory of Elastic Stability*, McGraw-Hill Publishing Company, New York, (1961).

24 Chen, L. W. and Shen, G. S. Dynamic stability of cracked rotating beams of general orthotropy, *Composite Structures*, **37**, 165–172, (1997).

25 Briseghella, L., Majorana, C. E., and Pellegrino, C. Dynamic stability of structures: a finite element approach, *Computers and Structures*, **69**, 11–25, (1998).

26 Dai, L. and Chen, C. Dynamic stability analysis of a cracked Nonlinear rotor system subjected to periodic excitations in machining, *Journal of Vibration and Control*, **13**, 537–556, (2007).

27 Cook, R. D., Malkus, D. S., and Plesha, M. E. *Concepts and Applications of Finite Element Analysis*, 3rd edition, John Wiley & Sons, (2001).

Prediction of Ground Vibrations Induced by Urban Railway Traffic: An Analysis of the Coupling Assumptions Between Vehicle, Track, Soil, and Buildings

Georges Kouroussis

Université de Mons – UMONS, Faculty of Engineering, Department of Theoretical Mechanics, Dynamics and Vibrations, Place du Parc, 20 — 7000 Mons, Belgium

Laurent Van Parys

Université de Mons – UMONS, Faculty of Engineering, Department of Civil Engineering, Place du Parc, 20 — 7000 Mons, Belgium

Calogero Conti and Olivier Verlinden

Université de Mons – UMONS, Faculty of Engineering, Department of Theoretical Mechanics, Dynamics and Vibrations, Place du Parc, 20 — 7000 Mons, Belgium

This paper is concerned with the problem of ground vibrations induced by railway traffic and its modelling through a decoupled approach, using only the finite element modelling for evaluating the ground waves propagation. The vehicle/track dynamics is calculated separately. An important modelling aspect is undoubtedly the track/soil interaction, which can play an important role in the generation of seismic waves. To avoid excessive computational resources, a coupled lumped mass model (CLM model) of the soil has been recently developed and is considered in this study. The influence of ballast and soil stiffnesses is presented, in order to confirm the range of validity of the CLM model. Combined with a discrete two layer model of the track, it offers the possibility of working with a simple compound track/soil model. A comprehensive analysis is provided to show the benefit of the finite element model with the proper radiation conditions at infinity, for analysing the structural response of a building located in the vicinity of the track. Focusing on typical results based on the tram of Brussels, the effects of track/soil and soil/structure coupling are investigated. Modal analyses of the vehicle and the building are presented in order to understand the effects of seismic wave amplification, especially when the source contains frequencies close to the natural frequencies of the building.

1. INTRODUCTION

Problems related to vibrations in buildings represent an important environmental issue in network designs, especially for nearby structures in densely populated cities. Ground vibrations induced by road and railway traffic can cause nuisance to occupants, malfunctioning of sensitive equipment (surgery or high-tech production), and even damage to buildings, if the vibration level exceeds critical values (e.g., 5 mm/s, according to DIN 4150 standards[1]). The growing traffic volume, the higher population density, and the diminishing distance between the vehicle and the structure amplify the overall vibration nuisance. Although most of general traffic exposure vibrations (smooth surface) are not uncomfortable for people, the passing of heavy vehicles on a road or track with an uneven surface is often pointed out as the main vibratory nuisance felt by city residents.

Brussels, the capital of Belgium and of the European Union, is comprised of a heavily urban territory with over one million residents. The railway network in the Brussels Capital Region (160 km^2) consists not only of the urban tramway network but also of the intercity and international train lines, since it represents a vital link in the high speed train (HST) network in the northwest of Europe. Although railway transport appears as the most promising solution to traffic congestion, the development of new lines is confronted with the availability of convenient areas and the mistrust of the dwellers likely to be submitted to new nuisances. These difficulties have been largely encountered during the implementation of the new suburban light rail network. Presently, the tramway represents 25% of urban transport in Brussels.

The accurate prediction of railway–induced ground vibrations, and of the associated structural response, needs an understanding of the complex mechanisms of the generation and propagation of seismic vibration waves. The usefulness of a numerical prediction model has been well emphasized by various authors during the last decades. Empirical models, derived from in situ measurements, and commonly used at the very beginning, have been replaced by numerical models, which are more general and not limited to situations covered by the in situ measurements. Crispino and D'Apuzzo[2] recently described the measurement of road traffic-induced vibrations on a heritage building in Naples, which conducted an empirical
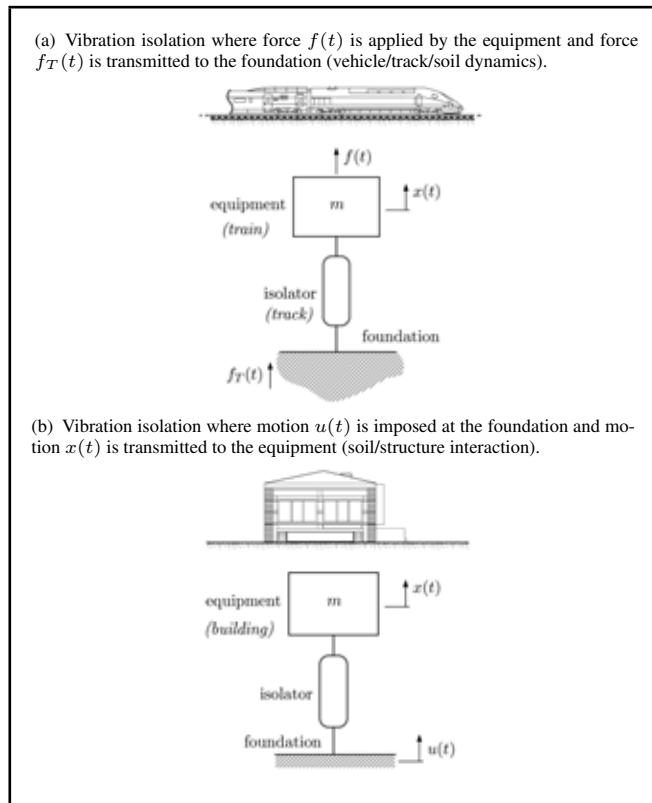
prediction expression of peak particular velocity. This study takes into account the maximum height or depth of the localized surface irregularity over which the heavy vehicle passes, the speed of the vehicle, and the distance between the irregularity and the building. Vogiatzis[3,4] has studied the effect of ground-borne vibrations generated by the metro of Athens on ancient monuments. The results were obtained from the bidimensional finite element model using experimental data, in order to propose efficient mitigation solutions. Track/soil and soil/structure interactions can also be studied from the experimental data, using measured frequency transfer functions coupled with a numerical vehicle/track model.[5,6]

To date, most of the existing numerical methods are based on wavenumber transforms, working in the k–ω domain and allowing an efficient representation of the infinity.[7–9] Nevertheless, the main drawback of these methods is the difficulty to include complex geometries in the model, like embedded structures. In addition, the problem statement is analogous in earthquake engineering, but the frequency content is larger than the one of typical earthquakes (generally under $10\,\text{Hz}$, while traffic-induced vibrations are felt up to $100\,\text{Hz}$). Pyl et al.[10,11] have proposed a numerical method based on the boundary element method coupled with the substructuring finite element model for soil/structure calculation, with an alternative formulation to mitigate fictitious eigenfrequencies borrowed from an original method for acoustic problems. The use of a full finite element (FE) model is more scarce, due to the difficulty of defining the correct absorbing boundary conditions to avoid spurious reflections at the model boundary. For example, Ju[12] has investigated the capacity of the FE approach to simulate the behaviour of vehicle–induced vibrations, proposing a solution for modelling moving elements like wheels on the ground. Large FE models, including the building, are proposed, implying however excessive computational resources and CPU-time.

According to the authors' opinion, the railway-induced ground vibration is analogous to the vibration isolation concepts. When a mechanical system is subjected to a force $f(t)$, a part of this is transmitted to the foundation, depending on the characteristics of the isolation (Fig. (0a)). On the other hand, when the foundation undergoes motion $u(t)$, the equipment also moves, with motion $x(t)$ depending on the equipment-isolator system (Fig. (0b)). In the railway, the first case is associated with the vehicle/track/soil interaction, as the force is defined by the wheel/rail interaction, with the static and dynamic contributions. The track plays the role of isolator by dispatching the forces through the discrete supports (sleepers).

The second case is the soil/structure interaction, with eventual mitigation solutions defining the isolation between the soil and the building. These two concepts are coupled, since the foundation is flexible. Although the connection of the vehicle with a flexible track does not appear with an insurmountable difficulty (see, for example, the works of Dietz et al.,[14] which use the co-simulation method of coupling the multibody and finite element approaches), the coupling with the subgrade imposes some restrictive constraints, due to the methodology employed for modelling the ground:

- In vehicle dynamics, the dynamic simulations are essentially performed in the time domain (essentially with the multibody approach), allowing the assumption of non-


(a) Vibration isolation where force $f(t)$ is applied by the equipment and force $f_T(t)$ is transmitted to the foundation (vehicle/track/soil dynamics).

(b) Vibration isolation where motion $u(t)$ is imposed at the foundation and motion $x(t)$ is transmitted to the equipment (soil/structure interaction).

Figure 1. Schematic diagrams of the vibration isolation systems: an analogy with the railway-induced ground vibration, adapted from[13].

linear behaviour of elements. A possible modal analysis needs, however, the knowledge of eigenvalues and eigenvectors related to the equations of motion, and is associated with a frequency analysis (linearisation around the nominal positions). Nevertheless, the existing methods for ground modelling often impose the simulation domain the frequency analysis for the classical boundary element method, and the time analysis for the finite element method proposed in Kouroussis et al.[15]

- The current computation time required by the multibody software is relatively low. It is known nowadays that the simulation time in soil dynamics is significant, especially for three-dimensional problems with a moving source (inducing a particular modelling of the contact behaviour).

- A periodic representation along the track is often adopted in the track/soil model, allowing for a reduction in computational efforts with the help of an efficient 2.5D approach,[16] but useless if local configurations must be considered in the vehicle/track model (e.g., wheel/rail contact in a rail joint).

This paper investigates the abilities of FE analysis to characterize building vibrations induced by adjacent tramway network with an important rail unevenness (local defect). The retained example concerns the tramway network in Brussels. A prediction method is used in this case, thoroughly validated in the past.[17,18] The purpose of this finite/infinite element model,[17] and the dynamic soil/structure interaction, at the source and the receiver is here accounted for. In addition, the building is analysed with the FE approach, in order to determine its natural frequencies. The same operation is performed
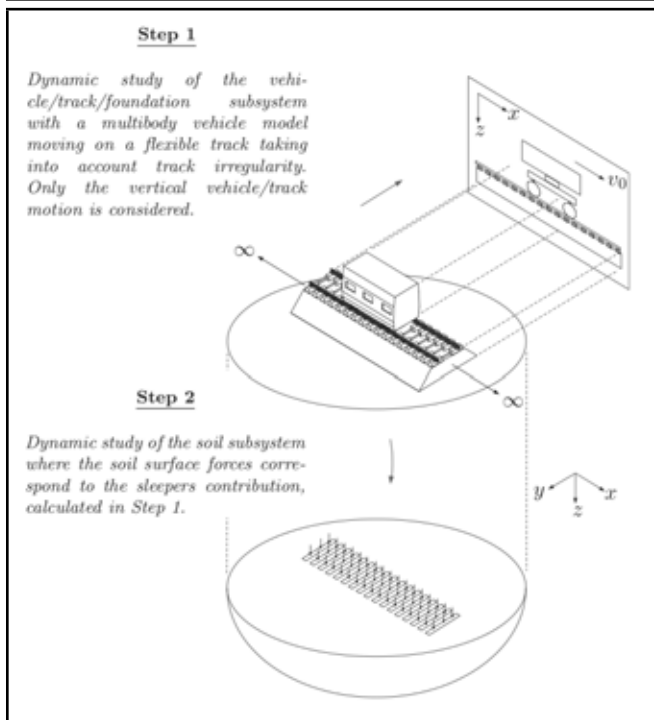
Figure 2. The description of the proposed prediction model, according to a decoupling between the ballast and the soil.

for the vehicle, using the multibody approach, in order to verify if the natural frequencies of the tram coincide with those of the building.

2. PREDICTION MODEL BASED ON A TWO-STEP APPROACH

Recently, Kouroussis et al.[19] proposed a numerical model for predicting the vibration induced in a neighbourhood by a railway vehicle. The particularity of the methodology is based on a two-stages approach, simulating separately the vehicle/track/foundation subsystem and the soil subsystem (Fig. (2)). The first step provides the dynamic behaviour of the vehicle/track/foundation subsystem. The second stage concerns the soil whose free-field response is computed from the loads acting on the soil surface, issued from the first subproblem. The FE method is used in this case, using both infinite elements and viscous boundaries as non-reflecting boundaries, in order to mimic the infinite dimensions of the soil.[20] Both simulations are performed in the time domain. Since each method has specific advantages and shortcomings, it is consequently more interesting to work in two successive simulations to take advantage of their peculiarities; thus, a decoupled approach is proposed. Let us note that the foundation dynamic properties are included in the vehicle/track/foundation with the help of the recently developed coupled lumped mass model (CLM model).[21]

The CLM model is an extension of the well-known Winkler model, which better represents the track soil coupling. An illustrative study is also presented, based on the analysis of track receptances. Finally, the case study findings regarding the ground vibrations are described, with an example coming from the Brussels railway network.
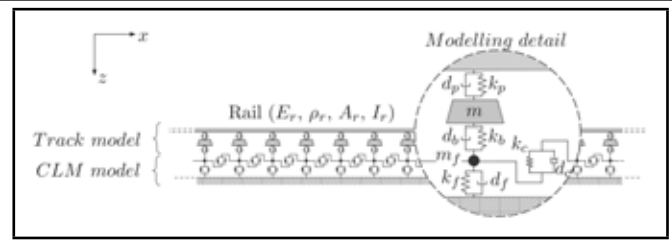
Figure 3. The flexible track, taking into account the condensed soil.

2.1. The Coupled Lumped Mass CLM Model

The mechanical vehicle/track/foundation model (Fig. (3)) that has been recently proposed by Kouroussis et al.[21] is succinctly discussed in this paper. The flexible rail is described by its Young's modulus E_r, its geometrical moment of inertia I_r, its section A_r, and its density ρ_r. Viscoelastic properties are considered for the railpads and ballast, characterised by springs and dampers (k_p and d_p for the railpad, k_b and d_b for the ballast). The CLM model for the foundation is based on the extension of Lysmer's analogue foundation. Besides the foundation mass m_f, stiffness k_f, and damping d_f, additional spring/dashpot systems by means of stiffness k_c and damping d_c are added between adjacent foundation masses for the coupling between each sleeper/foundation contact area. Reduced expressions of transmissiblity have been developed for determining the value of these five parameters. It appears also that damping d_c can be negative for adjusting the ground wave propagation delay.[21]

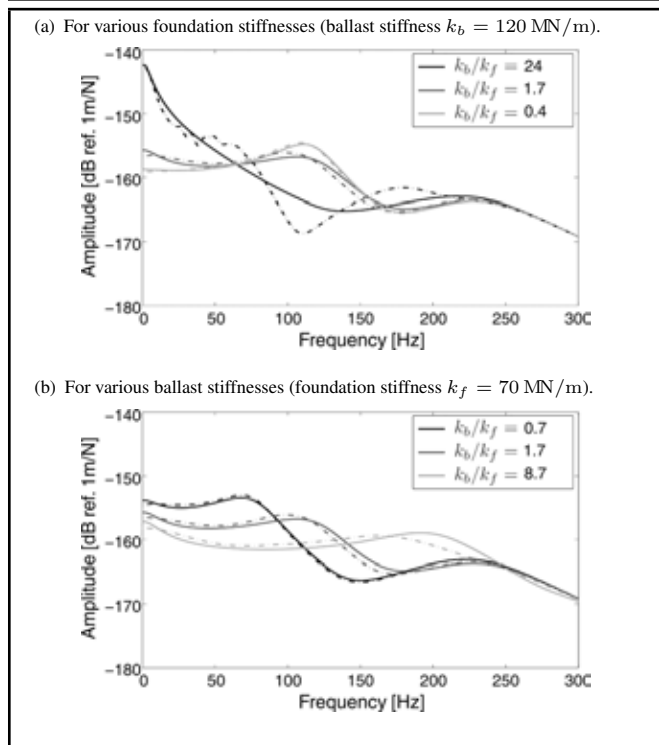## 2.2. Accuracy of the Model on the Track/Soil Coupling: Analysis of the Track Receptance

In order to evaluate the accuracy of the CLM model, track receptances are calculated for a typical track configuration. They correspond to the frequency response functions between the vertical displacement of the rail and the vertical force applied at the same point.

Figures (3a) and (3b) compare the receptances obtained by the CLM model and a rigorous FE model for various k_b/k_f ratios, considering the variation of k_f and k_b, respectively. Figure (4) points out the influence of the stiffness difference, as frequencies of first and second modes, corresponding to in-phase and out-of-phase vertical motions of rail and ballast, depend on the value of k_b, and, to a lesser degree, on the value of k_f (for soft soil). A good correspondence between the two approaches is also observed. Particularly, in the case of soft soil where the track receptance strongly depends on the foundation characteristics, the curve obtained with the CLM model follows the exact solution up to 50 Hz.

3. CASE STUDY: THE TRAM T2000

3.1. Context of the Study

This analysis concerns the vibrations induced by the passing of the Tram T2000, which serves urban districts in Brussels. This vehicle is composed of three coaches: a large one on each end (with a leading bogie), and a small one in the middle (Fig. (5)), with the particularity of large unsprung masses, which is due to the motor placed inside the rotating wheels.

(a) For various foundation stiffnesses (ballast stiffness $k_b = 120\,\mathrm{MN/m}$).

(b) For various ballast stiffnesses (foundation stiffness $k_f = 70\,\mathrm{MN/m}$).

Figure 4. A track receptances comparison, as a function of the ballast/foundation stiffness ratio, and a comparison of the CLM model (dashed lines) with the rigorous FEM model (solid lines).
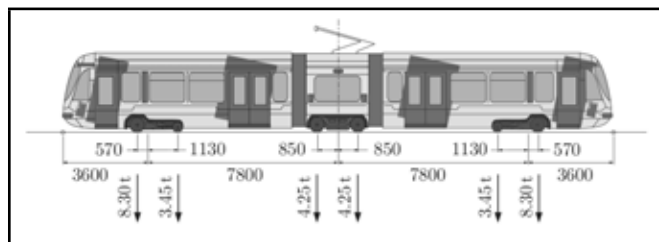

Figure 5. The general configuration of the Tram T2000.

The Brussels tramway network consists of 39% ballasted tracks, 18% clinker pavement, and 28% natural soil pavement. The selected site, Haren, is ballasted and has the advantage of having been previously studied in great detail. The appendix presents all the parameters (vehicle, track, soil) related to the present study.

Regarding the track, it is composed of an EB50T Vignole rail, regularly supported by wood sleepers. The railpad and ballast dynamic parameters (mass, stiffness, and damping) were obtained by updating the numerical vertical receptances from the experimental ones. Various experimental set-ups were used:

- impact tests realized with hammers impact or falling weight (Fig. (5a));

- harmonic tests through an unbalanced motor (Fig. (5b)), ideal for characterising the low-frequency behaviour;

- and static loading with the help of a driving machine (Fig. (5c)), applying a controlled force on the track (track settlement value).

The experimental set-up for evaluating the ground vibrations is presented in Fig. (7). Due to the difficulty of accurately modelling a rail joint, especially for the contact law, pads have been

(a) Impulse machine.

(b) Unbalanced motor.

(c) Static loading.
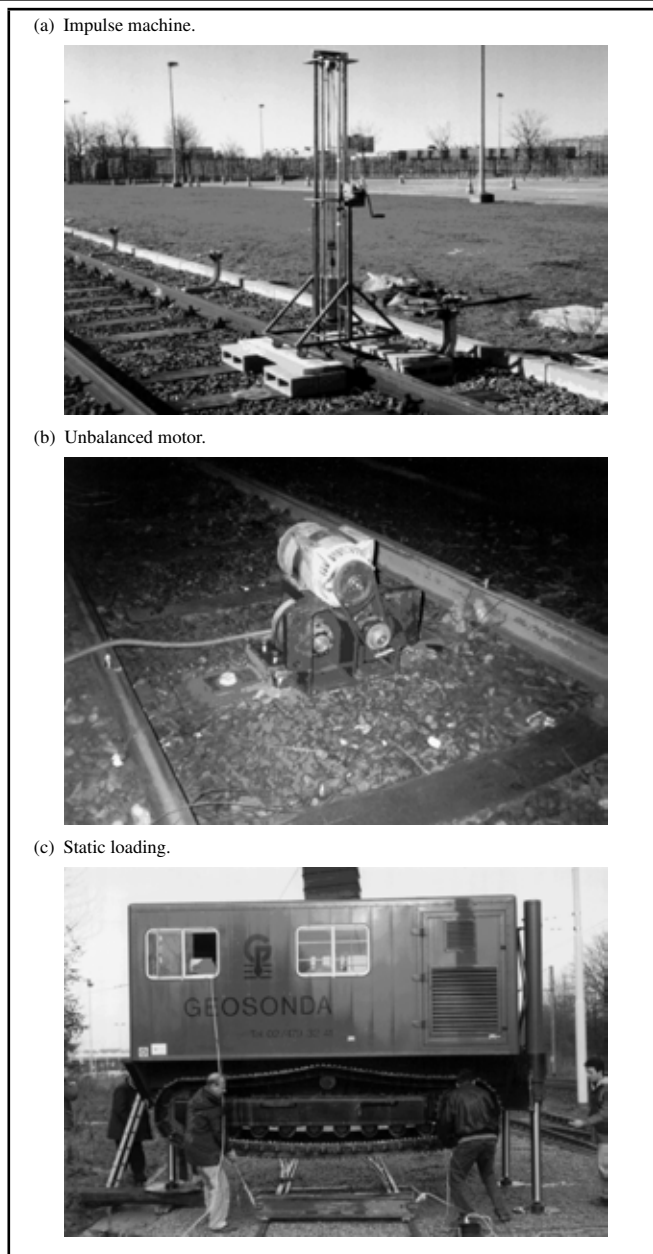
Figure 6. The means of characterisation of the track at the Haren site.

used to represent local defects, as seen in Fig. (6a). Two sensors have been used for the soil vibration recording, one at $2\,\mathrm{m}$ from the track, as seen in Fig. (6b), and one at $8\,\mathrm{m}$.

Singular rail surface defects are of practical significance in urban railway-induced ground vibrations because they represent the main contribution to the vibratory nuisance, the low vehicle speed that limits the quasi-static effect of track deflection. Pads used in the experimental set-up are chosen due to their ability to represent an equivalent realistic local defect. The main advantage is to easily model its dimension profile, taking into account the wheel geometry. Figure (7a) shows the curve defined by the wheel/profile contact height with the corresponding spatial frequency spectra, which can be seen in Fig. (7b). With this kind of defect and at low speed, frequencies up to around $50\,\mathrm{Hz}$ are equally excited (at a tram speed of $30\,\mathrm{km/h}$, a spatial frequency of $8\,\mathrm{m^{-1}}$ corresponds approximatively to a frequency of $70\,\mathrm{Hz}$).

(a) Pad placed on the rail head, representing the local defect.

(b) Sensor placed in the free-field (at 2 m from the track).
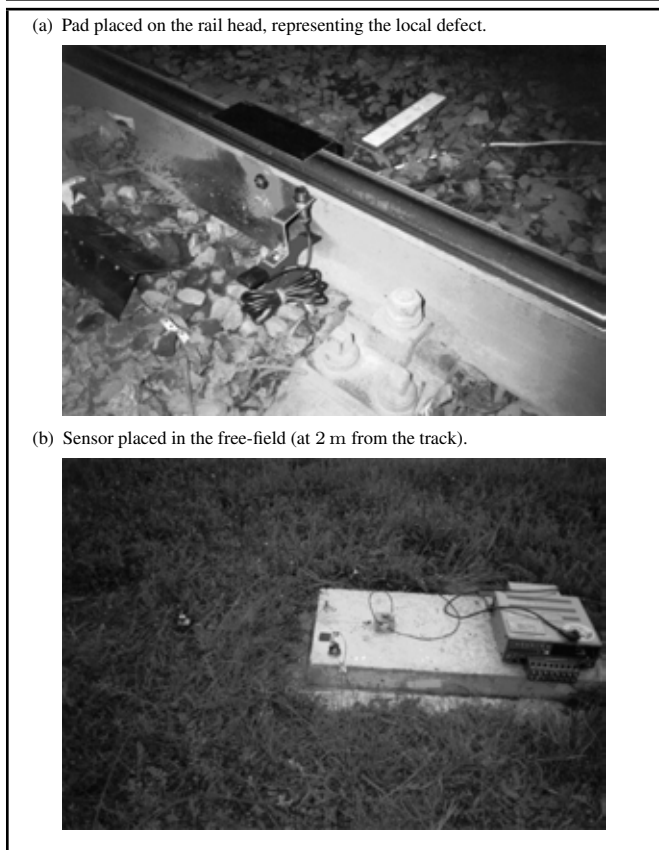
Figure 7. The measurement set-up during the experimental analysis.

(a) Spatial representation.

(b) Spectral representation.

Figure 8. A quantitative analysis of the singular rail surface defect (dashed line: geometry of the rail defect at a height of 1 mm and a length of 5 mm; solid line: wheel/profile contact height taking into account the wheel curvature, where $R = 0.340$ m).

Table 1. The theoretical mode shapes of Tram T2000 in the leading bogie.

	car bounce mode	bogie bounce mode	bogie pitch mode
With rigid track	$f_{01} = 1.8$ Hz $\xi_1 = 32\%$	$f_{02} = 24.7$ Hz $\xi_2 = 15\%$	$f_{03} = 33.9$ Hz $\xi_3 = 6\%$
With flexible track	$f_{01} = 1.7$ Hz $\xi_1 = 32\%$	$f_{02} = 20.4$ Hz $\xi_2 = 14\%$	$f_{03} = 26.6$ Hz $\xi_3 = 8\%$

3.2. Theoretical Modal Analysis of the Vehicle

At this stage, it is interesting to quantify the effect of the vehicle dynamics on the wheel/rail forces, which represents the source of ground vibrations. The Tram T2000 presents the particularity of having bounce and pitch motions in a relatively wide frequency range at different natural frequencies, depending on the bogie type. The leading and the middle bogie present some differences: four motorized wheels for the middle system instead of two for the leading bogie (outer side). Figure (9) shows the vertical impedances of the bogie and the car body frame, when excitation is applied on the front wheels. These curves reveal the influence of the car body-on-suspension bounce mode (between 2 Hz and 3 Hz) and the bogie bounce mode, at around 20 Hz, on the car and bogie motions, respectively. Amplitudes of the response are comparable for leading and middle bogies.

Table 1 presents the vehicle modal analysis results (leading bogie) in order to analyse the effect of the vehicle dynamics under a rigid track or a flexible track. Car-on-body bounce mode, bogie bounce mode, and bogie pitch mode are displayed, with the corresponding natural frequencies f_{0i} and damping ratios ξ_i. The effect of the track flexibility is directly observable on these results. In particular, a decrease from 5 to 20% of the frequency f_0 of the first three modes is observed with the flexibility of the track, demonstrating the strong dependence of vehicle/track coupling in vehicle dynamic analysis. Similar observations are noteworthy for the middle bogie, with a notable influence of the bogie bounce mode.

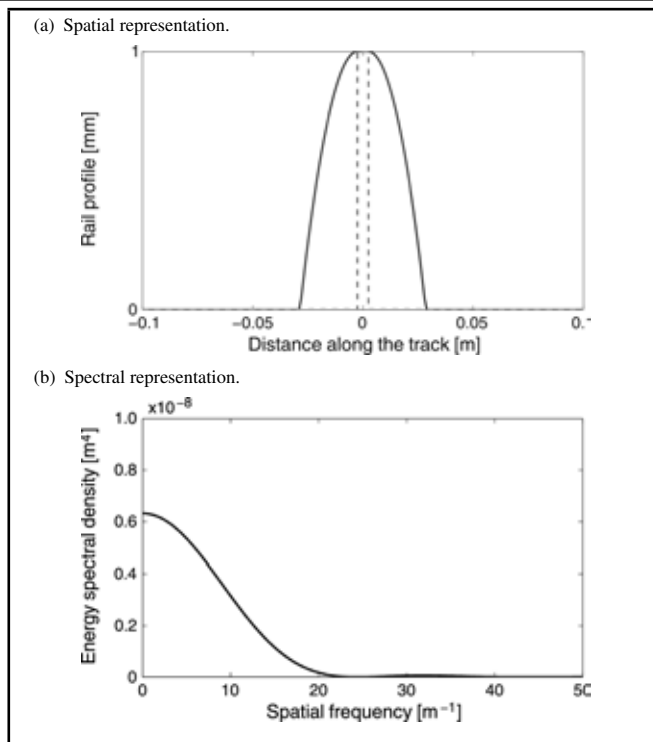The impedances of wheel on rail control the dynamics of their interaction. Figure (10) shows the frequency content of the motor wheel impedances (excitation and response on the wheels), for leading and middle bogies, considering a complete vehicle/track model, with a rigid or a flexible rail. It appears again that the track flexibility plays an important role in the impedance magnitude, which is crucial to an understanding of the wheel/rail interaction. With a flexible track, the wheel impedances decrease in level, with some variations around vehicle natural frequencies up to 70 Hz, which corresponds to the first resonance frequency of the track.[17] Similar results are also obtained with the trailer wheels. The impedance difference, along with the modal analysis results, demonstrates, among other things, the necessity of the vehicle/track coupling in the vehicle and track dynamics, especially when the track presents important roughness or irregularity. The wheel impedance plays an important role in the understanding of wheel/rail interaction. For example, if the wheel impedance is smaller than the one related to the rail at the contact point, important vehicle motions can be developed during the passing of the vehicle on local defects like rail joints, and the wheel/rail coupling cannot be neglected. By comparing these wheel impedances with the defect amplitude spectra displayed at Fig. (7b), we conclude that all modes of the vehicle affecting the wheel impedance are potentially excited when the vehicle rides at low speed on the singular rail surface defect.
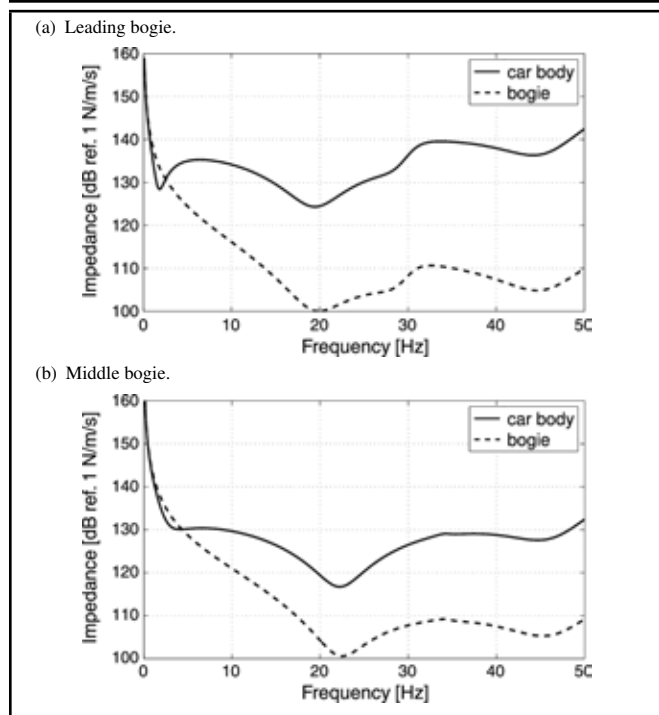
Figure 9. Numerical impedances of the studied tram (excitation on the front wheels).

Figure 10. The numerical spectral content of the direct motor wheel impedances.

3.3. Free-Field Ground Response

The full Tramway T2000 is simulated in a straight line. The proposed model has been validated for this study case in recent analyses,[17, 18] considering free-field vibrations and the simple assumption of the Winkler hypothesis for the foundation concerning the vehicle/track subsystem. Beside the good correspondence obtained between the predicted and measured responses, it has been demonstrated that vibrations of the soil are essentially dominated by bogie pitch mode and, to a lesser degree, by the car body-on-suspension bounce mode, the bogie bounce mode, and the axle hop modes. Soil stratification has also been pointed out as an important modelling parameter associated with vibration levels. The present analysis mainly deals with the interaction of the wheels with rough rail, to check for the soil surface vertical motion, and to compare the possible difference between the two versions of the model with the Winkler and the CLM foundations. Regarding the soil motion calculation, the computational time reaches up to 17 hours for 10 s simulated time using an i–7 computer and hyper-threading technology (the physical four cores constituting the processor can be virtually doubled during the simulation), and this for an explicit scheme. Similar CPU-times were needed for the vehicle/track/foundation model, using, in this case, the implicit Newmark-$1/4$ integration scheme.

Figures (11) and (12) present the results obtained by the simulations (with a Winkler model and a CLM model for the foundation behaviour) and the corresponding experimental results, at speed $v_0 = 30$ km/h on a local defect, besides considering the overall track irregularity. The vibration of the soil is generally described by its velocity, as many standards for vibration use velocity as a primary vibration descriptor of foundations. Some differences clearly appear between the two numerical results, due of course to the track coupling. But the difference is small, and both numerical results are close to the experimental counterparts, proving that the decoupled approach was valid
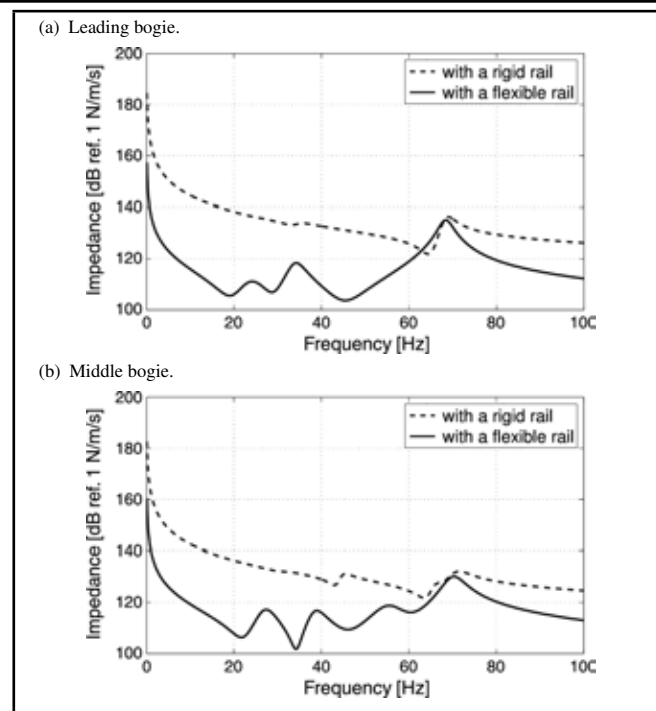
in this case[19] ($k_b/k_f = 0.26$ with k_f the equivalent Winkler foundation stiffness) and is now improved by the CLM model, which can more accurately represent a rigorous model without decoupling. A background noise appearing in the measurement, whose origin is unfortunately unknown, lightly masks the phenomena.

3.4. Modal Analysis of the Building

A building is modelled by finite elements and is representative of typical private, one-floor houses erected during the 20th century. It is composed of reinforced cast concrete and masonry. For the calculations, all the materials involved in the model are supposed to exhibit a linear elastic behaviour. The properties of concrete are in accordance with EN 1992-1 Eurocode standard for concrete structures design (see appendix).

The various vibration modes of the structure in the range of 0–50 Hz are depicted in Fig. (13), with a special focus around 20 Hz. Notice that, due to the symmetry of the building, only half of the structure is displayed. All the displayed modes appear as a combination of flexural and torsional motions of walls and floor, and only the mode at 15.0 Hz can be defined as symmetric. The first vertical bending mode of the upper floor is clearly shown at around 15 Hz, while the flexural motions of walls and other bending modes cover frequencies around 25–30 Hz. More particularly, the secondary bending modes are at 23.8 Hz and 27.0 Hz. Line nodes are presented in mode shapes (Figs. (12c)–(12e)), essentially located at the floor symmetry axes, e.g., in the middle of the first floor, modes at 23.8 Hz, 25.5 Hz, and 27.0 Hz have zero amplitude. All these results are obtained by considering the foundations to be fixed.

Indeed, the presented soil FE model is only dedicated to time domain simulations, since the frequency analysis is not accurate enough, according to the meshing guidelines suggested in.[20] Nonetheless, transient analysis can be performed
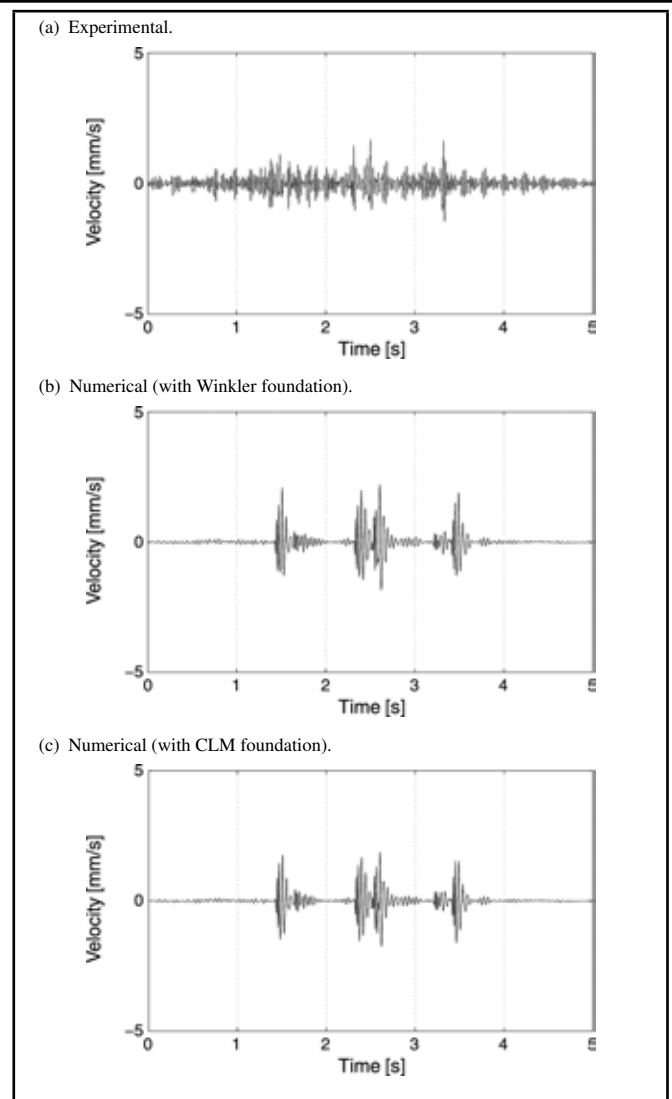
(a) Experimental.

(b) Numerical (with Winkler foundation).

(c) Numerical (with CLM foundation).
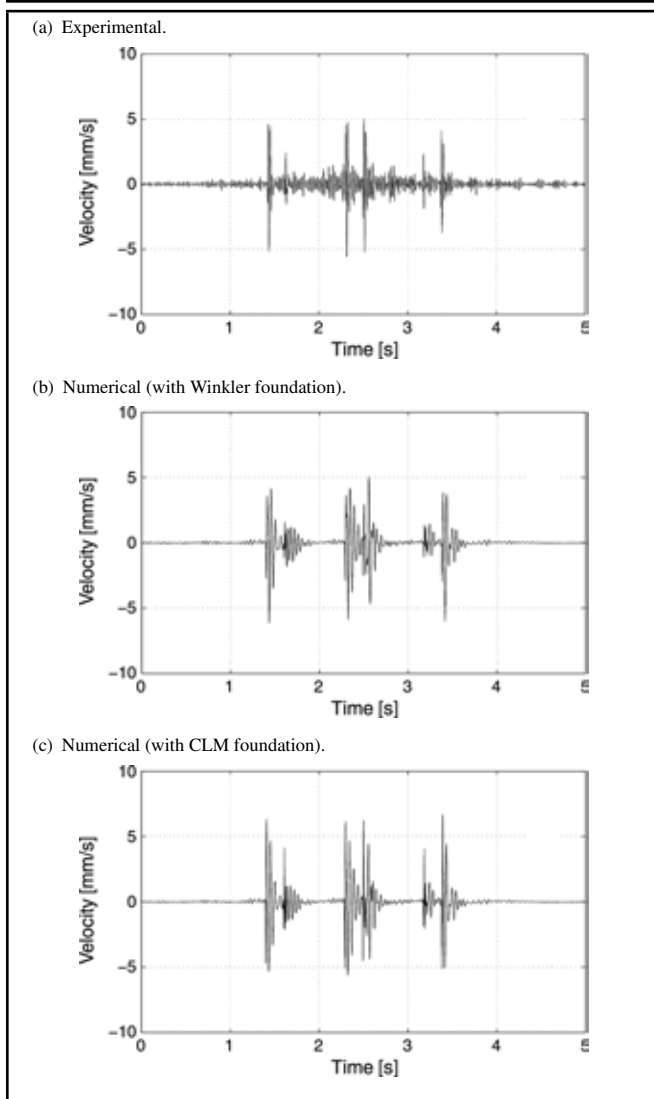
Figure 11. The vertical ground velocity at $2\,\mathrm{m}$ from the track during the passing of the Tram T2008 at the speed $v_0 = 30\,\mathrm{km/h}$ (local defect).

(a) Experimental.

(b) Numerical (with Winkler foundation).

(c) Numerical (with CLM foundation).

Figure 12. The vertical ground velocity at $8\,\mathrm{m}$ from the track during the passing of the Tram T2008 at the speed $v_0 = 30\,\mathrm{km/h}$ (local defect).

for soil/structure models and impact-based modal analysis gets around this problem with the help of the discrete Fourier transform. Calculated transfer functions of the ground and first floors at various locations are shown in Fig. (14), which confirms the results obtained in Fig. (13) for the upper floor vibrations. The ground floor does not have significant resonances in the analysed frequency range and the first floor presents two well-marked peaks, around 15 and 25 Hz, which can be associated with bending modes found by the modal analysis. It can be concluded that a modal analysis of the building, considering a fixed foundation, is sufficient to estimate the upper floor modes.

3.5. Structural Response

This section will try to numerically evaluate the effects of railway vibrations on a typical private house in the vicinity of the track. Since it has been validated in free-field, the proposed model can be used to evaluate the effects of the tram passing near the building. The latter is placed at $4\,\mathrm{m}$ from the track (distance from the front wall to the exterior rail) with the large front wall parallel to the track, which corresponds to a realistic situation often encountered in an urban area. The T2000 Tramway is simulated in a straight line considering a local rail defect, in front of the building.

Figure (15) presents the vertical velocity at the ground and upper floors, with the addition of the equivalent free-field velocity (in red dashed lines). The reference positions are located in the middle of the building width, at three-quarters along the length (location with cross markers in Fig. (14)). Besides the time history, the frequency content and the time-averaged signal are depicted. The latter is defined by the time weighted signal $KB_F(t)$.[22] The impact of each wheel on the local defect is emphasized on the figures, each axle crossing the defect at $t = 1.4\,\mathrm{s}$, $t = 1.6\,\mathrm{s}$, $t = 2.3\,\mathrm{s}$, $t = 2.5\,\mathrm{s}$, $t = 3.2\,\mathrm{s}$, and $t = 3.4\,\mathrm{s}$.

By analysing these results, some important remarks can be made:

- The amplitudes of displayed vibration in ground and upper floors signals are similar, with some discrepancies that are more easily observed in Fig. (16), which represents the seismic wave propagation along a plane perpendicular to the track, and in front of the defect. A decrease in amplitude is shown when the building is taken into account. Frequency contents of free-field and structural responses are also comparable at the ground level, with a maximum between 22 and 24 Hz, corresponding to the bogie pitch
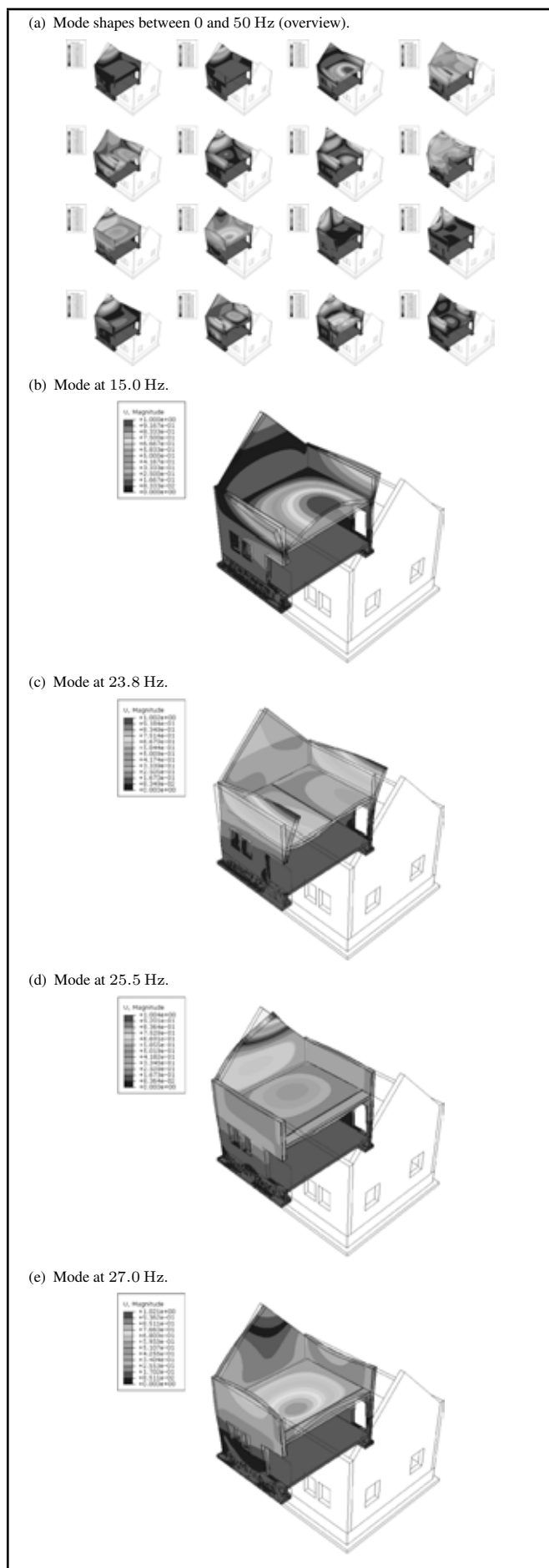
(a) Mode shapes between 0 and 50 Hz (overview).

(b) Mode at 15.0 Hz.

(c) Mode at 23.8 Hz.

(d) Mode at 25.5 Hz.

(e) Mode at 27.0 Hz.

Figure 13. A modal analysis of the building (with fixed boundary conditions).
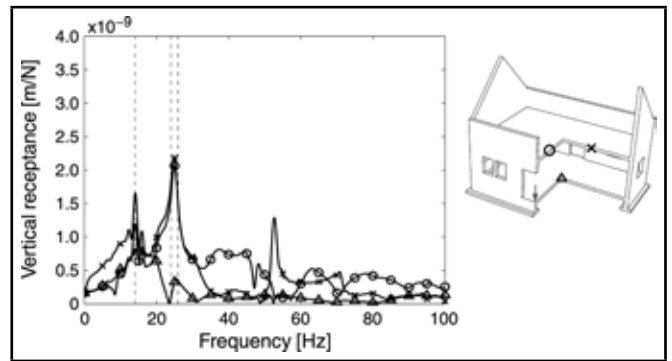

Figure 14. The transfer functions of the building (excitation at the foundation of house).

modes of the vehicle (excitation signature). Notice that no notable difference in amplitude is detected between the ground and the first floor vibrations.

- The main observation, however, is the difference in the frequency content between the ground and the first floor vibrations. The bending modes, at 15 Hz and 27 Hz, clearly dominate the signal, with a complete disappearance of the excitation frequency due to the mode shapes around this frequency. Although each load effect can be distinguished at the ground level, that is less obvious on the first floor.

4. CONCLUSION

This paper presents an overview of the potential of the FE approach, with an accurate prediction of railway excitation, to evaluate the ground-borne vibrations and the building structure's dynamic response due to railway traffic. In order to avoid complicated and heavy models for vehicle/track/soil simulation, a discrete and condensed form of the foundation has been developed, including the coupling through the track contact area. Based on the Lysmer's analogue foundation, spring and damper elements have been included for the purpose of coupling between foundations.

Combined with a two-stages approach, the prediction of railway-induced ground vibrations can be done, through an example issued from the tramway network of Belgium. Frequency analysis on the excitation and the receiver has been performed, in order to reveal the vibration modes dominating the free-field and structural responses. Particularly, the seismic wave propagation is different between the two cases. A complete vehicle/track/soil/structure model is thus necessary to take into account the local coupling between the different substructures. This kind of prediction model, based on the finite element approach and thoroughly validated in free-field case, is presented as a useful tool for predicting the soil/structure dynamics subject to external loads.

APPENDIX A. DETAILS OF THE MEASURED AND CALCULATED PARAMETERS: VEHICLE, TRACK, SOIL, AND BUILDING

The Tram T2000 presented in this paper has the following dynamic properties:

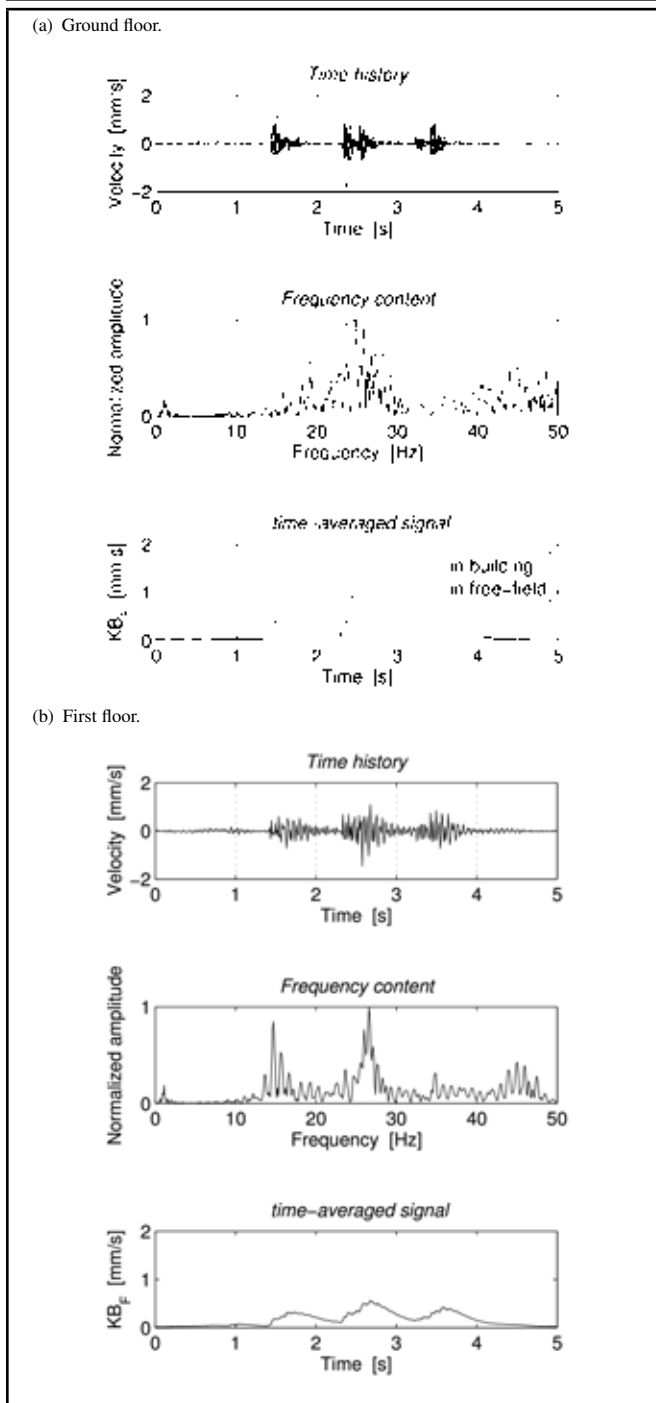- front and rear carbody mass $m_c = 7580$ kg;

(a) Ground floor.

(b) First floor.

Figure 15. The time history, spectral content and time-averaged signal of building vibrations, in the case of a vehicle speed of 30 km/h moving along a track with a local defect.

- central carbody mass $m_{cc} = 2600$ kg;

- bogie mass $m_b = 1800$ kg and pitch inertia $I_b = 300$ kg·m²;

- independent motor wheel mass $m_m = 945$ kg, with a tread of $m_t = 80$ kg, resilient material of stiffness $k_t = 145$ MN/m, and damping $d_t = 3$ kNs/m;

- trailer wheel mass $m_d = 160$ kg;

- primary suspension (trailer wheels) of stiffness $k_d = 5.88$ MN/m and damping $d_d = 6$ kNs/m;
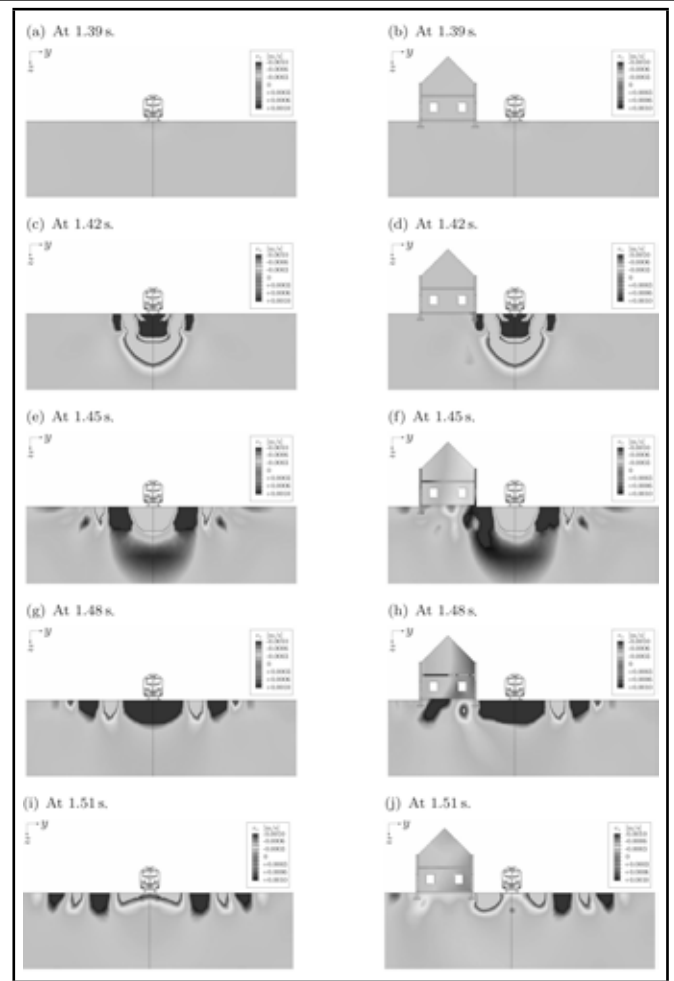

Figure 16. The propagation of the free-field (left) and structural response (right) vertical component of the soil vibration waves, in the case of a vehicle speed of 30 km/h moving along a track with a local defect.

Table 2. Track properties.

Rail flexural stiffness	$E_r I_r$	4.17 MNm²
Rail mass per length	$\rho_r A_r$	54 kg/m
Sleeper spacing	L	0.72 m
Railpad stiffness	k_p	90 MN/m
—— damping	d_p	30 kNs/m
Ballast stiffness	k_b	32 MN/m
—— damping	d_b	52 kNs/m

- primary suspension (motor wheels) of stiffness $k_m = 44$ MN/m and damping $d_m = 18$ kNs/m;

- secondary suspension of stiffness $k_2 = 960$ kN/m and damping $d_2 = 56.25$ kNs/m.

The parameters of the track and the foundation are presented in Table 2. The CLM model parameters associated with a half track are: $m_f = 2502$ kg, $k_f = 30$ MN/m, $k_c = 41$ MN/m, $d_f = 150$ kN/m, and $d_c = -23$ kN/m (see Fig. (3)).

The soil is represented by visco-elastic behaviour, according to a 6-layer configuration proposed by Degrande et al.[23] Values are presented in Table 3, and a progressive soil rigidity with depth is assumed.

The building is a two-story structure with a rectangular plan and an embedded concrete box foundation (depth 0.85 m), and it is representative of typical houses in Brussels. Main dimensions (length × width × height) are 10 m × 7 m × 5 m with the following properties:

Table 3. Soil characteristics and layering.

	Young's Modulus	Density	Poisson's ratio	Viscous damping	Depth
	MPa	kg/m^3	—	s	—
Layer 1	61	1876	0.13	0.0004	1.2
Layer 2	84	1876	0.13	0.0004	1.8
Layer 3	287	1876	0.13	0.0004	1.0
Layer 4	373	1876	0.27	0.0004	1.0
Layer 5	450	1876	0.33	0.0004	1.0
Halfspace	465	1992	0.48	0.0004	—

- Walls are in masonry (Young's modulus $10\,\mathrm{GPa}$, shear modulus $4.2\,\mathrm{GPa}$ and density $1800\,\mathrm{kg/m^3}$), and have a constant thickness of $0.25\,\mathrm{m}$.

- Foundations as well as floors are in concrete (Young's modulus $20\,\mathrm{GPa}$, shear modulus $8.3\,\mathrm{GPa}$, and density $2400\,\mathrm{kg/m^3}$). The floors thickness is equal to $0.20\,\mathrm{m}$.

REFERENCES

[1] Deutsches Institut für Normung. *DIN 4150-3: Structural vibrations—Part 3: Effects of vibration on structures*, (1999).

[2] Crispino, M. and D'Apuzzo, M. Measurement and prediction of traffic-induced vibrations in a heritage building, *Journal of Sound and Vibration*, **246** (2), 319–335, (2001).

[3] Vogiatzis, K. Noise and vibration theoretical evaluation and monitoring program for the protection of the ancient "Kapnikarea Church" from Athens metro operation, *International Review of Civil Engineering*, **1**, 328–333, (2010).

[4] Vogiatzis, K. Protection of the cultural heritage from underground metro vibration and ground-borne noise in Athens centre: the case of the Kerameikos archaeological museum and Gazi cultural centre, *International Journal of Acoustics and Vibration*, **17**, 59–72, (2012).

[5] Auersch, L. Theoretical and experimental excitation force spectra for railway-induced ground vibration: vehicle-track-soil interaction, irregularities, and soil measurements, *Vehicle System Dynamics*, **48** (2), 235–261, (2010).

[6] Auersch, L. Building response due to ground vibration—simple prediction model based on experience with detailed models and measurements, *International Journal of Acoustics and Vibration*, **15** (3), 101–112, (2010).

[7] Metrikine, A. V. and Popp, K.. Vibration of a periodically supported beam on an elastic half-space, *European Journal of Mechanics - A/Solids*, **18** (4), 679–701, (1999).

[8] Sheng, X., Jones, C. J. C., and Thompson, D. J. A theoretical study on the influence of the track on train-induced ground vibration, *Journal of Sound and Vibration*, **272** (3–5), 909–936, (2004).

[9] Lombaert, G. and Degrande, G. Ground-borne vibration due to static and dynamic axle loads of intercity and high-speed trains, *Journal of Sound and Vibration*, **319**, 1036–1066, (2009).

[10] Pyl, L., Degrande, G., Lombaert, G., and Haegeman, W. Validation of a source-receiver model for road traffic induced vibrations in buildings. I: source model, *ASCE Journal of Engineering Mechanics*, **130** (12), 1377–1393, (2004).

[11] Pyl, L., Degrande, G., and Clouteau, D. Validation of a source-receiver model for road traffic induced vibrations in buildings. II: receiver model, *ASCE Journal of Engineering Mechanics*, **130** (12), 1394–1406, (2004).

[12] Ju, S.-H. Finite element investigation of traffic induced vibrations. *Journal of Sound and Vibration*, **321** (3–5), 837–853, (2009).

[13] Harris, C. M. editor. *Shock and Vibration Handbook*, McGraw-Hill, New-York, USA, 6$^{\text{th}}$ edition, (2009).

[14] Dietz, S., Hippmann, G., and Schupp, G. Interaction of vehicles and flexible tracks by co-simulation of multibody vehicle systems and finite element track models, *Vehicle System Dynamics Supplement (The Dynamics of Vehicles on Roads and on Tracks)*, **37**, 372–384, (2002).

[15] Kouroussis, G., Verlinden, O., and Conti, C. Ground propagation of vibrations from railway vehicles using a finite/infinite-element model of the soil, *Proceedings of IMechE, Part F: Journal of Rail and Rapid Transit*, **223** (F4), 405–413, (2009).

[16] Sheng, X., Jones, C. J. C., and Thompson, D. J. Prediction of ground vibration from trains using the wavenumber finite and boundary element methods, *Journal of Sound and Vibration*, **293** (3–5), 575–586, (2006).

[17] Kouroussis, G., Verlinden, O., and Conti, C. On the interest of integrating vehicle dynamics for the ground propagation of vibrations: the case of urban railway traffic, *Vehicle System Dynamics*, **48** (12), 1553–1571, (2010).

[18] Kouroussis, G., Verlinden, O., and Conti, C. Efficiency of resilient wheels on the alleviation of railway ground vibrations, *Proceedings IMechE, Part F: Journal of Rail and Rapid Transit*, **226** (4), 381–396, (2012).

[19] Kouroussis, G., Verlinden, O., and Conti, C. A two-step time simulation of ground vibrations induced by the railway traffic, *Journal of Mechanical Engineering Science*, **226** (2), 454–472, (2012).

[20] Kouroussis, G., Verlinden, O., and Conti, C. Efficiency of the viscous boundary for time domain simulation of railway ground vibration, *17th International Congress on Sound and Vibration (ICSV17)*, Cairo, Egypt, (2010).

[21] Kouroussis, G., Gazetas, G., Anastasopoulos, I., Conti, C., and Verlinden, O. Discrete modelling of vertical track-soil coupling for vehicle-track dynamics, *Soil Dynamics and Earthquake Engineering*, **31** (12), 1711–1723, (2011).

[22] Deutsches Institut für Normung. *DIN 4150-2: Structural vibrations—Part 2: Human exposure to vibration in buildings*, (1999).

[23] Degrande, G., De Roeck, G., Dewulf, W., Van den Broeck, P., and Verlinden, M. Design of a vibration isolating screen, Sas, P. editor, *Proceedings ISMA 21, Noise and Vibration Engineering, Vol. II*, 823–834, Leuven, Belgium, (1996).

Design and Development of a μ-Synthesis Controller for a Flexible Robotic Manipulator, Modelled as a Rotating Euler-Bernoulli Beam

Hamed Moradi, Gholamreza Vossoughi, Firooz Bakhtiari Nejad and Mohammad T. Ahmadian

Department of Mechanical Engineering, Sharif & Amirkabir Universities of Technology, Azadi Street, P.O. Box: 11155-9567, Tehran, Iran

In this paper, a robust control strategy for a robotic manipulator, modelled as a cantilever rotating Euler-Bernoulli beam, is developed. Imprecision in the payload mass, unknown properties of the manipulator link, and torque disturbance are included as the sources of uncertainty. The objective is to achieve a desired angular rotation while the vibration of the manipulator tip is suppressed and the control system remains in a stable region. The control input of the system is an external driving torque. For formulation of the continuous system, the mode summation technique is used and equations of motion are described in the Laplace domain. Then, unstructured uncertainties are included in the form of multiplicative input uncertainty. The μ-synthesis control approach is used and an H_∞ optimal robust controller is developed based on the DK-iteration algorithm. Results show that the designed controller guarantees the robust stability and performance of the perturbed system against existing uncertainties. Consequently, stability of the closed-loop system, disturbance rejection, and trajectory tracking performance are achieved.

1. INTRODUCTION

Robotic manipulators are extensively used in areas such as industrial automation, underwater or space vehicles, manufacturing, material handling (e.g., CNC multi-axes milling machines), and medical surgeries. Flexible manipulators have several advantages over their rigid-arm counterparts, such as less material usage (and, consequently, less weight and energy consumption), smaller actuators, and more manoeuvrability. However, due to the inertia and external forces, light structures are more likely to deflect and vibrate. Therefore, the positioning inaccuracy of the end effector causes the performance of the manipulator to be unacceptable. Mechanical stiffening of the components has been used as a traditional solution to avoid such structural vibrations, which has proved to be ineffective for lightweight flexible manipulators. Consequently, the effects of link flexibility must be considered in the dynamic modelling, as stated by De Wit et al.[1] Thereafter, under external disturbances and parameter variations of the system, effective controllers are required to guarantee the quick and accurate manoeuvrability of manipulators.

Many research studies have been conducted to derive the equations of motion of flexible manipulators and to analyse their dynamics. In the early works, Book,[2] as well as Low and Vidyasagar,[3] derived the equations of motion for both rigid and flexible robot manipulators through Lagrangian formulation. To investigate the generic properties of the structural modelling related to the structural control, Spector and Flasher[4] used distributed sensors on the pinned-free Euler-Bernoulli beam. Choura et al.[5] found the differential equations describing the planar motion of a rotating, thin, flexible beam. Dynamics of a beam experiencing a combination of rotational and translational motions was analysed by Yuh and Young,[6] while its finite element simulation was presented by Gaultier and Cleghorn.[7] Dynamic equations for a planar manipulator with two flexible links, in contact with a constrained surface, have been studied by Matsuno et al.[8] Using Hamilton's principle, equations of motion for a chain of flexible links have been developed through a systematic procedure by Benati and Morro.[9] Damaren and Sharf[10] simulated the constrained motion of flexible-link manipulators, including inertial and geometric nonlinearities.

Fung and Chang[11] studied the dynamic modelling of a nonlinearly constrained flexible manipulator based on four configurations: Timoshenko, Euler, simple flexure, and rigid body beam theories. A linearised dynamic model for multi-link planar flexible manipulators with an arbitrary number of flexible links has been presented by Chen.[12] In that linearised model, flexible links were treated as Euler-Bernoulli beams and the Lagrangian approach was used to establish equations of motion. In addition, Meek and Liu[13] simulated the nonlinear dynamics of flexible manipulators under large overall motions. A study of modelling and the dynamic response of a multi-straight-line path tracing a flexible robot manipulator has been done by Kalyoncu[14] (under the action of an external driving torque and an axial force).

For performance control of the flexible robot manipulators, many control techniques have been developed based on the Euler-Bernoulli beam theory. Point-to-point position control of a flexible beam using the Laplace transform technique has been done by Bhat and Miu.[15] Diken[16] investigated the vibration control of the beam using measured shear force as the feedback, and simultaneously achieved the desired angular rotation by using a PD Controller. Implementation of a neural network tracking controller for a single flexible link has been compared for PD and PID controllers by Gutierrez et al.[17] Due

to a simple control structure, easy implementation, less real-time computational load, and low cost, traditional PID controllers have been extensively used in industrial operations, such as the works done by Gutierrez et al.[17] and A-Ramirez et al.[18]

When a classical controller in the family of PI/PD or PID is designed for a specific dynamic system, and its control gains are tuned appropriately, the desired performance is achieved with bounded values of control efforts. However, in the presence of structured/unstructured model uncertainties, very large actuations are required to achieve precise control and improve the transient performance (in many cases, actuator saturation occurs). This phenomenon has been generally observed in other dynamic systems or processes, as seen in Skogestad and Postlethwaite.[19] Therefore, developing a robust tuning procedure that guarantees the transient performance of robot manipulators is a study that requires further investigation.

Many tracking control algorithms have been developed to make each joint track a desired trajectory. In an early work for the Timoshenko beam, and to achieve tracking with suppression of elastic vibrations, Yuan and Hu[20] designed a non-linear controller using input-output linearization and elastic mode stabilization. Green and Sasiadek[21] studied the dynamics and tracked the optimal control of a two-link flexible manipulator, while Onsay and Akay[22] investigated the vibration reduction of a flexible arm by time optimal control. However, in optimal control approaches, accurate selection of switching time is required (which depends on the system dynamics). Therefore, minor modelling errors cause switching errors and consequently lead to a significant increase in the residual vibrations.

In the field of adaptive control, variable structure set-point control of under-actuated robots—as seen in Su and Leung[23] and Su and Stepanenko[24]—and nonlinear adaptive control via the sliding mode state and perturbation observer, per Jiang and Wu,[25] have been done. However, in these control approaches, a fixed control law is designed based on the priori bound of uncertainty. In addition, for the tracking objective, Huang et al.[26] developed a guaranteed performance adaptive algorithm with limited torque, and Slotine and Li[27] investigated the composite adaptive control for robot manipulators. However, adaptive control techniques are potentially complex and utilize design methods that require *a priori* knowledge of the system model, as seen in Kirchoff and Melek.[28] Therefore, although adaptive control approaches lead to fine control and compensate for structured uncertainties of the manipulators dynamics, they usually fail to appropriately work in the presence of unstructured uncertainties.

Recently, many works have been presented to deal with the problem of the fuzzy control of robot manipulators; e.g., Ha et al.[29] developed a fuzzy sliding mode control. Castillo and Melin[30] used a hybrid fuzzy-neural approach for an intelligent adaptive model-based control of robotic systems. Neuro-fuzzy control of modular and reconfigurable manipulators, as seen in the work of Melek and Goldenberg,[31] and robust control of a spatial robot using fuzzy sliding modes, as appears in Yagiz and Hacioglu,[32] have been investigated. In these neuro-fuzzy control approaches, control law is changed according to certain predefined rules, which depend on the position of the system error states with respect to sliding surfaces. However, implementation of controllers developed based on these methods requires achieving data for structure identification, and designing

its control parameters demands a substantial amount of time.[28]

Robot manipulators as multivariable coupling systems are usually associated with structured and unstructured uncertainties. Imprecision in the payload mass, unknown properties of the manipulator link, and torque disturbance are the sources of structured uncertainties. High frequency parts of the dynamics and un-modelled dynamics, such as disturbance and nonlinear friction, cause the unstructured uncertainties. In contrast with the adaptive and fuzzy based controllers, robust controllers require no accurate knowledge of the system, and their implementation is convenient (an early survey of robust control for robot manipulators has been presented by Sage et al.[33]). Besides the robust-fuzzy[32] and robust-adaptive based control approaches using Lyapunov's direct method,[26, 34] nonlinear H_∞ or mixed H_2/H_∞ control techniques have been developed by Siqueria et al.[35] and Chen et al.[36] Moreover, Karkoub and Tamma[37] studied the μ-synthesis control of flexible manipulators, modelled after the Timoshenko beam theory.

As it is discussed, various strategies have been implemented to solve the tracking problem of manipulators. However, a simultaneous analysis to achieve the desired tracking and vibration suppression while keeping the closed-loop controlled system globally stable has not been investigated, especially when the dynamic model associates with various uncertainties. Therefore, there is still room for a comprehensive control analysis of the problem in the presence of model uncertainties.

In this paper, a robotic manipulator is modelled as a cantilever rotating Euler-Bernoulli beam. To analyze the problem, the mode summation technique is used and equations of motion are described in the Laplace domain. The model is associated with parametric uncertainties caused by imprecision in the payload mass and unknown properties of the manipulator link. After representation of the uncertain system in the form of general control configuration, uncertainties are included in the form of multiplicative input uncertainty. The μ-synthesis control approach is used and an H_∞ robust controller is developed based on the DK-iteration algorithm. Unlike the previous works, both desired angular rotation and suppression of manipulator tip vibration are achieved by manipulation of an external driving torque, as the control input. Simulation results of the manipulator response are presented in the time and frequency domains. Results show that the designed controller guarantees the robust stability and performance of the perturbed system against existing uncertainties.

2. DYNAMICS OF THE ROBOTIC MANIPULATOR

The physical configuration of the single-link flexible manipulator is shown in Fig. 1 where UOV and xoy represent stationary and moving coordinate frames, respectively. The arm and the joint of the manipulator are assumed to be flexible. To simulate the effect of a gripped payload, a mass attached to the arm tip is considered. With the assumption of a long and slender manipulator, transverse shear and rotary inertia effects are neglected. Therefore, the Euler-Bernoulli beam theory can be used to model the elastic behaviour of the manipulator, per Mohamed and Tokhi.[38] In addition, the mass and flexible properties are assumed to be distributed uniformly along the flexible link. According to the formulation developed by White and Heppler,[39] by neglecting the effect of shear, the equations
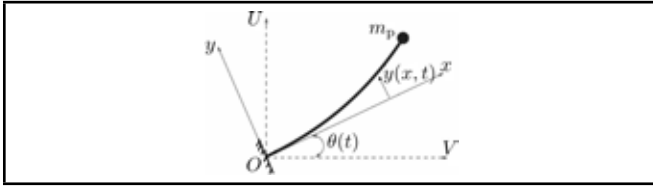
Figure 1. Schematic of the flexible manipulator.

of motion for the Timoshenko beam are reduced for the Euler-Bernoulli one as follows:[16]

$$EI\frac{\partial^4 y(x,t)}{\partial x^4} + \rho\frac{\partial^2 y(x,t)}{\partial t^2} = \rho x\frac{\partial^2 \theta}{\partial t^2} - m_{\rm p}\frac{\partial^2 y(l,t)}{\partial t^2}; \quad (1)$$

$$J_{\rm tot}\frac{\partial^2 \theta}{\partial t^2} + \int_0^t \rho\left(\frac{\partial^2 y(x,t)}{\partial t^2}\right)x dx + m_{\rm p}l\frac{\partial^2 y(l,t)}{\partial t^2} = \tau; \quad (2)$$

$$J_{\rm tot} = \frac{J_{\rm m}}{n^2} + J_{\rm b}.$$

For Eqs. (1) and (2), EI is the flexural rigidity, y is the beam deflection measured with respect to the xoy coordinate, ρ is the mass per unit length, $m_{\rm p}$ is the payload mass, θ is the rotational angle, and τ is the motor torque with respect to the beam axis. In the aforementioned equations, $J_{\rm tot}$ is the total mass moment of inertia including the motor inertia $J_{\rm m}$ and the beam inertia $J_{\rm b}$, and n is the gear ratio between the beam and motor rotational angles. Beam deflection at any point x can be expressed in terms of the normal modes $\phi_i(x)$ as follows:[40]

$$y(x,t) = \sum_i q_i(t)\phi_i(x); \quad (3)$$

where $q_i(t)$ is the i-th generalized coordinate. For a cantilever Euler-Bernoulli beam, the eigenvector at any mode is given as[40]

$$\phi_i(x) = A_i[\cosh\lambda_i x - \cos\lambda_i x - \mu_i(\sinh\lambda_i x - \sin\lambda_i x)]; \quad (4)$$

$$\mu_i = (\cosh\lambda_i + \cos\lambda_i)/(\sinh\lambda_i + \sin\lambda_i) \quad (5)$$

and the natural frequencies of a cantilever beam are defined as

$$\omega_i = \left(\frac{\lambda_i}{l}\right)^2\sqrt{\frac{EI}{\rho}}; \quad (6)$$

where values of λ_i are constants taking values of $\lambda_1 = 1.88$, $\lambda_2 = 4.69$, and $\lambda_3 = 7.85$ for the first three natural frequencies. Normal modes, $\phi_i(x)$, are orthogonal functions that satisfy the following relationship:

$$A_i^2\int\phi_i(x)\phi_i(x) = 1. \quad (7)$$

Substituting Eqs. (4) and (5) in Eq. (7) results in $A_i = 1$. Substituting Eq. (3) in Eq. (1) and multiplying the resulting equation by $\phi_j(x)$, as well as using the orthogonal characteristics of the modes as

$$\int_0^l \phi_i(x)\phi_j(x)dx = \begin{cases} 1 & \text{for } i = j \\ 0 & \text{for } i \neq j \end{cases} \quad (8)$$

yields

$$\ddot{q}_i + \tilde{\omega}_i^2 q_i = \alpha_i^*\ddot{\theta} \quad (9)$$

Figure 2. General schematic of the closed-loop control system.

and

$$\tilde{\omega}_i^2 = \frac{\omega_i^2}{1 + \Gamma_i}; \quad (10)$$

$$\alpha_i^* = \frac{1}{1 + \Gamma_i}\frac{\int_0^l x\varphi_i(x)dx}{\int_0^l \varphi_i^2(x)dx}; \quad (11)$$

$$\Gamma_i = \frac{m_{\rm p}}{\rho}\frac{\int_0^l \varphi_i(l)\varphi_i(x)dx}{\int_0^l \varphi_i^2(x)dx}. \quad (12)$$

Similarly, substituting Eq. (3) in Eq. (2) yields

$$\ddot{\theta} + \sum \gamma_i\ddot{q}_i = \frac{\tau}{J_{\rm tot}} \quad (13)$$

and

$$\gamma_i = \frac{1}{J_{\rm tot}}\left\{\rho\int_0^l x\varphi_i(x)dx + m_{\rm p}l\varphi_i(l)\right\}. \quad (14)$$

Multiplying Eq. (13) by α_i^*, and substituting $\alpha_i^*\ddot{\theta}$ from Eq. (9) yields

$$\beta_i(\ddot{q}_i + \tilde{\omega}_i^2 q_i) + \sum_j \eta_j\ddot{q}_j = \tau \quad (15)$$

and

$$\beta_i = \frac{J_{\rm tot}}{\alpha_i^*}; \quad (16)$$

$$\eta_j = J_{\rm tot}\gamma_j; \quad (17)$$

while transforming Eq. (15) into the Laplace domain results in

$$\beta_i(s^2 + \tilde{\omega}_i^2)Q_i(s) + \sum_j \eta_j s^2 Q_j(s) = \tau(s). \quad (18)$$

Expanding Eq. (18) for two modes ($i, j = 1, 2$) (the reason for considering two modes is discussed next in section 4) and solving the set of equations for $Q_1(s)$ and $Q_2(s)$ yields the following:

$$\begin{bmatrix} Q_1(s) \\ Q_2(s) \end{bmatrix} = \frac{\tau(s)}{D(s)} \cdot$$
$$\cdot \begin{bmatrix} (\beta_2 + \eta_2)s^2 + \beta_2\tilde{\omega}_2^2 & -\eta_2 s^2 \\ -\eta_1 s^2 & (\beta_1 + \eta_1)s^2 + \beta_1\tilde{\omega}_1^2 \end{bmatrix}\begin{bmatrix} 1 \\ 1 \end{bmatrix}; \quad (19)$$

$$D(s) = [(\beta_1 + \eta_1)s^2 + \beta_1\tilde{\omega}_1^2][(\beta_2 + \eta_2)s^2 + \beta_2\tilde{\omega}_2^2] - \eta_1\eta_2 s^4. \quad (20)$$

3. H_∞ ROBUST CONTROL DESIGN

Figure 2 shows a general schematic of the designed closed-loop control system and its components are described in a schematic of the H_∞ control design, shown in Fig. 3. Variables r, $\bar{y}$, e, u, d, and d_i are the reference input, output variables, tracking error, controlled system input, output disturbance, and input disturbance, respectively. Signals $\tilde{y}$, $\tilde{e}$, and $\tilde{u}$ are weighted with the weighting functions $W_{\rm m}$, $W_{\rm p}$, and $W_{\rm u}$.

According to the Fig. 3, the transfer function between the output and the disturbance (y/d), and between the tracking
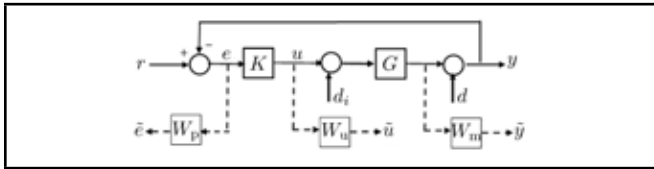
Figure 3. Components of the H_∞ control design.
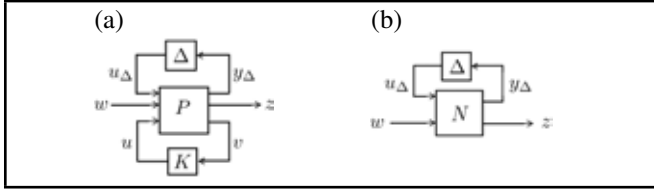
Figure 4. General control configuration in the presence of model uncertainty is used for (a) synthesis (b) analysis.

error and the reference input (e/r), is explained by $S = (I + GK)^{-1}$, which is called the sensitivity transfer function. Moreover, the complementary sensitivity function, $T = GK(I + GK)^{-1}$, describes the transfer function between the output and the reference input (y/r). In addition, the control signal is explained in terms of the reference input, output, and input disturbance as $u = KS(r - d - Gd_i)$. Consequently, to achieve disturbance rejection and appropriate transient performance, $\|S\|_\infty$ must be small while for the perfect tracking, $|T(j\omega)|$ must have unit value (because for perfect tracking, $y = r$.

At low frequencies, the performance weight W_p must be large enough to achieve a desired nominal performance. At high frequencies, the upper bound function W_m on the possible multiplicative uncertainties must be large enough. Due to the constraint $S + T = I$ (identity), it is not possible to make both of them simultaneously small. Therefore, the weighted sensitivity function, $\|W_p S\|_\infty$, and complementary sensitivity function, $\|W_m T\|_\infty$, are minimized. In addition, to restrict the magnitude of the control effort, the upper bound $1/|W_u|$ on the magnitude of KS must be small. To achieve these conditions, a stacking mixed sensitivity approach is used, as follows:

$$\|N\|_\infty = \max_\omega \bar{\sigma}(N(j\omega)) < 1;$$

$$N = \|W_p S \quad W_u KS \quad W_m T\|_\infty.$$

At each frequency, the size of the matrix N is determined by computing the maximum singular value $\bar{\sigma}(N(j\omega))$. The stabilizing H_∞ optimal controller is determined by minimizing the function $\|N(K)\|_\infty$.[19]

3.1. General Control Configurations in Terms of $N - \Delta$ Structure

To include the existing uncertainties in the closed-loop system shown in Fig. 2, the general control configuration is used, as shown in Fig. 4, where P and K are the generalized plant and controller. Possible perturbations are included in the block diagonal matrix Δ, which is normalized such that $\|\Delta\|_\infty \leq 1$. The block diagram of Fig. 4a, in which P is closed through a lower loop by K, is transformed into the block diagram in terms of N as shown in Fig. 4b. Using lower linear fractional transformation (LFT) results in (see Appendix A):

$$N = F_L(P, K) = P_{11} + P_{12}K(I - P_{22}K)^{-1}P_{21}.$$

Using an upper linear fractional transformation (LFT) for the N_Δ structure, the perturbed (uncertain) transfer function from external inputs w to external outputs z is evaluated as

$$z = F_u(N, \Delta)w; \tag{21}$$

$$F_u(N, \Delta) = N_{22} + N_{21}\Delta(I - N_{11}\Delta)^{-1}N_{12}. \tag{22}$$

3.2. Stability and Performance Analysis for the Uncertain System

The structured singular value μ is used to analyze nominal performance (NP), robust stability (RS), and robust performance (RP) of the uncertain system (see Appendix B). After representation of the uncertain system in the form of $N - \Delta$ structure, using Eqs. (21) and (22), and considering the RP requirement as $\|F\|_\infty \leq 1$ for all possible perturbations, the conditions of nominal stability/performance and robust stability/performance become[19]

$$NS \Leftrightarrow N \text{ (internally stable)}; \tag{23}$$

$$NP \Leftrightarrow \bar{\sigma}(N_{22}) = \mu_{\Delta_P} < 1, \ \forall\omega, \text{ and } NS; \tag{24}$$

$$RS \Leftrightarrow \mu_\Delta(N_{11}) < 1, \ \forall\omega, \text{ and } NS; \tag{25}$$

$$RP \Leftrightarrow \mu_{\hat{\Delta}}(N) < 1, \ \forall\omega, \text{ and } NS; \tag{26}$$

$$\hat{\Delta} = \begin{bmatrix} \Delta & 0 \\ 0 & \Delta_P \end{bmatrix}; \tag{27}$$

$$N = \begin{bmatrix} W_m T_I & W_I KS \\ W_p SG & W_p S \end{bmatrix}; \tag{28}$$

and

$$T_I = KG(I + KG)^{-1}; \tag{29}$$

$$S = (I + GK)^{-1}; \tag{30}$$

where the detailed structure of the block diagonal matrix Δ depends on the existing uncertainty and Δ_P is always a full complex matrix, indicating the H_∞ performance specification.

4. SIMULATION OF THE CONTROL DESIGN, RESULTS, AND DISCUSSION

The mass and flexible properties are assumed to be distributed uniformly along the flexible manipulator. For physical simulation of the problem, a steel type flexible manipulator of dimensions $1000 \times 30 \times 2.5 \, \text{mm}^3$, Young's modulus of the elasticity $E = 210 \times 10^9 \, \text{N/m}^2$, area moment of inertia $I = 39.1 \, \text{mm}^4$, mass density per length $\rho = 0.585 \, \text{kg/m}$, and mass moment of inertia of beam $J_b = 0.195 \, \text{kg m}^2$ with payload mass of $m_p = 0.25 \, \text{kg}$ is considered. With the assumption of the ratio $J_m/J_b n^2$ to be the unit, the total mass moment of inertia becomes $J_{tot} = 2J_b = 0.39 \, \text{kg m}^2$. Consequently, according to the governing equations in the modelling section, the nominal values of the parameters for the two first modes of the flexible arm, given by Eqs. (10)–(12) and (16)–(17), are found as follows:

$$\bar{\beta}_1 = 1.15, \tag{31}$$

$$\bar{\beta}_2 = 2.68, \tag{32}$$

$$\bar{\eta}_1 = 0.83, \tag{33}$$

$$\bar{\eta}_2 = -0.45, \qquad (34)$$

$$\bar{\bar{\omega}}_1 = 10.2, \qquad (35)$$

$$\bar{\bar{\omega}}_2 = 104.1. \qquad (36)$$

It should be mentioned that according to Eq. (6), the natural frequencies of the considered cantilever beam are proportional with the coefficients $\lambda_i^2, i = 1, 2, 3, \ldots$, while $\lambda_1 = 1.88$, $\lambda_2 = 4.69$, and $\lambda_3 = 7.85$. Consequently, the second and third natural frequencies (ω_2, ω_3) are about 6 and 17 times of the first one (ω_1). These frequencies are sufficiently far away from the first natural frequency. Under such conditions and for the considered model here, the higher modes are not excited (and if excited, have a negligible effect on time responses of the dynamic system). Therefore, considering two modes in the expansion of Eq. (18) is physically enough (even in prior research[16] only one mode was considered).

However, it should be noted that for other cases of robotic manipulators, in which the flexural rigidity is reduced greatly, the inclusion of higher modes is necessary. In that case, the procedure used in this research can be easily extended in a straight forward manner to the models with higher numbers of modes.

4.1. Description of the Uncertain Model

The various sources of model uncertainty are classified into parametric (real) and dynamic (frequency-dependent). The first type occurs when the model structure is known, but some of the parameters are uncertain. The second type is caused by the missing dynamics, usually at high frequencies where the model is in error. In this paper, the imprecision in the payload mass and unknown properties of the manipulator link are considered as the parametric uncertainties. As a real case study, assume that the physical parameters of the manipulator and payload mass are varied around their nominal values so that it results in variation of parameters, e.g., with $\pm 25\%$ uncertainty as follows:

$$0.75\bar{\chi} < \chi < 1.25\bar{\chi} \qquad (37)$$

where χ can take any values of β_i, η_i, and $\tilde{\omega}_i$, $i = 1, 2$ for the two first modes of the flexible manipulator, given by Eqs. (31)–(36).

4.2. Complex Uncertainty and Performance Weight Functions

Frequency domain analysis is used to quantify the parametric uncertainties, resulting in complex perturbations normalized as $\|\Delta\|_\infty \leq 1$. In many practical cases, the configuration of multiplicative input uncertainty is used to represent the various sources of dynamic uncertainty, as shown in Fig. 5. In this approach, the perturbed plant $G_p(s)$ is described as

$$G_p(s) = G(s)[1 + W_m(s)\Delta_I(s)]; \quad \underbrace{|\Delta_I(j\omega)| \leq 1 \ \forall \omega}_{\|\Delta_I\|_\infty \leq 1}$$

where the $G(s)$ is the nominal plant and $\Delta_I(s)$ is any stable transfer function with a magnitude less or equal to 1, at each frequency. The original complex uncertainty $G_p(s)$ is replaced by a conservative disc type approximation $G_p'(s)$ of
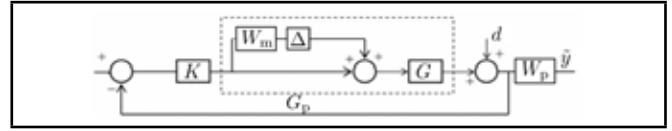

Figure 5. Uncertain plant including multiplicative input uncertainty.
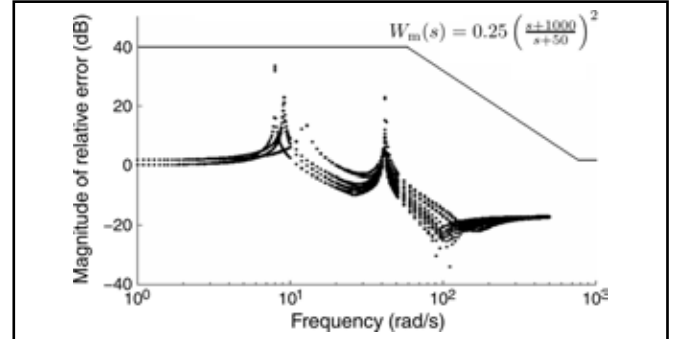

Figure 6. Relative errors $|(G_p - G)/G|$ for 2^6 perturbed plants.

radius $|W_m(j\omega)G(j\omega)|$, where the weight function W_m is determined as[19]

$$l_I(\omega) = \max_{G_p \in \Pi} \left| \frac{G_p(j\omega)}{G(j\omega)} - 1 \right|, \quad |W_m(j\omega)| \geq l_I(\omega), \ \forall \omega,$$

where Π is the set of possible perturbed plants and $G(s)$ is a 2×2 matrix given by Eqs. (19) and (20). As shown in Fig. 6, the relative plant errors $|G_p/G - 1|$ are plotted for 2^6 possible perturbed plants (because any of parameters β_i, η_i, and $\tilde{\omega}_i$, $i = 1, 2$ can take two extreme limits, given by Eqs. (31)–(36) and (37)), where some plots are coincide. According to this figure, the weight function of the model uncertainty, the upper bound on relative error functions, is found as

$$W_m(s) = 0.25 \left(\frac{s + 1000}{s + 50} \right)^2. \qquad (38)$$

At the low frequencies, the weight function $1/|W_P|$ as the upper bound on the sensitivity function $|S|$ is equal to the parameter A (typically $A \approx 0$) in correlation with the steady state tracking error. At the high frequencies, it approaches to the maximum peak amplitude $M \geq 1$, and the bandwidth frequency (ω_B^*) indicates the speed of the time response. An appropriate performance weight W_P is described in terms of these parameters as[19]

$$W_P = \frac{s/M + \omega_B^*}{s + \omega_B^* A}.$$

For instance, to have a desired step response with a maximum overshoot of 10 percent, the rise time of about 1.5 s, and a perfect tracking (error ≈ 0), the performance weight is selected as

$$W_P(s) = \frac{s/1.1 + 1.82}{s + 2 \times 10^{-4}}. \qquad (39)$$

4.3. μ-Synthesis Controller Design Based on the DK-iteration Algorithm

In the robust H_∞ technique, DK-iteration is an effective practical approach used to find the μ-optimal controller. In
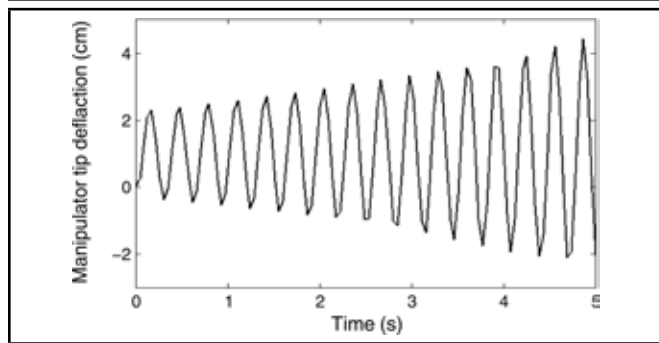
Figure 7. Manipulator tip deflection after applying the robust controller designed in the first stage.

this method, sources of uncertainty are represented by the perturbation blocks Δ_i, normalized as $\|\Delta_i\| \leq 1$. According to Fig. 4, the problem is to find the controller K that produces the control signal u to counteract the influence of w on z by minimizing the closed loop norm $\|T_{wz}\|_\infty$.

Using a μ-synthesis code and a DK-iteration algorithm developed in the Robust Control Toolbox of MATLAB, an H_∞ robust controller of the 16-order is obtained. Using the same toolbox, this controller is reduced to a second order controller as follows:

$$K = \frac{1}{(s+0.005)(s+0.14)} \begin{bmatrix} s+0.24 & s+0.25 \\ s+0.51 & s+0.59 \end{bmatrix}. \quad (40)$$

Figure 15 (as seen in the Appendix) shows the Bode diagram of the 16-order and reduced second order robust controllers to validate the correctness of this approximation. The matrix transfer function $[G(s)]$ is derived from Eq. (19) as follows:

$$G(s) = \begin{bmatrix} G_{11} & G_{12} \\ G_{21} & G_{22} \end{bmatrix} =$$
$$= \frac{1}{D(s)} \begin{bmatrix} (\beta_2+\eta_2)s^2 + \beta_2\tilde{\omega}_2^2 & -\eta_2 s^2 \\ -\eta_1 s^2 & (\beta_1+\eta_1)s^2 + \beta_1\tilde{\omega}_1^2 \end{bmatrix}; \quad (41)$$

where $D(s)$ is given in Eq. (20). However, applying this reduced second order controller on the uncertain plant, e.g., a plant with the parameters $\beta_i = 1.2\bar{\beta}_i$, $\eta_i = 0.8\bar{\eta}_i$, and $\omega_i = \bar{\omega}_i$, $i = 1, 2$, results in an unstable time response. For instance, Fig. 7 shows the unstable time response of the manipulator tip deflection, found from Eq. (3), after applying the robust controller. The reason is that although the designed control given by Eq. (40) is stable, the transfer function $[KG^*]$ is unstable where

$$G_{11}^* = G_{21}^* = G_{11} + G_{12}; \quad (42)$$

$$G_{12}^* = G_{22}^* = G_{21} + G_{22}. \quad (43)$$

Figure 8 shows the root locus of the transfer functions $K_{11}G_{11}^*$ and $K_{22}G_{22}^*$ (root locus of the transfer functions $K_{21}G_{21}^*$ and $K_{12}G_{12}^*$ is similar to that of $K_{11}G_{11}^*$ and $K_{22}G_{22}^*$, respectively). As it is shown, due to the existence of the eigenvalues with positive real parts, using $[KG^*]$ results in unstable time responses. To overcome this problem, two more iterations are included in the μ-synthesis. After developing the
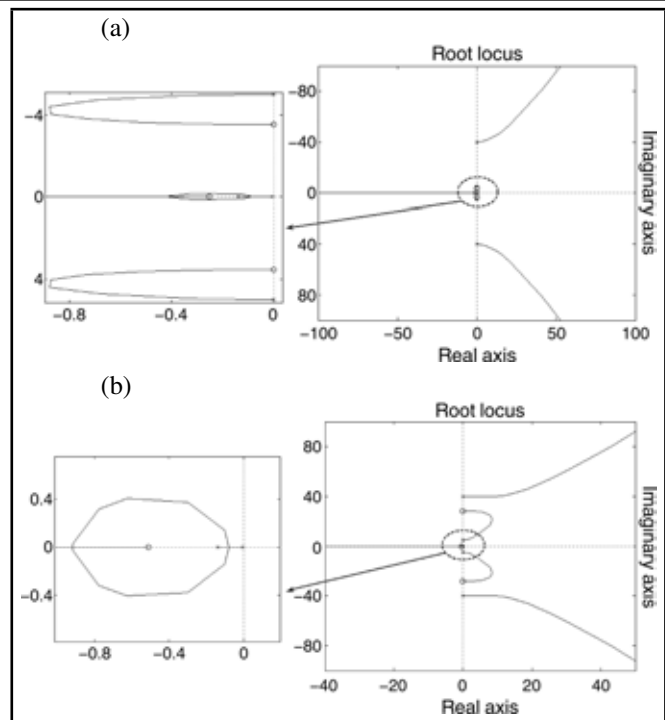
Figure 8. The root locus of the transfer functions (a) $K_{11}G_{11}^*$ (or $K_{21}G_{21}^*$) and (b) $K_{22}G_{22}^*$ (or $K_{12}G_{12}^*$).

code, the optimal robust controller is modified as follows:

$$\hat{K} = \frac{1}{(s+0.005)(s+0.14)(s+10)} \times$$
$$\times \begin{bmatrix} (s+0.24)(s^2+16) & (s+0.25)(s^2+1200) \\ (s+0.51)(s^2+16) & (s+0.59)(s^2+1200) \end{bmatrix}. \quad (44)$$

Figure 9 shows the root locus of the transfer functions $\hat{K}_{11}G_{11}^*$ and $\hat{K}_{22}G_{22}^*$.

Since the transfer functions $G(s)$, $\hat{K}(s)$, $\hat{K}(s)G(s)$, and consequently $S(s)$, $S(s)G(s)$, $\hat{K}(s)S(s)$, and $T(s)$ are stable, the system is nominally stable (NS).[19] Comparing Eqs. (23)–(26) and (27)–(30) shows that the condition for nominal performance (NP), robust stability (RS) and robust performance (RP) are the satisfaction of $\|W_PS\|_\infty \leq 1$, $\|W_mT\|_\infty \leq 1$, and $\|N\|_\infty \leq 1$, respectively. Figure 10 shows the μ-plots after applying the optimal robust controller. As it is shown, all robust stability, nominal performance, and robust performance are achieved. According to this figure, $\|W_mT\|_\infty = 0.2$, which indicates that before the worst case uncertainty yields instability, the uncertainty may increase by a factor of $1/0.2 = 5$.

Consider that a trajectory tracking from the initial rotational angle $\theta_0 = 0$ to the final value $\theta_d = 35°$ is desired while the manipulator tip vibration is suppressed. Figure 11 shows the rotational angle for the nominal plant and the uncertain plant with parameters, i.e., $\beta_i = 1.2\bar{\beta}_i$, $\eta_i = 0.8\bar{\eta}_i$, and $\omega_i = \bar{\omega}_i$, $i = 1, 2$. As expected, the desired characteristics of the time response, described through the performance weight in Eq. (39), are achieved. Additionally, as shown in Fig. 12, after applying the optimal robust controller, the manipulator tip vibration is suppressed. As this figure shows, during the suppression process, the uncertain plant oscillates with overall larger vibration amplitudes with respect to the nominal plant.

Figure 13 shows the μ-plot for $\|KS\|_\infty$, which indicates no saturation in the control signal τ (because $\|KS\|_\infty \leq 1$). The
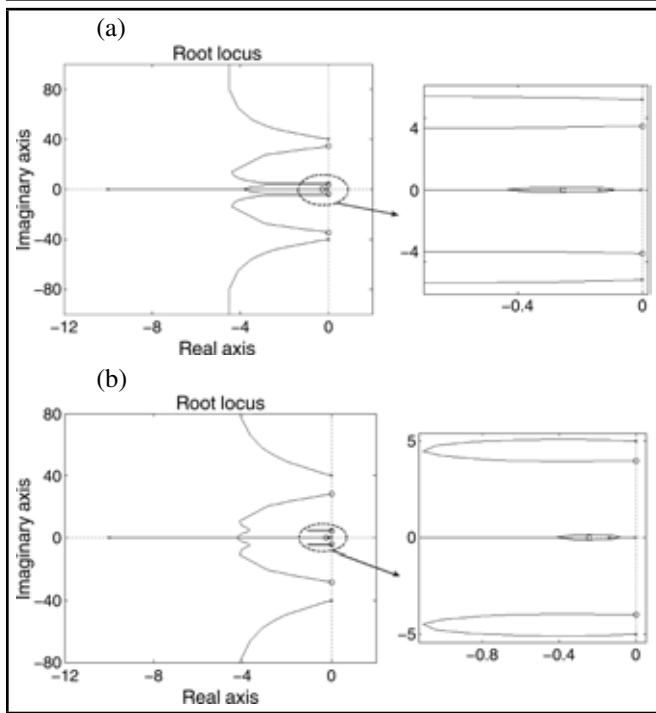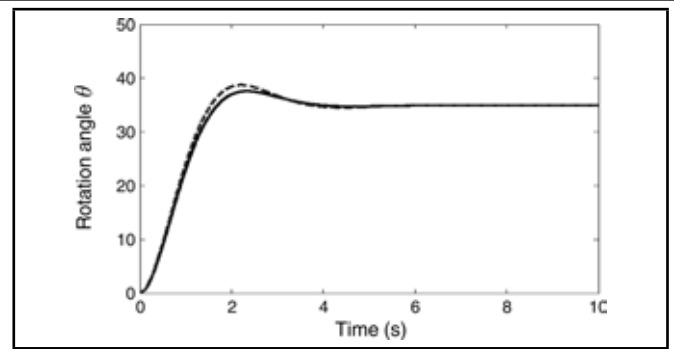
Figure 9. The root locus of the transfer functions (a) $\hat{K}_{11}G_{11}^*$ (or $\hat{K}_{21}G_{21}^*$) and (b) $\hat{K}_{22}G_{22}^*$ (or $\hat{K}_{12}G_{12}^*$).
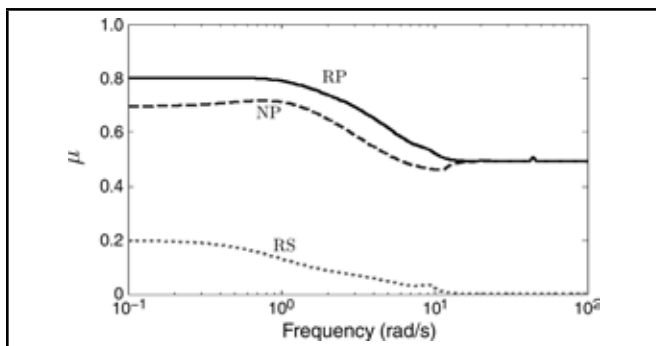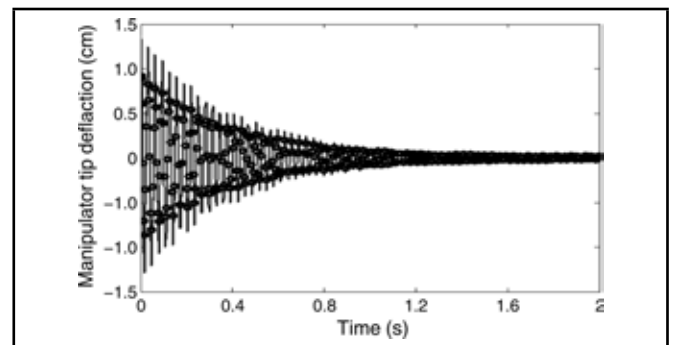

Figure 10. μ-plots of nominal performance (NP: dashed line), robust stability (RS: dots) and robust performance (RP: solid line) for the manipulator system with modified optimal robust controller.

Figure 11. Rotational angle response to the desired valued $\theta_{\rm d} = 35°$ for the nominal (solid line) and uncertain (dashed line) plants.

Figure 12. Manipulator tip deflection after applying the optimal robust controller for nominal (circles) and uncertain plants (solid line).
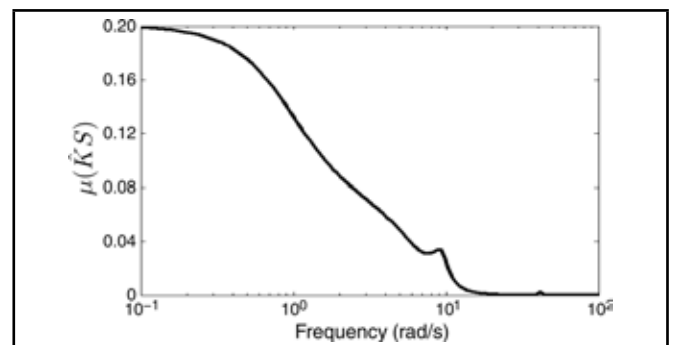

Figure 13. μ-plots for the transfer function $\hat{K}S$ with the modified optimal robust controller.

motor torque, as the control effort, is shown in Fig. 14. As it is shown and physically expected, for performance tracking and vibration suppression, the uncertain plant requires more motor torque.

It should be mentioned that the main hindrance of the proposed H_∞ control strategy is the implementation of high-order controllers, which may associate with high real-time computational load (in practice). For instance, in this research, using the proposed robust control approach leads to the 16-order controller. This controller was efficiently approximated with a second order controller, as illustrated in the Appendix (the initial controller is given by Eq. (40)). Similarly, the modified controller given by Eq. (44) is a third-order controller, obtained via reduction in a high-order one. In the majority of dynamic systems, such reduction in a controller's order is possible.[19] However, there may be some cases in which such approximation of high-order controllers to the low-order ones cannot be realized.

5. CONCLUSIONS

In this paper, an H_∞ optimal robust controller is designed to improve the performance of a rotating robotic manipulator. The Euler-Bernoulli beam theory is used to develop the dynamic model of the rotating manipulator. The mode summation technique is applied to develop the formulation in terms of general coordinates in the Laplace domain. The parametric sources of uncertainty, such as the imprecision in the payload mass and unknown properties of the manipulator link, are included.

After representation of the uncertain system in the form of the $N - \Delta$ structure, uncertainties are included in the form of multiplicative input uncertainty. The μ-synthesis control approach is used and an H_∞ robust controller is developed based on the DK-iteration algorithm. However, due to the internal instability, this controller cannot guarantee the robust stability of the uncertain system. To overcome this problem, root locus analysis is used and a modified optimal robust controller is
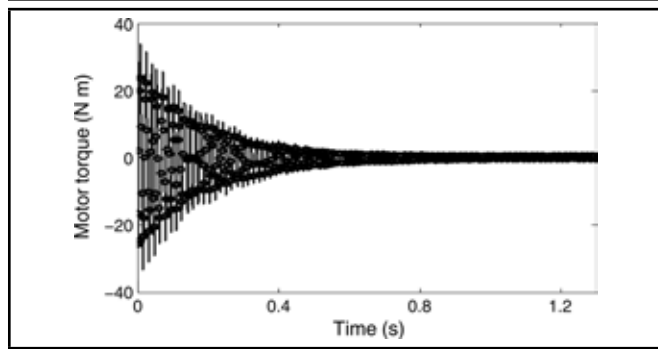
Figure 14. Required motor torque for the nominal (circles) and uncertain (solid line) plants.

designed after two more algorithm iterations.

Results show that in the presence of parametric uncertainties, robust stability and performance and nominal performance are achieved after applying the designed controller. Therefore, both the desired angular rotation and the suppression of manipulator tip vibration are achieved by manipulation of an external driving torque while the stability of the uncertain system is also guaranteed. In comparison with the nominal plant, to achieve the desired angular rotation and vibration suppression, uncertain plant requires larger motor torque.

A. LOWER AND UPPER LINEAR FRACTIONAL TRANSFORMATION

Consider a matrix P of dimension $(n_1 + n_2) \times (m_1 + m_2)$ and partition it as[19]

$$P = \begin{bmatrix} P_{11} & P_{12} \\ P_{21} & P_{22} \end{bmatrix}. \qquad (45)$$

Let the matrices Δ and K have dimensions $(m_1 \times n_1)$ and $(m_2 \times n_2)$, respectively (compatible with upper and lower partitions of P). The following notation for the lower and upper linear fractional transformation is defined as:

$$F_{\mathrm{L}}(P, K) \triangleq P_{11} + P_{12}K(I - P_{22}K)^{-1}P_{21} \qquad (46)$$

and

$$F_{\mathrm{u}}(P, \Delta) \triangleq P_{22} + P_{21}\Delta(I - P_{11}\Delta)^{-1}P_{12}. \qquad (47)$$

B. STRUCTURAL SINGULAR VALUE

Let M be a given complex matrix and $\Delta = \mathrm{diag}\{\Delta_i\}$ denote a set of complex matrices, with $\bar{\sigma}(\Delta) \leq 1$ and a given block diagonal structure in which some of blocks may be repeated and some of the blocks may be restricted to be real. Real non-negative function $\mu(\Delta)$, called the structured singular value, is defined by[19]

$$\mu(M) =$$
$$= \frac{1}{\min\{k_{\mathrm{m}}|\det(I - k_{\mathrm{m}}\Delta M) = 0 \text{ for structure } \Delta; \bar{\sigma}(\Delta) \leq 1\}}.$$

If no such structured Δ exists, then $\mu(M) = 0$. A value of $\mu = 1$ means that there exists a perturbation with $\bar{\sigma}(\Delta) = 1$, which is just large enough to make $I - M\Delta$ singular. A small value of μ is desired, as it means that a larger perturbation makes $I - M\Delta$ singular.
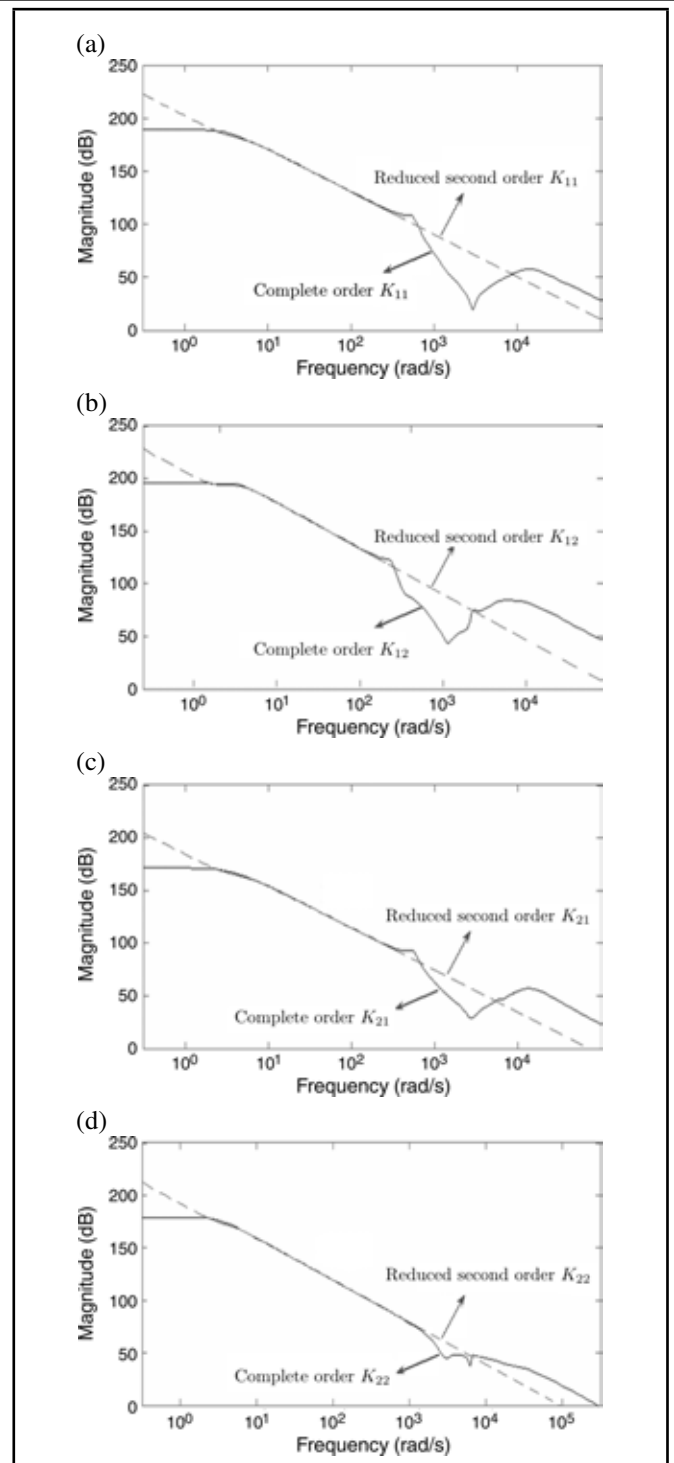

Figure 15. Bode diagrams of K_{11} (a), K_{12} (b), K_{21} (c), and K_{22} (d) of the 16-order (solid line) and reduced second order (dashed line) robust controllers.

C. COMPARING THE ROBUST AND PID CONTROL APPROACHES ON THE PERFORMANCE OF THE NOMINAL PLANT

As it was already discussed, the family of classical controllers including PI, PD, and PID cannot guarantee the robust stability and performance of the model in the presence of uncertainties. Here, for the nominal plant, a comparison between the proposed robust control strategy and PID control is presented through Figs. 16–18. The Simulink Toolbox of Matlab is used for implementation of the PID controller. Due to the well-known design of PID controller, its formulation is not
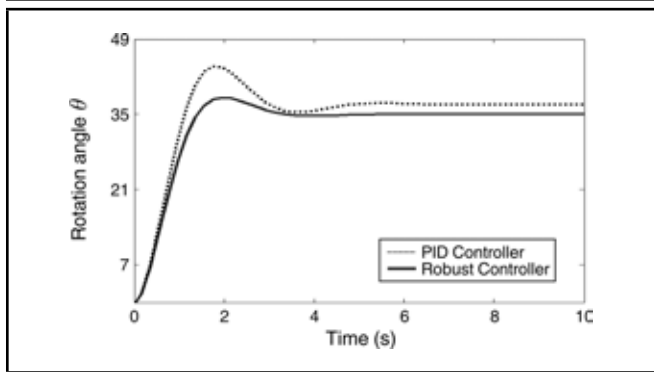
Figure 16. Rotational angle response to the desired value $\theta_{\mathrm{d}} = 35°$ for the nominal model after implementation of the optimal robust controller (solid line) and a classical PID controller (dashed line).
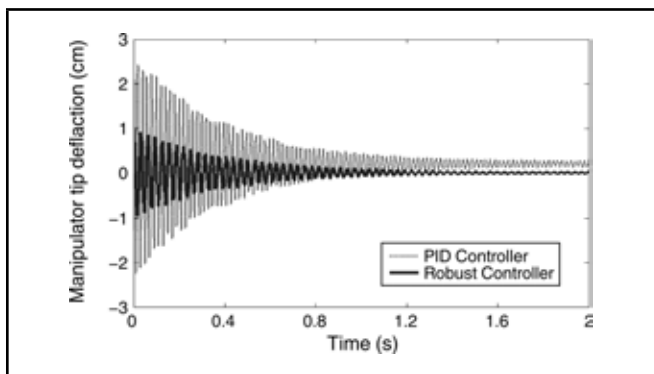
Figure 17. Manipulator tip deflection for the nominal model after implementation of the optimal robust controller (solid line) and a classical PID controller (dashed line).
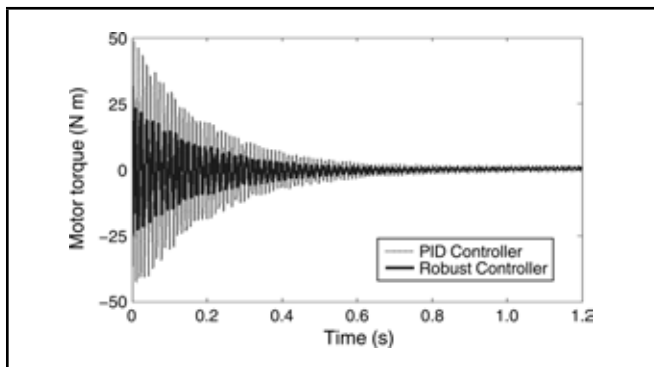
Figure 18. Required motor torque for the nominal model after implementation of the optimal robust controller (solid line) and a classical PID controller (dashed line).

presented. According to Figs. 16 and 17, when the PID controller is implemented, more oscillatory behaviour is observed for both the angular rotation and the manipulator tip deflection. In addition, time responses of these variables associate with steady state error. As it is shown in Fig. 18, more motor torque is required when the PID controller is applied.

REFERENCES

[1] DeWit, C. C., Siciliano, B., and Bastin, G. *Theory of robot control*, Springer, London, (1996).

[2] Book, W. J. Recursive Lagrangian dynamics of flexible manipulator arms, *Int. Journal of Robotic Research*, **3** (3), 87–101, (1984).

[3] Low, K. H. and Vidyasagar, M. A Lagrangian formulation of the dynamic model for flexible manipulator systems, *ASME Journal of Dynamic Systems, Measurement & Control*, **110**, 175–181, (1988).

[4] Spector, V. A. and Flasher, H. Modeling and design implications of noncolocated control in flexible systems, *ASME Journal of Dynamic Systems, Measurements & Control*, **112**, 186–193 (1990).

[5] Choura, S., Jayasuriya, S., and Medick, M. A. On the modelling, and open-loop control of a rotating thin flexible beam, *ASME Journal of Dynamic Systems, Measurement & Control,* **113**, 26–33, (1991).

[6] Yuh, J. and Young, T. Dynamic modeling of an axially moving beam in rotation: simulation and experiment, *ASME Journal of Dynamic Systems, Measurement & Control*, **113**, 34–40, (1991).

[7] Gaultier, P.E. and Cleghorn, W.L. A spatially translating and rotating beam finite element for modeling flexible manipulators, *Journal of Mechanism & Machine Theory*, **27** (4), 415–433, (1992).

[8] Matsuno, F., Asano, T., and Sakawa, Y. Modeling and quasi-static hybrid position/force control of constrained planar two-link flexible manipulators, *IEEE Transactions on Robotics & Automation*, **10**, 287–297, (1994).

[9] Benati, M. and Morro, A. Formulation of equations of motion for a chain of flexible links using Hamilton's principle, *ASME Journal of Dynamic Systems, Measurement & Control*, **116**, 81–88, (1994).

[10] Damaren, C. and Sharf, I. Simulation of flexible-link manipulators with inertial and geometric nonlinearities, *ASME Journal of Dynamic Systems, Measurement & Control*, **117**, 74–87, (1995).

[11] Fung, R.F. and Chang, H.C. Dynamic modelling of a nonlinearly constrained flexible manipulator with a tip mass by Hamilton's principle, *Journal of Sound & Vibration*, **216** (5), 751–69, (1998).

[12] Chen, W. Dynamic modelling of multi-link flexible robotic manipulators, *Journal of Computers & Structures*, **79**, 183–95, (2001).

[13] Meek, J.L. and Liu, H. Nonlinear dynamics analysis of flexible beams under large overall motions and the flexible manipulator simulation, *Journal of Computers & Structures*, **56** (1), 1–14, (1995).

[14] Kalyoncu, M. Mathematical modelling and dynamic response of a multi-straight-line path tracing flexible robot manipulator with rotating-prismatic joint, *Journal of Applied Mathematical Modelling*, **32**, 1087–1098, (2008).

[15] Bhat, S. P. and Miu, D. K. Experiments on point to point position control of a flexible beam using Laplace transform technique-part II: closed loop, *ASME Journal of Dynamic Systems, Measurement & Control*, **113**, 438–443, (1991).

[16] Diken, H. Vibration control of a rotating Euler-Bernoulli Beam, *Journal of Sound & Vibration*, **232** (3), 541–551, (2000).

[17] Gutierrez, L. B., Lewis, F. L., and Lowe, J. A. Implementation of a neural network tracking controller for a single flexible link: comparison with PD and PID controller, *IEEE Trans. Industrial Electronics*, **45** (2), 307–318, (1998).

[18] A-Ramirez, J., Cervantes, I., and Kelly, R. PID regulation of robot manipulators: stability and performance, *Journal of Systems & Control Letters*, **41**, 73–83, (2000).

[19] Skogestad, S. and Postlethwaite, I. *Multivariable Feedback Control*, John Wiley and Sons, New York, (2005).

[20] Yuan, K. and Hu, C. M. Nonlinear modeling and partial linearizing control of a slewing Timoshenko beam, *ASME Journal of Dynamic Systems, Measurement & Control*, **118**, 75–83, (1996).

[21] Green, A. and Sasiadek, J. Z. Dynamics and trajectory tracking control of a two-link robot manipulator, *Journal of Vibration & Control*, **10** (10), 1415–1440, (2004).

[22] Onsay, T. and Akay, A. Vibration reduction of a flexible arm by time optimal open-loop control, *Journal of Sound & Vibration*, **147** (2), 283–300, (1991).

[23] Su, C. Y. and Leung, T. P. A sliding mode controller with bound estimation for robot manipulators, *IEEE Trans. Robotics Automation*, **9**, 208–214, (1993).

[24] Su, C. Y. and Stepanenko, Y. Adaptive variable structure set-point control of underactuated robots, *IEEE Transaction of Automotic Control*, **44** (11), 2090–2093, (1999).

[25] Jiang, L. and Wu, Q. H. Nonlinear adaptive control via sliding model state and perturbation observer, *IEEE Proceedings of Control Theory Applications*, **149** (4), 269–277, (2002).

[26] Huang, C. Q., Peng, X. F., Jia, C. Z., and Huang, J. D. Guaranteed robustness/performance adaptive control with limited torque for robot manipulators, *Journal of Mechatronics*, **18**, 641–652, (2008).

[27] Slotine, J. E. and Li, W. Composite adaptive control of robot manipulator, *Journal of Automatica*, **25**, 509–519, (1989).

[28] Kirchoff, S. and Melek, W. W. A saturation-type robust controller for modular manipulators arms, *Journal of Mechatronics*, **17**, 175–190, (2007).

[29] Ha, Q. P., Rye, D. C., and Whyte, H. D. F. Fuzzy moving sliding mode control with application to robotic manipulators, *Journal of Automatica*, **35** (4), 607–616, (1999).

[30] Castillo, O. and Melin, P. Intelligent adaptive model-based control of robotic dynamic systems with a hybrid fuzzy-neural approach, *Journal of Applied Soft Computing*, **3**, 363–378, (2003).

[31] Melek, W. and Goldenberg, A. Neurofuzzy control of modular and reconfigurable robots, *IEEE/ASME Transactions on Mechatronics*, 381–389, (2003).

[32] Yagiz, N. and Hacioglu, Y. Robust control of a spatial robot using fuzzy sliding modes, *Journal of Mathematical & Computer Modelling*, **49**, 114–127, (2009).

[33] Sage, H.G., De Mathelin, M. F., and Ostertag, E. Robust control of robot manipulators: a survey, *Int. Journal of Control*, **72** (16), 1498–1522, (1999).

[34] Torres, S., Mendez, J. A., Acosta, L., and Becerra, V. M. On the improving the performance in robust controllers for robot manipulators with parametric disturbances, *Journal of Control Engineering Practice*, **15**, 557–566, (2007).

[35] Siqueria, A. G., Terra, M. H., and Maciel, B. C. O. Nonlinear mixed H_2/H_∞ control applied to manipulators via actuation redundancy, *Journal of Control Engineering Practice*, **14**, 327–335, (2006).

[36] Chen, B. S., Lee, T. S., and Feng, J. H. A nonlinear H_∞ control design in robotic systems under parameter perturbation and external disturbance, *Int. Journal of Control*, **59**, 439–461, (1994).

[37] Karkoub, M. and Tamma, T. Modelling and μ-synthesis control of flexible manipulators, *Journal of Computers & Structures*, **79**, 543–551, (2001).

[38] Mohamed, Z. and Tokhi, M. O. Command shaping techniques for vibration control of a flexible robot manipulator, *Journal of Mechatronics*, **14**, 69–90, (2004).

[39] White, M. W. and Heppler, G. R. Vibration of a rotating Timoshenko beam, *ASME Journal of Vibration & Acoustics*, **118**, 607–613, (1996).

[40] Inman, D. J. *Engineering Vibration*, Prentice Hall Int. Inc., Englewood, NJ, (1994).

A Parametric Shock Analysis of Spade-Less, Lightweight, Wheeled, Military Vehicles Subjected To Cannon Firing Impact: A Feasibility Study of Spade Removal

Ashkan Haji Hosseinloo

School of Mechanical and Aerospace Engineering, Nanyang Technological University, 50 Nanyang Avenue, Singapore 639798, Singapore

Nader Vahdati

Department of Mechanical Engineering, The Petroleum Institute, PO Box 2533, Abu Dhabi, UAE

Fook Fah Yap

School of Mechanical and Aerospace Engineering, Nanyang Technological University, 50 Nanyang Avenue, Singapore 639798, Singapore

Tracked military vehicles are being replaced by their lightweight wheeled counterparts in many armies around the world. However, mounting high calibre artillery guns on lightweight, wheeled vehicles may bring about problems such as crew discomfort, vehicle slide, lift-off, turnover, and etc. To avoid these problems, spades are used to connect the vehicle to the ground which in turn reduces the vehicle mobility. Furthermore, the optimum spade design for different vehicles and soils is a difficult if not impossible task to accomplish. In this paper, a spade-less, four-wheeled vehicle with a mounted mortar is modelled, and the effects of the firing impact amplitude, duration, and elevation angle on vehicle response are investigated. It is found that all of the likely problems can be avoided if appropriate precautions are taken, except for firing inaccuracy at very high bomb charges. Therefore, for many cases, it is feasible to remove the spades.

NOMENCLATURE

F_r	Recoil force
m_r	Recoil mass
m_{tr}	Rear unsprung mass
m_{tf}	Front unsprung mass
m_c	Mortar-chassis mass
m_{ch}	Chassis mass
m_{mor}	Mortar mass
I_c	Mortar-chassis mass moment of inertia
I_{ch}	Chassis mass moment of inertia
I_{mor}	Mortar mass moment of inertia
k_r	Recoil stiffness
k_{cr}	Rear suspension stiffness
k_{cf}	Front suspension stiffness
k_{tr}	Rear tire stiffness
k_{tf}	Front tire stiffness
k_{hr}	Rear horizontal stiffness of chassis
k_{hf}	Front horizontal stiffness of chassis
c_r	Recoil damping coefficient
c_{cr}	Rear suspension damping coefficient
c_{cf}	Front suspension damping coefficient
c_{tr}	Rear tire damping coefficient
c_{tf}	Front tire damping coefficient
c_{hr}	Rear horizontal damping coefficient of chassis
c_{hf}	Front horizontal damping coefficient of chassis
L	Vehicle wheelbase
a	Distance from mortar-chassis centre of gravity to front of the car
b	Distance from mortar-chassis centre of gravity to rear of the car
c	Horizontal distance from mortar-chassis centre of gravity to mortar connection point to chassis
f	Distance from mortar centre of gravity to its connection point to chassis
e	Distance from chassis centre of gravity to rear of the car
d	Distance from chassis centre of gravity to front of the car
h	Horizontal distance from chassis centre of gravity to mortar connection point to chassis
α	Mortar elevation angle from horizon
h_c	Vertical distance from mortar-chassis centre of gravity to mortar connection point to chassis
h_r	Vertical distance from mortar-chassis centre of gravity to rear suspension
h_f	Vertical distance from mortar-chassis centre of gravity to front suspension

h_{cf} Vertical distance from chassis centre of gravity to front suspension

h_{cr} Vertical distance from chassis centre of gravity to rear suspension

h_{ch} Vertical distance from chassis centre of gravity to mortar connection point to chassis

y_{cg} Vertical distance from chassis centre of gravity to that of mortar-chassis system

1. INTRODUCTION

Many armies' vision of their future is a lighter, faster, and a more lethal fighting force. The U.S. Army's Future Combat Systems Multi-Role Fighting Vehicle is an example of the application of this vision.[1] To this end, tracked military vehicles are being replaced by their wheeled counterparts in many armies around the world, due to their higher mobility and lower maintenance needs.[2]

Artillery cannons and mortars are installed on both tracked and wheeled military vehicles, and the heavier the chassis is, the larger the cannon (with higher firing power) that will be used. However, for defeating threats at greater distances and yet still maintaining vehicle mobility, mounting higher calibre guns on lightweight vehicles, in particular wheeled vehicles is of great interest. On the other hand, the transmission of high firing impact force on the chassis of light vehicles may bring about problems such as crew discomfort, vehicle slide, lift-off, turnover, tire blowout, firing inaccuracy, and bottoming out of the suspension dampers. To avoid these problems, the chassis of the light vehicle is usually connected to the ground with spades, thereby transmitting a part of the recoil force to the ground. But the use of spades contradicts with the agile shoot and scoot capabilities of wheeled vehicles in the counter-battery fire. Figure 1 depicts a High Mobility Multi-Purpose Wheeled Vehicle (HMMWV) with a mounted high calibre mortar and spades.

Since the spades reduce the mobility of the wheeled military vehicles and the optimum spade design for different vehicles and soils is a difficult if not impossible task to accomplish, it is very interesting to see if it is feasible to eliminate the spades without introducing substantial problems. To this end, a good realization of the dynamics of an integrated spade-less vehicle-mortar system is needed. Then the effects of the firing impact on the system should be extensively investigated and the likelihood of the potential problems should be thoroughly assessed.

Fraud and Donnard[4] patented a new design of spades for military vehicles that made use of a retractable suspension for the spades. They claimed their design would help for quicker shoot and scoot though they did not eliminate the spades. Prior experience with the M551 Sheridan, a light tank first put into production by the United States in 1966, raised concern that firing large calibre armaments from lightweight spade-less vehicles may result in unacceptable crew discomfort and vehicle reaction during recoil.[5] Therefore, they conducted several experiments to define the transmitted acceleration to the crew in these vehicles, in order to assess crew discomfort levels.[6,7] Later, when the United States Marine Corps (USMC) was concerned that the 105 mm gun recoil could have an adverse effect
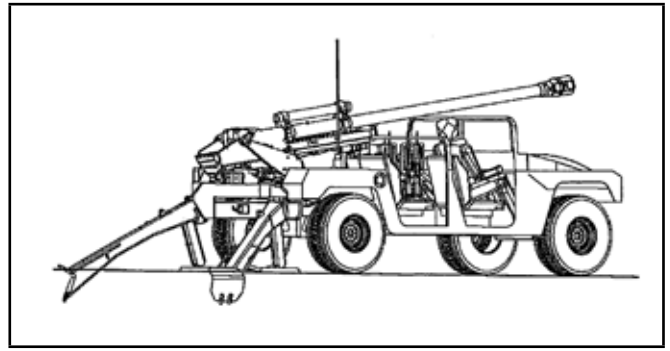

Figure 1. The HMMWV with mounted mortar and spades.[3]

on their Light Armoured Vehicle (LAV), the Ballistic Research Laboratory (BRL) was summoned to investigate the problem.[8] They were particularly concerned about the turnover of the vehicle when it was canted. They tested the system at two cant angles (0 and -10 degrees) and four azimuth angles (0, 30, 60 and 90 degrees) for three different recoil systems for a stationary and a moving vehicle. They concluded that no turnover would occur in any of the scenarios. However, they did not investigate the effect of the elevation angle, which can significantly affect the impact moment on the vehicle, and therefore the results and the overturn risk. Moreover, there was no parametric analysis so that one could extend it to other vehicles or mortar systems.

Another impact of high recoil force on the chassis when the spades are removed is the introduced firing inaccuracy due to the increased vibration of the chassis. Large, heavy vehicles, such as the Abrams tank and the Bradley fighting vehicle, not only will not be affected so much by the recoil impact, but they also have high-cost gun turrets that are controlled by very expensive, fully-stabilized gun sights, to accurately position the weapon muzzle on the target. However, small and lightweight vehicles, such as HMMWVs, cannot justify such expensive gun turrets or fully-stabilized sights. Therefore, to improve the accuracy of the weapon firing from a small lightweight vehicle, the US Army Research Laboratory (ARL) developed the Inertial Reticle Technology (IRT).[9] They replaced the conventional sight with a video camera and the weapon mounting plate with an actively controlled turret, which was automatically controlled by two motors. However, adding a camera and an active control system adds more complexity to the system, in addition to its higher cost.

There are very few analytical studies on integrated vehicle-mortar systems. These few analyses are all about tracked heavy vehicles. Shengtao studied a heavy tracked tank to see if the vehicle would turn over when the spade was eliminated.[10] He modelled the tank in the simplest way–as a one degree-of-freedom rigid body–and then studied whether the offset between the firing force and the centre of gravity of the tank would cause the vehicle to turn over. He concluded that for large gun-to-vehicle ratios, the spade is needed to avoid having the vehicle tip over. Most recently, Balla modelled an integrated, tracked, vehicle-mortar system and studied its firing stability and accuracy.[11,12] However, many other potential problems were not assessed, such as the effect of the firing charge or the elevation angle on firing accuracy, vehicle slide, vehicle turnover, etc.

In their previous study, the authors developed a mathematical model for a spade-less integrated mortar-vehicle system and tried to employ semi-active primary suspensions to reduce the vehicles heave, pitch and fore-aft vibrations, and to improve its firing accuracy.[13,14] The authors used a particular mortar system with fixed bomb charge (force amplitude and duration) and fixed elevation angle. However, different bomb charges and elevation angles will be required to aim at different targets for different distances. Therefore, to include all these cases, a parametric study is conducted in this article to investigate the effects of different firing parameters–namely, firing impact amplitude, duration, and elevation angle–on the vehicle response, in terms of chassis maximum acceleration, vehicle slide and lift-off, tire blowout, pitch motion, range inaccuracy, and suspension travel. Consequently, the above mentioned concerns are assessed and the range of firing parameters for safe firing is determined. As a result, the feasibility of spade removal from lightweight, wheeled vehicles is investigated.

2. MATHEMATICAL MODELING

The most common lightweight, wheeled, military vehicle in many armies is probably the HMMWV. The HMMWV was designed primarily for personnel and light cargo transport behind front lines, not as a front line fighting vehicle. However, due to the urge of high mobility in the battle fields, HMMWVs are being equipped with different artillery guns and armament to be used in the front lines. A typical spade-less HMMWV with a mounted mortar is depicted in Fig. 2. The mortar in this picture is a low-recoil Super Rapid Advanced Mortar System (SRAMS).[15–17]

In this study, a six-degrees-of-freedom model of an integrated HMMWV-mortar system developed in the authors previous study is utilised.[13] Five degrees of freedom are the rear and front tire deflections, vehicle heave, pitch, and fore-aft motions. The sixth degree of freedom is the recoil mass motion of the mortar system. The mortar system is rigidly connected to the vehicle chassis and the elevation angle (α), once chosen, remains the same during firing. The mathematical model is schematically illustrated in Fig. 3. The soil elasticity is not considered in the current modelling hence, the simulations are valid if the firing is conducted on a relatively hard soil as compared to the vehicle tires. Although this model was originally developed for a HMMWV, it is generic and can be used for any other four-wheeled vehicle.

Since the pitch angle is usually small, the linearized dynamic equations of the system will be in the matrix form, as follows:

$$\mathbf{M}\ddot{\mathbf{z}} + \mathbf{C}\dot{\mathbf{z}} + \mathbf{K}\mathbf{z} = \mathbf{r_d}, \qquad (1)$$

where $\mathbf{z}$ is the displacement vector defined as

$$\mathbf{z} = \begin{bmatrix} y_G & \theta & x & y_{tr} & y_{tf} & x_r \end{bmatrix}^T. \qquad (2)$$

The displacement vector elements are vehicle heave, pitch, and fore-aft motions; rear and front tire deflections; and recoil displacement, respectively.

In Eq. (1), $\mathbf{M}$, $\mathbf{K}$, and $\mathbf{C}$ represent mass, stiffness, and damping matrices, respectively, and are defined in Eqs. (3) to (5)(see

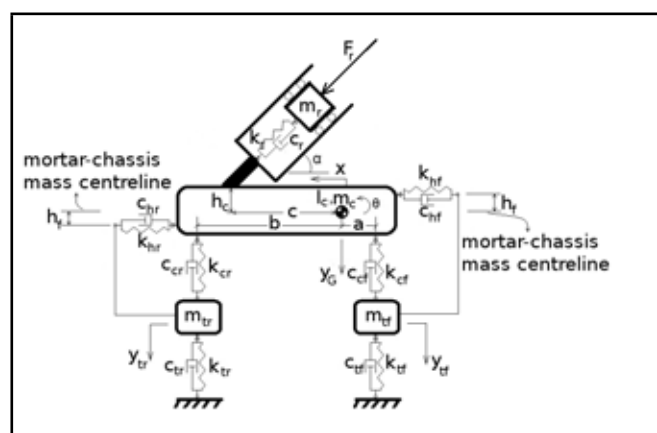**Figure 2.** A typical spade-less HMMWV with mounted mortar.

Figure 3. The mathematical model of an integrated spade-less HMMWV-mortar system

page 186).[13] In Eq. (1), $\mathbf{r_d}$ is the vector of the body forces and the firing impact, and can be written as

$$\mathbf{r_d} = \begin{bmatrix} m_c g & 0 & 0 & m_{tr}g & m_{tf}g & F_r + m_r g \sin \alpha \end{bmatrix}^T. \qquad (6)$$

All the parameters are described in the nomenclature. In order to decrease the order of differentiation, Eq. (1), which is essentially six, scalar, second-order, differential equations, is transformed into a state space, which will consist of twelve scalar, first-order, differential equations. The state space form will be as follows:

$$\dot{\mathbf{x}} = \mathbf{A}\mathbf{x} + \mathbf{R_d}, \qquad (7)$$

where the state vector, the state matrix, and the disturbance vector are defined, respectively, as

$$\mathbf{x}_{12 \times 1} = \begin{bmatrix} \mathbf{z}^T & \dot{\mathbf{z}}^T \end{bmatrix}^T, \qquad (8)$$

$$\mathbf{A}_{12 \times 12} = \begin{bmatrix} \mathbf{0}_{6 \times 6} & \mathbf{I}_{6 \times 6} \\ -\mathbf{M}^{-1}\mathbf{K} & -\mathbf{M}^{-1}\mathbf{C} \end{bmatrix}, \qquad (9)$$

and

$$\mathbf{R_d}_{12 \times 1} = \begin{bmatrix} \mathbf{0}_{6 \times 6} \\ \mathbf{M}^{-1} \end{bmatrix} \mathbf{r_d}. \qquad (10)$$

In all of the above mentioned equations, the mass, the mass moment of inertia, and the centre of gravity location of

$$\mathbf{M} = \begin{bmatrix} m_c & 0 & 0 & 0 & 0 & 0 \\ 0 & I_c & 0 & 0 & 0 & 0 \\ 0 & 0 & m_c & 0 & 0 & 0 \\ 0 & 0 & 0 & m_{tr} & 0 & 0 \\ 0 & 0 & 0 & 0 & m_{tf} & 0 \\ m_r \sin\alpha & m_r c \sin\alpha + m_r h_c \cos\alpha & m_r \cos\alpha & 0 & 0 & m_r \end{bmatrix}_{6\times6}, \tag{3}$$

$$\mathbf{K} = \begin{bmatrix} k_{cr}+k_{cf} & bk_{cr}-ak_{cf} & 0 & -k_{cr} & -k_{cf} & -k_r \sin\alpha \\ bk_{cr}-ak_{cf} & b^2 k_{cr}+a^2 k_{cf} & h_f k_{hf}-h_r k_{hr} & -bk_{cr} & ak_{cf} & -k_r(c\sin\alpha+h_c\cos\alpha) \\ 0 & 0 & k_{hf}+k_{hr} & 0 & 0 & -k_r \cos\alpha \\ -k_{cr} & -bk_{cr} & 0 & k_{cr}+k_{tr} & 0 & 0 \\ -k_{cf} & ak_{cf} & 0 & 0 & k_{cf}+k_{tf} & 0 \\ 0 & 0 & 0 & 0 & 0 & k_r \end{bmatrix}_{6\times6}, \tag{4}$$

$$\mathbf{C} = \begin{bmatrix} c_{cr}+c_{cf} & bc_{cr}-ac_{cf} & 0 & -c_{cr} & -c_{cf} & -c_r \sin\alpha \\ bc_{cr}-ac_{cf} & b^2 c_{cr}+a^2 c_{cf} & h_f c_{hf}-h_r c_{hr} & -bc_{cr} & ac_{cf} & -c_r(c\sin\alpha+h_c\cos\alpha) \\ 0 & 0 & c_{hf}+c_{hr} & 0 & 0 & -c_r \cos\alpha \\ -c_{cr} & -bc_{cr} & 0 & c_{cr}+c_{tr} & 0 & 0 \\ -c_{cf} & ac_{cf} & 0 & 0 & c_{cf}+c_{tf} & 0 \\ 0 & 0 & 0 & 0 & 0 & c_r \end{bmatrix}_{6\times6}, \tag{5}$$

the combined chassis-mortar system are used; however, there might be different mortars or vehicle chasses combined together. Therefore, for the model to be generic, parameters of the combined system are calculated using parameters of the vehicle chassis and the mortar. Details of the formulation to relate these parameters are discussed in the authors previous study.[13]

3. PARAMETRIC STUDIES

As mentioned earlier, in order to assess the different problems that might occur in a spade-less wheeled vehicle when firing, a comprehensive study on shock response of the vehicle-to-firing impact is needed. To this end, three different firing parameters–firing impact amplitude, duration, and elevation angle–are varied over a practical range, so as to account for different bomb charges and firing conditions. Vehicle response is then studied in terms of the chassis maximum acceleration, vehicle slide and lift-off, tire blowout, pitch motion, range inaccuracy, and suspension travel.

For the simulation results, the parameters of the HMMWV and the SRAMS are used for the vehicle and the mortar system. The geometric and physical properties of the vehicle chassis are used from those provided by Aardema[18] for a standard HMMWV without any shelter or mortar. Vehicle suspension and tire properties are adopted from the study conducted by Karakas et al.[19] and all are tabulated in Table 1. All the parameters in the table are introduced in the nomenclature.

Horizontal stiffness and damping have two components. The first part, which results from bushings and other constant sources, is assumed to be 7 % of the corresponding vertical stiffness and damping.[13] The other component of the horizontal stiffness and damping results from deviation of the vertical suspension from vertical position and it is assumed to be equal to 15% of their corresponding vertical values.[20] Furthermore, the static friction coefficient between the tires and the dry ground is assumed to be 0.7.[21]

The mortar system considered in this paper is a 120 mm

Table 1. The vehicle parameters for the full scale half HMMWV model

Parameter Symbol	Value	Parameter Symbol	Value
m_{ch}	1810 kg	c_{cf}	9000 N.s.m^{-1}
m_{tr}	181 kg	c_{tr}	4000 N.s.m^{-1}
m_{tf}	181 kg	c_{tf}	4000 N.s.m^{-1}
I_{ch}	2976 kg.m^2	L	3.3 m
k_{cr}	163300 N.m^{-1}	e	2 m
k_{cf}	163300 N.m^{-1}	h_{ch}	0.2 m
k_{tr}	463800 N.m^{-1}	h_{cf}	-0.2 m
k_{tf}	463800 N.m^{-1}	h_{cr}	0.2 m
c_{cr}	9000 N.s.m^{-1}		

Table 2. The mortar parameters for the full scale SRAMS model

Parameter Symbol	Value	Parameter Symbol	Value
m_r	400 kg	c_r	80345 N.m^{-1}
m_{mor}	800 kg	h	0.75 m
I_{mor}	2000 kg.m^2	f	1 m

smoothbore SRAMS. The properties of the mortar system are presented in Table 2. The recoil system of a gun is essentially a critically-damped system to absorb the recoil force.[22] Therefore, the recoil damping is set to a value so that the local recoil damping ratio is equal to unity. One should note that the properties given here for the mortar system are for a full-scale, full-mortar model, while the properties given for the vehicle are for a full-scale, half-car model. Therefore, once they are substituted into the system equations, one may either multiply the vehicle properties by two or the mortar properties by half. The geometric properties will not change for this matter.

Based on the experimental pressure data measured inside the SRAMS barrel the recoil firing force is modelled as a half-sine impact with an amplitude of F_r and a duration of T. Different forms of the sine function have been used by other researchers as well, to model the cannon firing and ballistic forces.[12] Unfortunately, the authors cannot reveal any of the experimental data due to confidentiality constraints. The firing impact is

then formulated as

$$F_r(t) = \begin{cases} F_r \sin(\pi t/T), & , 0 \leq t \leq T \\ 0 & , t > T \end{cases}. \quad (11)$$

The recoil impact amplitude (F_r) is varied from 50 kN to 400 kN,[23] and its duration (T) is varied over the range of 5 ms to 200 ms. Furthermore, the elevation angle (α) is varied from 10 to 80 degrees. Using the parameters given in this section and the mathematical modelling in section 2, the simulations are carried out in MATLAB and the results are presented in section 4.

4. RESULTS

The simulation results will show different responses of the vehicle in 3D diagrams or 2D contours, as a function of either the firing impact amplitude and the elevation angle, or the firing impact duration and the elevation angle. If the plotted response is a function of the firing impact amplitude and the elevation angle, the third remaining parameter, i.e., the firing duration, is set to 50 ms. And if the plotted response is a function of the firing impact duration and the elevation angle, the third remaining parameter, i.e., the firing impact amplitude, is set to 135700 N. These selected numerical values belong to the firing of a particular charge of a 120 mm SRAMS.

The safety and reliability of the electronics as well as human discomfort, are greatly dependent on the acceleration transmitted to them. According to the simulation results, the maximum vertical acceleration occurs at the rear of the vehicle, while the maximum horizontal acceleration is almost constant over the vehicle length. Therefore, the rear of the vehicle is the critical point where the electronics and the crew will experience the largest acceleration. Figure (4) shows the maximum total acceleration of the rear of the vehicle as a function of the firing impact amplitude and the elevation angle. Figure (5) shows the same response as a function of the firing impact duration and the elevation angle.

The total acceleration in these figures is a conservative one, since it is assumed that the maximum vertical and the maximum horizontal accelerations at the rear of the car occur at the same time. Hence, the total acceleration is calculated as the square root of the sum of the squares of the maximum vertical and horizontal accelerations. This is a valid assumption, since they actually occur almost at the same time. According to the figures, as any of the three parameters increases, the maximum total acceleration also increases. As shown in Fig. 5, higher impact durations yield a sudden jump in the slope of the acceleration increase. This is probably because of the proximity of the impact fundamental frequency to that of the chassis heave or pitch motion.

According to the results, the maximum total acceleration falls below 10 g for a large range of the firing variables. This is well below the average human acceleration tolerence. Although its being subjective makes the measurment of this tolerence an arduous task, there are few articles reporting an average acceleration tolerance based on different criteria. An experiment conducted by Lombard and his colleagues is presented by Hundley et. al.,[6] who reports an average tolerance level of 22.6 g based on local pain, bruising, and neck
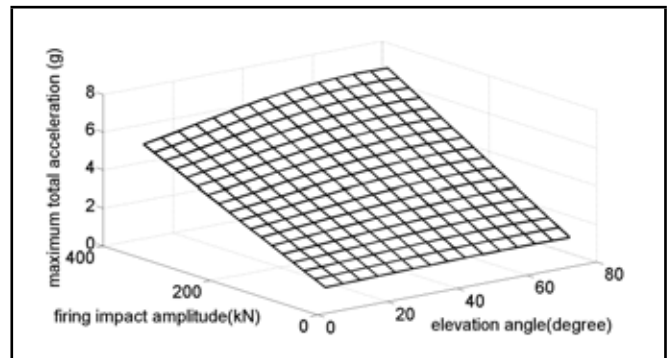
Figure 4. The maximum total acceleration at the rear of the vehicle as a function of the firing impact amplitude and the elevation angle
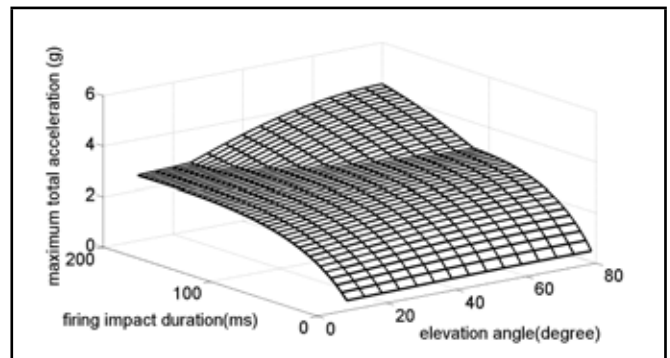
Figure 5. The maximum total acceleration at the rear of the vehicle as a function of the firing impact duration and the elevation angle

pain. The acceleration tolerence for electronics is usually much larger.

The other issue is to see if a recoil system designed and optimised for a particular bomb or charge properly reduces the recoil force for other bombs and charges or not, as well as to see if it works properly for all possible elevation angles. Figures 6 and 7 show the maximum transmitted recoil force through the recoil system as a function of the three parameters. This force is normalised by the amplitude of the firing impact; hence, a normalised force of zero indicates zero force transmission, and a normalised force of one indicates complete transmission of the firing impact through the recoil system to the vehicle chassis. According to the figures, as the firing impact duration or elevation angle increases, the transmitted recoil force increases, meaning that the recoil system functionality degrades. However, when the firing impact amplitude increases, the recoil system efficacy improves.

Another concern when the spades are eliminated is that the vehicle might slide on the ground for high bomb charges or small elevation angles. To check this issue, the horizontal force exerted to the tires by the chassis is compared to the maximum static friction force that can be applied from the ground on the tires.If the former force is larger than the latter the vehicle will slide. The maximum friction force on the vehicle is calculated by multiplying the friction coefficient and the normal force between the ground and the tires.

Figures 8 and 9 show the vehicle slide contours for a dry contact between the tires and the ground, in terms of firing impact amplitude, duration and elevation angle. The contours are divided into two regions, the slide region and the no-slide region, which are separated by the boundary line named dry.
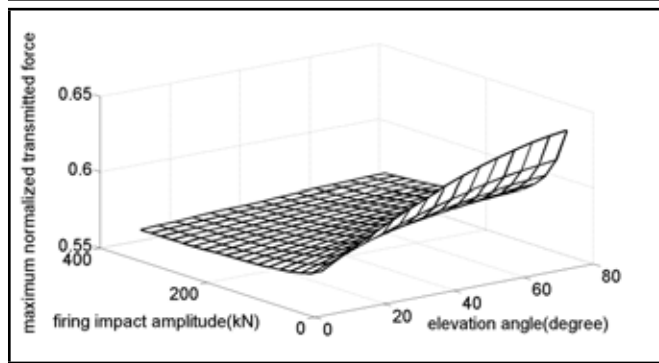
Figure 6. The maximum normalised transmitted recoil force as a function of the firing impact amplitude and the elevation angle
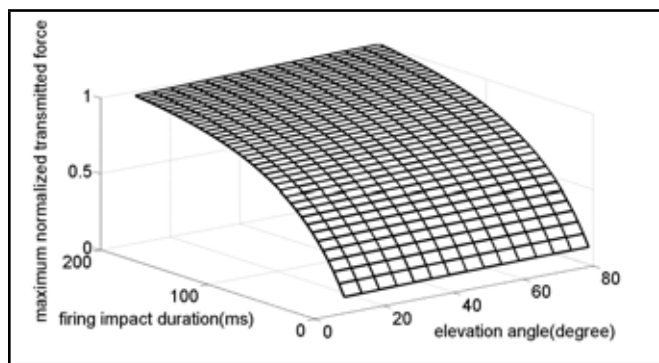

Figure 7. The maximum normalised transmitted recoil force as a function of the firing impact duration and the elevation angle
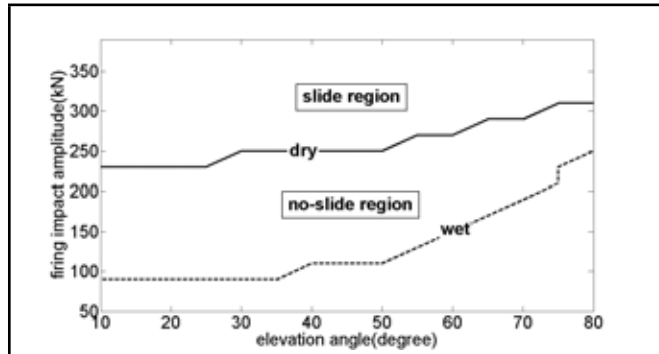

Figure 8. The vehicle slide contour in terms of the firing impact amplitude and the elevation angle; the solid line indicates the dry tire-ground condition, and the dotted line represents the wet tire-ground condition.

Figure 9. The vehicle slide contour in terms of the firing impact duration and the elevation angle; the solid line indicates the dry tire-groind condition, and the dotted line represents the wet tire-ground condition.

Figure 10. The vehicle lift-off contour in terms of the firing impact amplitude and elevation angle.

Figure 11. The vehicle lift-off contour in terms of the firing impact duration and the elevation angle.

If the contact between the tires and the ground is wet or the road has iced over, the boundary line falls below the dry line, which decrease the no-slide region. The wet boundary line is labelled as wet in the vehicle contour diagrams. The decrease of the no-slide region in wet or frozen conditions is due to the drop in the static friction coefficient that is considered to be 0.25 for the simulations in this paper. The friction coefficient is assumed as 0.25 to represent an arbitrary wet or icy road while investigating the surface and friction condition on the sliding vehicle. According to the figures, as either the firing impact amplitude or the duration increases, or the elevation angle decreases, the vehicle is more likely to slide in both dry and wet conditions.

As the bomb charge or elevation angle increases, there is a tendency for the vehicle to lift off of the ground after firing. In
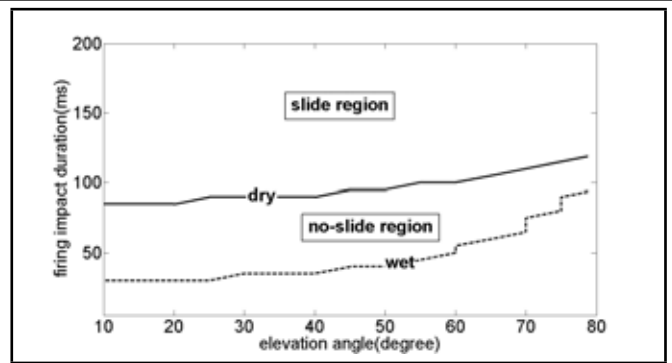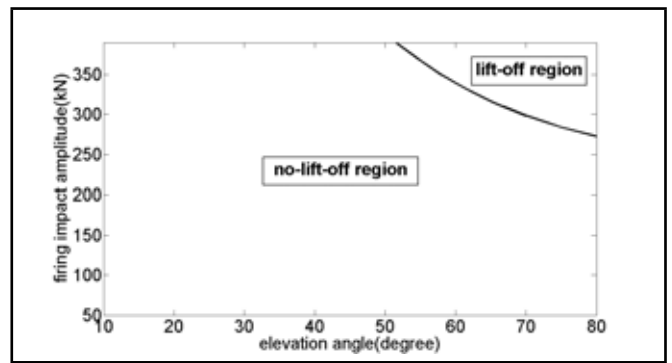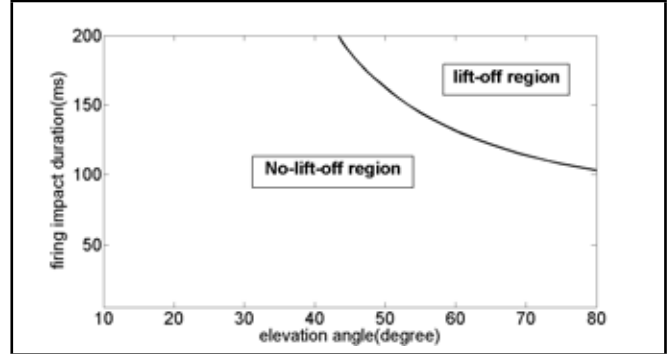
the simulations, when the tire force becomes zero, it indicates that the tire starts to lift off of the ground (a positive value of tire force represents a compressive force). For this case study, the rear tires always have a smaller minimum force than the front tires do, for any firing impact amplitude, duration, or elevation angle. Therefore, the rear tires determine if the vehicle lift-off occurs or not. Figures 10 and 11 show the vehicle lift-off contours in terms of the firing impact amplitude, duration, and elevation angle. The contours are divided into two regions; these are the lift-off region and the no-lift-off region. According to the figures, as the firing impact amplitude or duration, or the elevation angle increases the tires are more likely to lift off.

A serious concern for lightweight, wheeled vehicles is tire blowout when the spades are eliminated. The transmission of excessive firing impact force to the chassis and the tires, at high
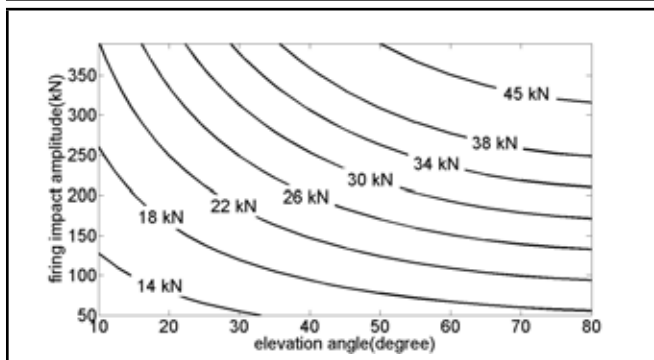
Figure 12. The force contour for rear tires in terms of the firing impact amplitude and elevation angle.
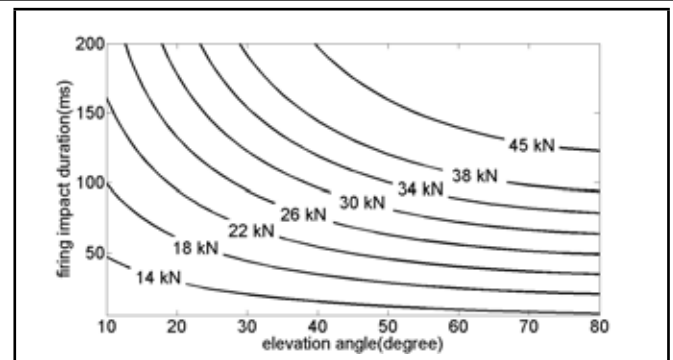
Figure 13. The force contour for rear tires in terms of the firing impact duration and the elevation angle.

bomb charges, may blow out the tires due to excessive tire load. Therefore, tire load analysis is essential for prediction and prevention of tire blowout. For the vehicle-mortar configuration considered in this paper, the rear tires experience larger loads than the front tires do over the practical ranges for the three parameters studied in this research. Consequently, the rear tires will determine if the tires will blow out under the firing impact force. Figures 12 and 13 show force contours for the rear tires in terms of firing impact amplitude, duration, and elevation angle. According to the figures, as any of these parameters increase, the tire load increases too. These figures can be used to see if a particular tire with a known maximum load capacity will blow out under a given firing impact load, duration, and elevation angle.

The tires commonly used in HMMWVs can resist up to 18 kN. This low maximum capacity restricts firing high bomb charges at large elevation angles. However, by a thorough search, these authors found other rugged tires for HMMWVs that are capable of handling higher tire forces. Baja T/A off-road tires, made by the BFGoodrich company and having an NSN number of 2610-01-563-8328, are examples of E-range, high-capacity tires capable of handling more than a 22 kN load when stationary. Furthermore, there is a new generation of airless tires called Tweel, first commercialised by Michelin. These tires have a higher load capacity than their pneumatic counterparts, due to the airless characteristics. To design even higher capacity tires for military applications, particularly for HMMWVs, Resilient Technologies and Wisconsin-Madison's Polymer Engineering Center are currently developing a patent-pending, non-pneumatic tire that can even survive an IED attack, and still make a 50 mph getaway.[24] This tire is basically a round honeycomb wrapped with a thick, black tread. The airless tire is currently being tested on a Wausau-based National Guard HMMWV. However, airless tires have their own drawbacks, and the decision regarding whether to use them or not requires a thorough consideration of all their advantages and disadvantages.

Another method to mitigate the risk of the tire blowout is the pressure change of the tires. Nowadays, the technology on some of the cars allows the driver to decrease or increase the tire pressure with a remote. Since the load capacity of the tire significantly depends on its pressure, if this technology is installed in the vehicle, then the pressure could be changed accordingly when firing, which would increase the tires load capacity and, prevent tire blowout.

Another concern for lightweight vehicles firing high calibre guns without spades is a large pitch angle of the chassis, which significantly affects crew comfort and firing accuracy. According to simulation results (not shown in this article), as the firing impact amplitude or duration, or elevation angle increases, the maximum pitch angle increases as well. Consequently, the chassis pitch angle affects the firing accuracy. If the momentum velocity of the bomb, leaving the barrel, is designated by V_0, the firing range will be

$$R = (V_0^2 \sin 2\alpha)/g, \qquad (12)$$

where R is the range, α is the elevation angle, and g is the gravitational acceleration. By assuming a half-sine firing impact as mentioned before, the impulse imparted to the bomb will be

$$\int_0^T F_{firing} dt = \int_0^T F_r \sin(\pi t/T) dt = 2F_r T/\pi, \qquad (13)$$

where F_{firing} and F_r are firing and recoil forces, respectively. Therefore, if the bomb mass is designated by m, the bomb velocity leaving the barrel, i.e., V_0 will be

$$V_0 = 2F_r T/m\pi. \qquad (14)$$

Now, one can evaluate the change in the range in terms of a change in the elevation angle by differentiating Eq. (12) with respect to α. Differentiating Eq. (12) and substituting V_0 from Eq. (14) yields,

$$dR = \frac{2}{g}(2F_r T/m\pi)^2 \cos(2\alpha) d\alpha. \qquad (15)$$

Making use of Eq. (15) and assuming that the bomb weighs 15 kg, the firing inaccuracy due to the pitch motion is plotted in Figs. 14 and 15. According to the figures, as the elevation angle deviates from 45 degrees, the inaccuracy in the firing range increases. However, this increase in inaccuracy for complementary elevation angles (having equal deviation from 45 degrees) is not equal; the smaller angle will have a smaller inaccuracy in the range. Therefore, since firing at complementary elevation angles ideally results in the same range, it is recommended to fire at the smaller elevation angle due to its smaller inaccuracy. Furthermore, as the impact amplitude or duration increases, the inaccuracy in the firing range also increases. This increase in inaccuracy becomes as large as a few kilometres for large impact amplitudes or durations.
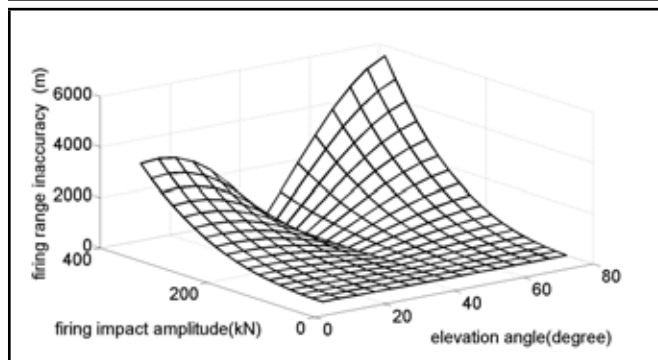
Figure 14. The firing range inaccuracy as a function of the firing impact amplitude and elevation angle.
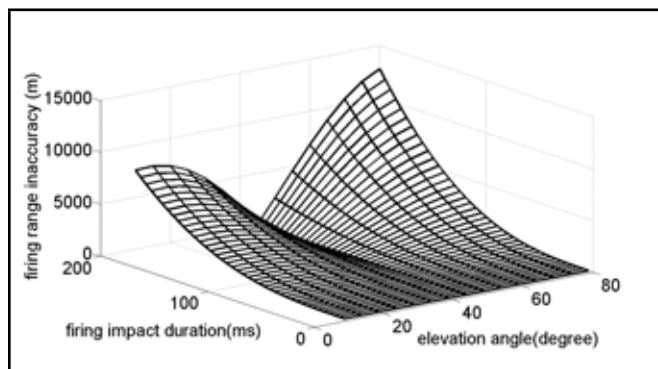
Figure 15. The firing range inaccuracy as a function of the firing impact duration and elevation angle.

Therefore, the use of spades on lightweight vehicles is recommended for higher accuracy when very high calibre guns and large bomb charges are being used.

And, finally, the suspension travel of the vehicle should also be checked so as to not exceed the maximum allowed value; otherwise, the dampers will bottom out and eventually cease to function. For the vehicle-mortar configuration in the simulation–with a given firing impact amplitude, duration and elevation angle–the rear suspension travel is always larger than that of the front suspension. According to simulation results (not shown here), as the firing impact amplitude, duration, or the elevation angle increases, the maximum suspension travel increases as well. However, the maximum suspension travel reaches 22 cm in the worst case, which is still acceptable and will not normally result in suspension damage or bottoming out of the dampers.

The effects of firing impact on a spade-less, lightweight, wheeled vehicle was analysed in this section and the vehicle response was assessed in terms of chassis maximum acceleration, vehicle slide and lift-off, tire blowout, pitch angle, range inaccuracy, and suspension travel.

5. CONCLUSION

The research was conducted to investigate the effects of firing impact on spade-less, lightweight, wheeled, military vehicles and determine whether spade removal was feasible. To this end, a generic six-degrees-of-freedom mathematical model of a vehicle-mortar system was used. The effects of three main firing parameters–firing impact amplitude, duration, and elevation angle–were investigated on the vehicle re-

sponse. These three parameters enable the analysis to cater to different bombs, bomb charges, and firing conditions. The vehicle response was assessed in terms of vehicle maximum acceleration, slide, lift-off, tire blowout, pitch angle, range inaccuracy, and suspension travel.

Simulation results show that maximum acceleration occurs at the rear of the vehicle. Although the maximum acceleration is below 10 g and might not affect a single fire, multiple firing might bring about, fatigue electronic damage, or crew discomfort such as headaches, transitory head pain, and neck strain. To prevent these problems, it is recommended that the electronics are not mounted at the rear of the vehicle and that the crew should be absent from the vehicle or sitting in the front seats while the cannon is being fired.

It was also shown that the functionality of the recoil system will be degraded as the impact duration or elevation angle increases. The efficacy of the recoil system is more sensitive to the former parameter, i.e., the impact duration. The simulation results also show that the vehicle will not slide unless firing horizontal, high calibre guns at very large charges. This slide issue becomes problematic if the ground is wet and slippery. Similarly, the vehicle would not lift of the ground unless it fired high bomb charges at large elevation angles.

Furthermore, according to the results, the tires are likely to blow out when the firing impact amplitude or duration becomes very large. To prevent this from happening, the use of more rugged tires is recommended. As the firing impact amplitude or duration increases, the pitch and the firing inaccuracy increase as well. However, although the pitch angle increases as the elevation angle increases, the firing inaccuracy increases as the elevation angle deviates from 45 degrees. Nevertheless, the firing inaccuracy for the complementary elevation angles is not the same, as it is smaller for the smaller elevation angle; therefore, it is recommended that the smaller elevation angle be chosen to fire between the two complementary angles, which ideally result in equal ranges. And, finally, the simulation results show that there would be no excessive suspension travel, even at high bomb charges or elevation angles.

In summary, all of the above mentioned problems about a spade-less, lightweight, wheeled vehicle can be avoided if appropriate precautions are taken (except for firing inaccuracy, if high calibre guns at high bomb charges are used). Firing at distant targets with high calibre guns and high bomb charges from a spade-less, lightweight vehicle can result in up to a few kilometres of inaccuracy in range. Thus, for this purpose, spades are needed for a lightweight, military vehicle with passive suspensions. However, for a broad range of firing amplitude, duration, and elevation angle, it is feasible to remove the spades, which therefore increases the vehicle mobility and avoids the challenging and sometimes impossible task of an optimum and efficient spade design.

REFERENCES

[1] Tedesche, M., Durocher, R., and Gully, M. Discussion of fire out of battery test results, Technical Report P954210, (2001).

[2] Fabey, M. GCV may decide fate of army tracked vehicles, *Aviation Week*,(2010).

[3] Balbo, P. Weapon system able to equip a light vehicle and process to implement such a weapon system, United States Patent, (2005).

[4] Fraud, M. and Donnard, R. Mobile mortar firing unit, United States Patent, (1988).

[5] Kathe, E. L. Recoil considerations for railguns, *10th Electromagnetic Launch Technology (EML) Symposium*, USA, (2001).

[6] Hundley, T. A. Measurement of gunner head acceleration during firing of high impulse guns on lightweight armored vehicles and the assessment of gunner tolerance to such impact, Technical Report A516191, (1987).

[7] Zywiol, H. and LaFiandra, M. E. Mounted combat system crew shock loading: head and neck injury potential evaluation, Technical Report A357964, (2007).

[8] Murdza, C. Weapon recoil effects on canted lightweight vehicles, Technical Report A715582, (1994).

[9] Brosseau, T. L., Kregel, M. D., Haug, B. T., and McLaughlin, J. T. The inertial reticle technology (IRT) applied to a 50-cal. M2 heavy-barrel machine gun firing from a high-mobility multipurpose wheeled vehicle (HMMWV), Technical Report A510773, (2000).

[10] Shengtao, Z. Study and experiment of the gun-to-vehicle ratio, *Vehicle & Power Technology*,(1990).

[11] Balla, J. Combat vehicle vibrations during fire in burst, *International Conference on Mathematical Models for Engineering Science*, Puerto de la Cruz, Tenerife, Spain, (2010).

[12] Balla, J. Dynamics of mounted automatic cannon on track vehicle, *International Journal of Mathematical Models and Methods in Applied Sciences*, **5**(3), 423–432, (2011).

[13] Hosseinloo, A. H., Vahdati, N., and Yap, F. F. Performance of spade-less wheeled military vehicles with passive and semi-active suspensions during mortar firing, *Vehicle System Dynamics*, **50** (10), 1515–1537, (2012).

[14] Hosseinloo, A. H., Vahdati, N., and Yap, F. F. Elimination of spades in wheeled military vehicles using MR-fluid dampers, *Active and Passive Smart Structures and Integrated Systems; SPIE*, San Diego, CA, United states (2011).

[15] Foss, C. F. Mortar system detailed as trials progress, *Jane's Defence Weekly*, (2004).

[16] Foss, C. F. Singapore technologies kinetics mounts mortar system on HMMWV, *Jane's Defence Weekly*, (2005).

[17] Foss, C. F. 120 mm mortar SRAMS allows greater mobility, *Jane's Defence Weekly*,335–338, (2006).

[18] Aardema, J. Failure analysis of the lower rear ball joint on the high-mobility multipurpose wheeled vehicle (HMMWV), Technical Report A498102, (1988).

[19] Karakas, E. S., Gordaninejad, F., Evrensel, C. A., Yeo, M.-S., Liu, Y., and Sahin, H. Control of a quarter HMMWV suspension system using a magneto-rheological fluid damper, *Smart Structures and Materials*, Damping and Isolation, San Diego, CA, United States, (2004).

[20] Berghuvud, A. and Stensson, A. Consequences of nonlinear characteristics of a secondary suspension in a three-piece freight car bogie, *Vehicle System Dynamics*, **36** (1), 37–55, (2001).

[21] Bedford, A. and Fowler, W. *Engineering mechanics: statics*, Prentice Hall, (2008).

[22] Bhatnagar, R. M. Recoil motion theorem, Proceedings of the Institution of Mechanical Engineers, Part K: *Journal of Multi-body Dynamics*, **219** (2), 173–176, (2005).

[23] Borkowski, W., Rybak, P., Hryciw, Z., Wysocki, J., and Michaowski, B. Combat vehicle dynamic load tests in the aspect of the operation safety, *Journal of Konbin*, 13 (1), 65–78, (2010).

[24] Answering the Call for Extreme Tires, Retrieved from www.physicscentral.com/explore/action/extremetires1.cfm, (Accessed September 20, 2012).

Rotating Group Design for Vane Pump Flow Ripple Reduction

Leonardo Zanetti-Rocha and Samir N.Y. Gerges

Department of Mechanical Engineering, Federal University of Santa Catarina, University Campus, Trindade, 88040-900, Florianpolis-SC, Brazil

D. Nigel Johnston

Department of Mechanical Engineering, University of Bath, Bath, BA2 7AY, UK

Jorge P. Arenas

Institute of Acoustics, University Austral of Chile, PO Box 567, Valdivia, Chile

It is well known that the hydraulic pump is the main source of noise in hydraulic power steering systems. This noise is produced by the pulsating flow transmitted through the fluid due to the cyclic pumping mechanism. This flow ripple and pressure ripple spread through the hydraulic circuit, interacting in a complex way with other parts of the vehicle. This process generates annoying audible noise inside the vehicle. This work addresses a new approach to flow ripple reduction by tuning the pump rotating group. The method consists of making the outlet flow as steady as possible by modifying the rotating group geometry. A MATLAB/Simulink-based pump model has been created according to the new geometrical characteristics and their numerical results, compared to the regular pump ones. In addition, a flow ripple experiment was conducted using the secondary source method (SSM to validate the numerically-predicted results of the regular pump. The results of the new design show significant amplitude reduction of the flow ripple amplitudes at different operating conditions. In particular, the flow ripple reduction at the first harmonic is almost 20 dB when the pump runs in a parking manoeuvres operating condition (1000 rpm at 50 bar of backpressure).

1. INTRODUCTION

Noise produced by the hydraulic power steering pump when operating a car can, in some situations, be perceived inside the vehicle as an annoying sound. The flow variations (flow ripple) generated by the pump through its natural operating process are transmitted along the power steering hydraulic circuit, interacting with the impedance of the hoses and tubes. This process generates structural vibration and, consequently, sound emission around the circuit.[1]

In some vehicles, the hydraulic circuit is tuned in order to avoid hearing noise inside the cabin. Flexible hoses, sometimes with tuning cables, are usually used to increase circuit compliance in order to remove unwanted resonance frequencies or reduce the flow ripple amplitude. In fact, there are several techniques and devices—such as silencers, side branches, accumulators, etc.—that can be used to reduce fluid-borne noise along the propagation circuit.[2,3]

However, if a pump can be manufactured with a lower noise profile, this may create a solution that is independent of the hydraulic circuit and does not require costly and time-consuming tuning of the system to achieve the required noise reduction.

The present work is aimed at vane pumps and proposes a new rotating group design, intended to reduce the flow ripple amplitude. Because this new design is not dependent on the number of vanes, an eight vane rotating group was developed to combine cost reduction with flow ripple reduction.

In order to achieve those results, a MATLAB/Simulink-based numerical model was created from a regular pump design and validated through the experimental secondary source mMethod (SSM), which has been developed at the University of Bath.[4,5] The SSM has been used as the basis for an international standard to measure pump pressure ripple characteristics.[6] The simulated results of the new design are compared here with the regular pump ones. A comparison is then made in terms of the flow ripple amplitudes in the frequency domain.

2. REGULAR PUMP CHARACTERISTICS

The regular automotive pump has two discharge ports located diametrically opposite to each other, i.e., they are spaced by an angle of $180°$ regarding the centre of the thrust plate as the centre of the reference circumference. This type of positive-displacement pump is called a *balanced pump* because these two opposite ports balance the forces acting against the rotor, and all the walls of the chamber as well, reducing the shaft pump oscillations and overall vibrations. Figure 1 shows the rotating group components and its assembly scheme.

The pump uses the engine torque applied to its shaft to pump oil from the inlet port to the outlet port. Figure 2 shows a scheme of the pumping process inside the pump. The system back pressure varies according to the outlet hydraulic circuit constraint, increasing the pressure as the constraint increases.
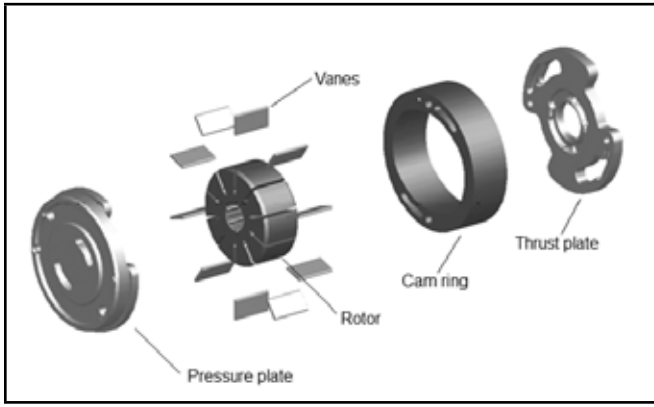
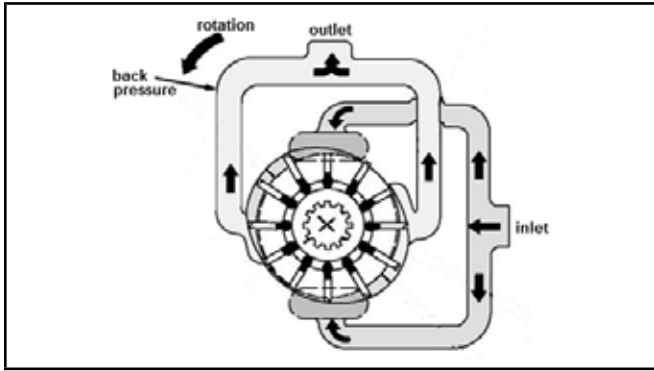**Figure 1.** The rotating group components.

Figure 2. Schematics of the rotating group operation.

3. PUMP MODEL

The numerical model of the pump is based on the general continuity equation, choosing the chamber, between a leading vane and its trailing vane, as the control volume. Similar models have been developed by other authors.[7–9]

All the dimensions (geometric data) were loaded into the model from the drawings of a regular ten-vane automotive hydraulic pump. The rate of change of pressure with respect to time is given by

$$\frac{dp}{dt} = -\frac{\beta_e}{V}\frac{dV}{dt} - Q_{IN} - Q_{OUT} - Q_{LEAK}; \quad (1)$$

where Q_{IN} is the flow in the inlet port, Q_{OUT} is the flow in the discharge port, β_e is the effective bulk modulus, V is the chamber volume, and Q_{LEAK} is the flow resulting from the leakage path inside the pump.

The flows through the inlet and outlet ports are calculated using the orifice equation, which relates the pressure difference between the downstream and upstream sides of a restriction. This is given by

$$Q = C_d A \sqrt{\frac{2\Delta p}{\rho}}; \quad (2)$$

where C_d is the orifice flow coefficient, A is the orifice area, ρ is the fluid density, and Δp is the pressure difference between the upstream and downstream sides. The flow leakages are calculated using the equation for laminar leakage flow between two planes, one of which is moving relative to the other, i.e.,

$$Q_{LEAK} = \frac{LH^3(p - p_a)}{12\mu t_h} \pm \frac{vLh}{2}; \quad (3)$$

where h is the clearance, L is the width of the gap, t_h is the length of the gap, μ is the fluid viscosity and v is the velocity. The first term on the right hand side of Eq. (3) describes the flow through the areas when both are fixed. The second term adds the effect of relative movement of the plates (Couette Flow).

Analysing the pump operation and the way that the internal parts are assembled, several leakage paths can be identified where leakage flows can be calculated. Therefore, Eq. (3) is used to calculate the following leakage paths into the pump rotating group.

1. Vane tip leakage:

$$Q_{vtl} = \frac{L_v h_1^3(p - p_a)}{12\mu t} \pm \frac{\omega r L_v h_1}{2}. \quad (4)$$

2. Vane end leakage:

$$Q_{vll} = \frac{(r_c - r_r)h_2^3(p - p_a)}{12\mu t_v} \pm \frac{\omega(r_c + r_r)(r_c - r_r)h_2}{4}. \quad (5)$$

3. Vane slot leakage:

$$Q_{vsl} = \frac{L_v h_3^3(p - p_{out})}{12\mu \left[h_v - (r_c - r_r)\right]}. \quad (6)$$

In Eqs. (4)–(6), L_v is the vane length, h_1 is the vane tip clearance, h_2 is the vane end clearance, h_3 is the vane slot clearance, ω is the rotational speed of the vanes, p is the fluid chamber pressure, p_a is the adjacent (leading or trailing) fluid chamber pressure, h_v is the vane height, r_c is the radius of the cam ring from the centre of the rotor, and r_r is the rotor radius.

Figure 3 shows a scheme of a fluid chamber showing the three leakage paths corresponding to Eqs. (4)–(6). The scheme also shows a leakage path across the end faces of the rotor, q_{rli}, which is not included in the present model since its value is negligible.

The model also needs to include the 'under-vane' flow to the chambers at the inner radial faces of the vanes, caused by the vane movement which is expressed by

$$Q_{uv_i} = v_i L_v t_v; \quad (7)$$

where $v_i = dr_i/dt$ is the radial speed of the vane. These chambers connect to the delivery port, and the pressure helps the vane with its radial movement to maintain contact against the ring wall, along with centrifugal forces. The sum of the under-vane flows results in the total pump under-vane flow, given by

$$Q_{uv} = \sum_{i=1}^{N_v} Q_{uv_i}; \quad (8)$$

where N_v is the number of pump vanes (notice that in the standard pump, $N_v = 10$).

Some of the values used in the numerical simulation are presented in Table 1. The fluid bulk modulus is reduced to allow for the effect of air bubbles and compliance of the rotor and vanes. The vane end clearance was estimated from the vane
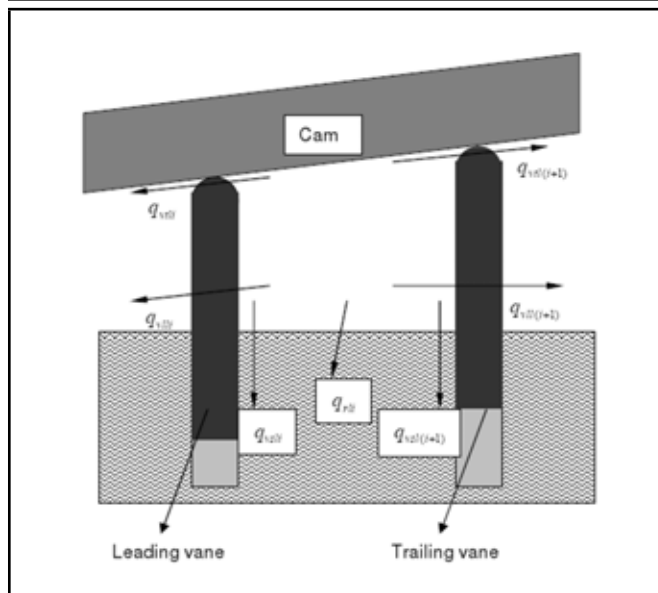
Figure 3. The leakage flows in and out of the fluid chamber.[8]

Table 1. Values used in the numerical simulation.

Fluid viscosity	8.3 cP
Fluid density	870 kg/m^3
Effective bulk modulus	4×10^8 Pa
Flow coefficient for ports	0.6
Vane tip clearance	0.01 mm
Vane end clearance	0.019 mm
Vane slot clearance	0.01 mm
Rotor radius	20.7 mm
Rotor width	16 mm

and rotor dimensions. The vane tip and vane slot clearances are simple estimates, and in practice these clearances would be expected to vary as the vanes move through their cycle.

Figure 4 shows the regular pump numerical simulation, running at 1000 rpm at 50 bar.

4. SECONDARY SOURCE METHOD

The secondary source method (SSM), developed at the University of Bath,[4,5,10] was used in this work for measuring both the pump flow ripple and the impedance. The SSM was first adopted as the British Standard for measuring pump fluid-borne noise,[11] and was later used as the basis for an ISO standard in the measurement of pump pressure ripple characteristics.[6]

The SSM is based on the measurements of the harmonics of the pressure ripple at a series of points along the length of a rigid pipe connected either to the delivery or suction port of the test pump. The pressure ripple that occurs at two or three positions is analyszed to determine the pressure ripple.

From the Norton model, shown in Fig. 5, it is possible to find an equation to establish the flow ripple at the pump discharge port:

$$Q_0 = Q_s - \frac{P_0}{Z_s};$$
(9)

where Q_s is the internal source flow, Q_0 is the flow ripple at the pump discharge port, P_0 is the pressure ripple at the discharge

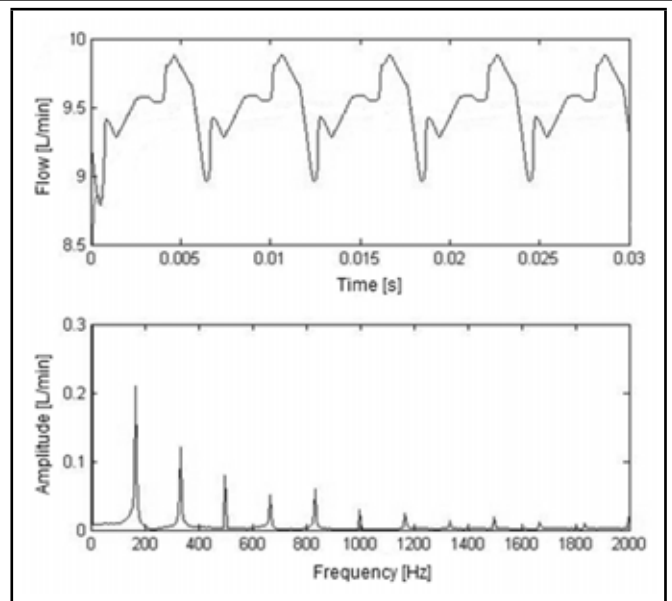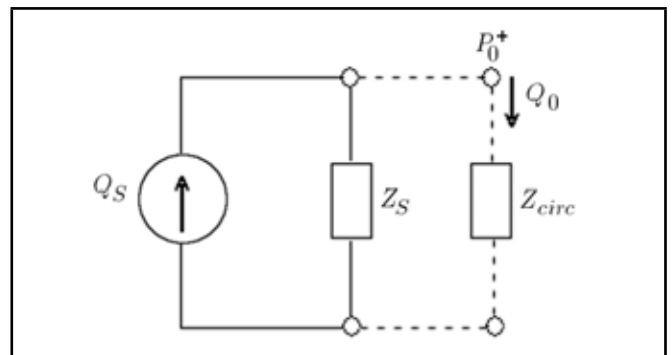**Figure 4.** The regular pump outlet flow ripples (1000 rpm at 50bar).

Figure 5. The Norton model of a pump.

port, and Z_s is the source impedance.

In order to calculate the source impedance, a secondary source of pressure ripple is placed downstream of the pump, as shown in Fig. 6. In this condition, the secondary source is operated at a different speed than the test pump and the harmonic components of this secondary source are measured. It can be shown that if the second pump flow ripple frequencies do not coincide with the pump under the test circumstances, the harmonic frequencies and the spectral leakages are negligible, while Q_s can be assumed to be zero. Therefore, the calculation of the source impedance Z_s can be separated from the calculation of the source flow ripple Q_s. Thus, Eq. (9) is simplified and the source impedance can be determined as

$$Z_s = -\frac{P_0}{Q_0}.$$
(10)

Measurements of the pressure ripple are then taken with the secondary source not operational, from which Q_s can be easily calculated through the Norton model, given that the values of Z_s, P_0 and Q_0 are known.

Even though the basic principles of SSM are presented, it is not the aim of this paper to discuss the method in detail. More information and the detailed evaluation of the SSM can be found in the literature.[4,5,10]
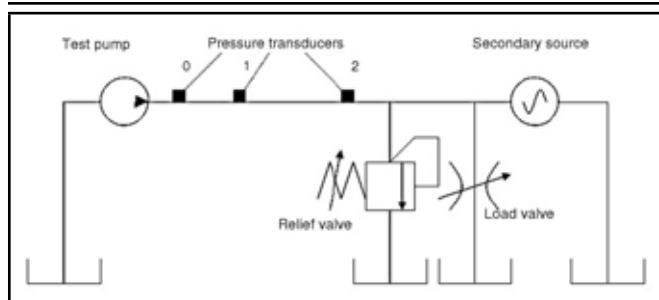
Figure 6. The hydraulic circuit for secondary source method.[12]

The simulated results were compared with the experimental ones measured through the SSM, and some results are shown in Fig. 7. The simulated results show reasonably good agreement with those obtained by the SSM when the pump is run at low speed—i.e., 1000 rpm in Fig. 7a and 7b. However, for more extreme conditions, e.g, 2000 rpm and 75 bar in Fig. 7c, the shape of the flow does not match accurately with the simulated ones.

To improve the experimental analysis, a frequency domain analysis was carried out. Figures 8a–8c show the simulated and measured results in the frequency domain of the outlet flow ripple for the same operating conditions considered in Figs. 7a–7c. It can be seen that when the pump is run at low speed, there is a good agreement between the measured and simulated results of amplitude of the first harmonics, where differences between the results vary from none to a maximum of 7 dB. On the other hand, Fig. 8 also shows a low correlation between measured and simulated amplitudes when the pump is run at high speeds, mainly at high frequencies, which explains the differences observed in Fig. 7c.

Differences between experimental and simulated results may be attributed to inaccuracies in the SSM, as well as simplifications and assumptions made in the simulation model. Uncertainties in the nature of the delivery passageway and the integral flow control valve, which are not included in the model, may explain some of the differences. Nonetheless, the similarity in the amplitude and the trends of the results in the time-domain analysis, and the similarity in the amplitudes of the first harmonics in the frequency-domain analysis, indicate that the results obtained from the simulation model are reasonable and may be used to investigate the effect of making changes in the design of the rotor, cam and ports.

5. REGULAR PUMP FLOW RIPPLE ANALYSIS

As seen previously, the pump outlet flow ripple is the result of several hydraulic phenomena that occur inside the rotating group during the operation. To understand how the outlet flow ripple is formed, it is important to analyse the influence of each one of these phenomena separately. Once this analysis is done, it would be possible to act over each phenomenon in order to reduce the flow ripple amplitude.

5.1. Timing Analysis

Figure 9 shows the simulated outlet flow without the influence of the internal leakage flows and the under-vane flows,
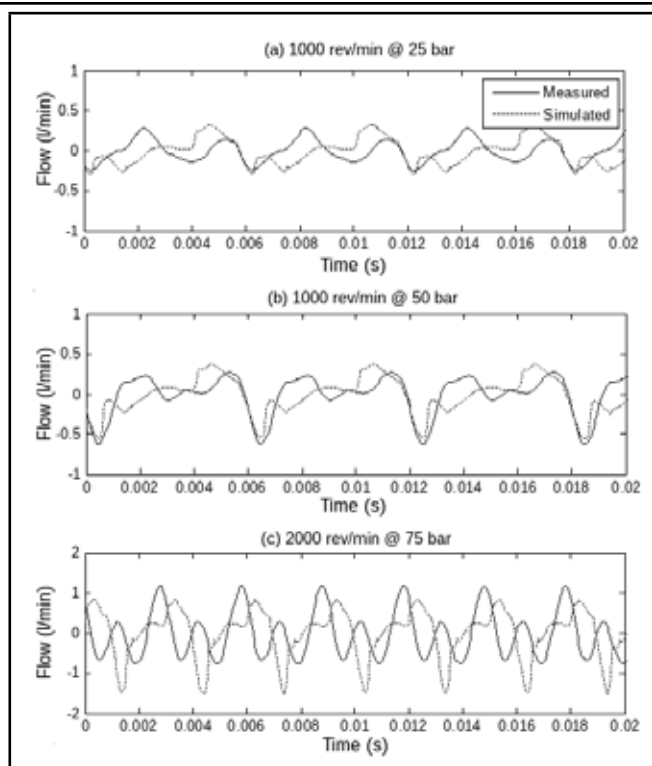

Figure 7. Results of the measured and simulated outlet flow ripple in the time-domain.

run at 1000 rpm and 50 bar. From these results it can be observed that:

1. Excepting the effects of the dynamic flow characteristics, represented in the plot by "spills" along the curve (pointed), the outlet flow (without leakage and vanes flows) is not uniform. In fact, the final signal shape is quite similar to a saw-tooth wave, as can be seen in Fig. 10.

2. There is a $36°$ lag between the start of two consecutive fluid chamber flows. Also, $88°$ is the total angular length that the fluid chamber passes over to the discharge port, i.e., the discharge port is opened to a fluid chamber during a rotation of $88°$ degrees.

In addition, it can be shown that, independent of the intersection point between two consecutive fluid chamber flows, the outlet flow will always exhibit a saw-tooth shape with different amplitudes. In Fig. 11, we can observe some interesting intersection points.

5.2. Under-vane Flow Analysis

As described by Eq. (7), if the compressibility effect is ignored, the under-vane flow will be proportional to the vane radial velocity. The total pump flow ripple caused by under-vane flows will be the sum of all under-vane flow contributions along the rotor revolution, as described by Eq. (8). Figure 12 shows each under-vane flow contribution, while Fig. 13 shows the pump under-vane flow, that is to say, the sum of them.

From the figures it is possible to notice the following:

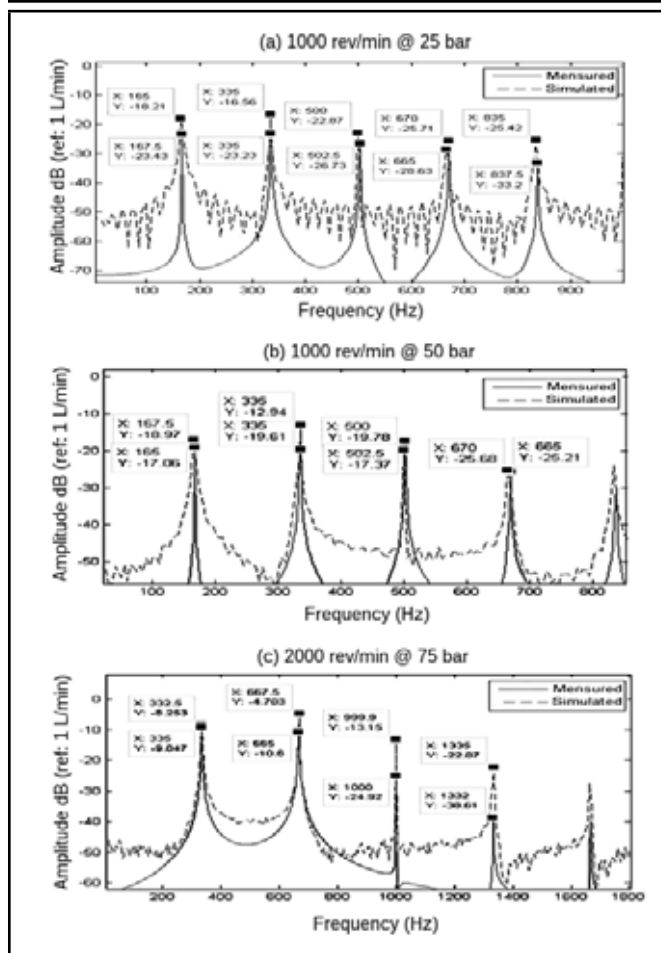1. The flow ripple caused by the under-vane flows is not null.

Figure 8. Results of the measured and simulated outlet flow ripple in the frequency-domain.

Figure 9. The simulated outlet flow without the influence of the internal leakage flows (upper plot) and the under-vane flows (lower plot), run at 1000 rpm and 50 bar.

Figure 10. The flow ripple shape, similar to a saw-tooth wave.

In fact, its contribution is very significant to the pump outlet flow ripple.

2. In Fig. 12, the upward slope is different than the downward slope. This is due to the fact that the rising and descending parabolic curve length (that, when joined, describes the cam ring suction and the discharge cam ring shape) are not the same. In other words, the intersection point of both parabolic curves is not in the middle of the suction/discharge total path.

3. Besides the triangular shape, the under-vane flow has a steady value along its curve. This is due to a pre-compression zone present in the cam ring shape.

5.3. Compressibility Effect Analysis

Although the hydraulic oil compressibility is very low, large temperature and pressure variations present in the fluid chamber during the pump operation can produce significant fluid compressibility variations. The air dissolved in the fluid is also an important factor that contributes to these variations.

The fluid compressibility affects directly the outlet pump flow ripple and its effect is better seen when the fluid chamber opens to the discharge port; at that moment, a large increase in pressure is applied to the fluid chamber causing outlet flow spills. The amplitude of these spills depends on the
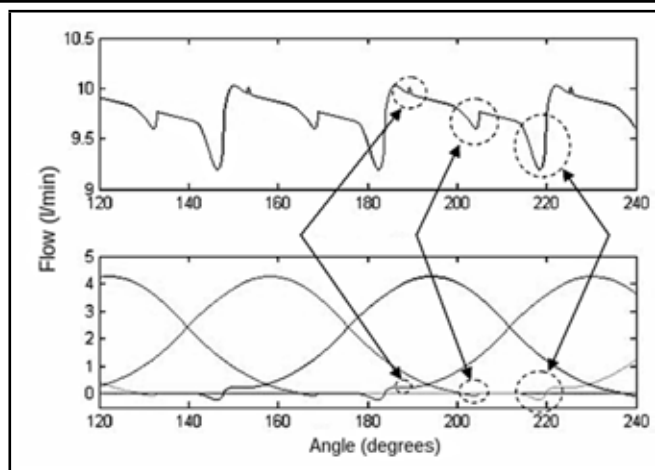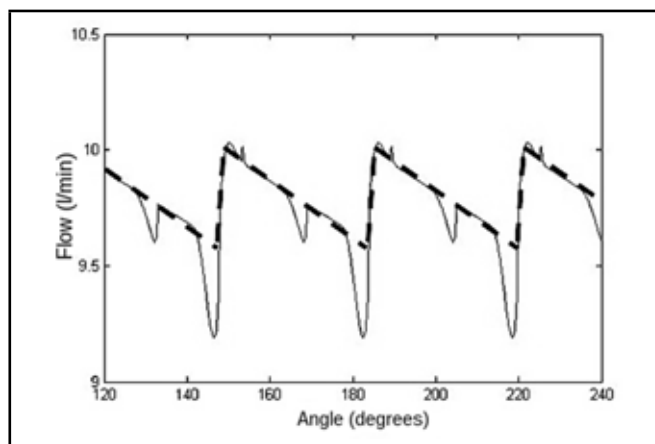
fluid compressibility that, mathematically, can be represented by the fluid effective bulk modulus (β_e).

Figure 14 shows the pump outlet flow without the leakage and the under-vane flow contributions, when the fluid effective bulk modulus is varied.

The results presented in Fig. 14 show that some spills amplitude increase when the fluid bulk modulus decreases, thus increasing the outlet flow ripple. However, other regions of the curve are not affected by the bulk modulus variation and, therefore, are not related to the fluid characteristics. These regions are shaped by the geometrical rotating group characteristics.

5.4. Internal Leakage Analysis

The rotating group internal leakage contribution has also been evaluated. Figure 15 shows the outlet flow with and without the leakage contributions. It can be observed that the overall amplitude has decreased when the leakages are taken into account, but the shape of the outlet flow remains roughly the same. In other words, the outlet flow ripple amplitude is not significantly increased when the leakages are considered even though the overall flow amplitude decreases.

These results are valid for the leakages found in the regular pump design from the regular rotating group drawing tolerances. Beyond these values, the leakage effect must be re-
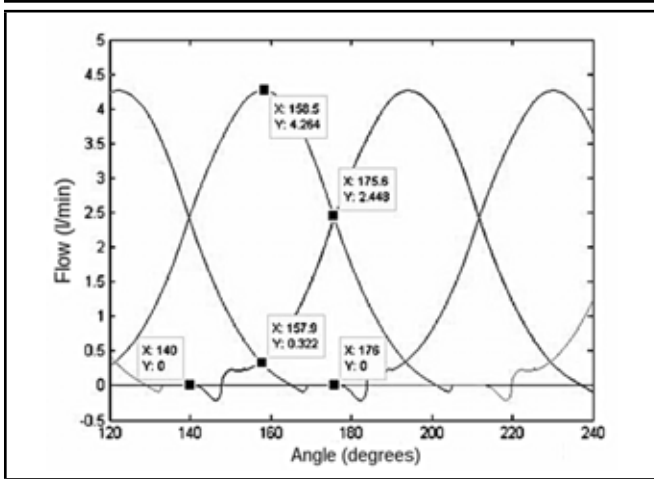
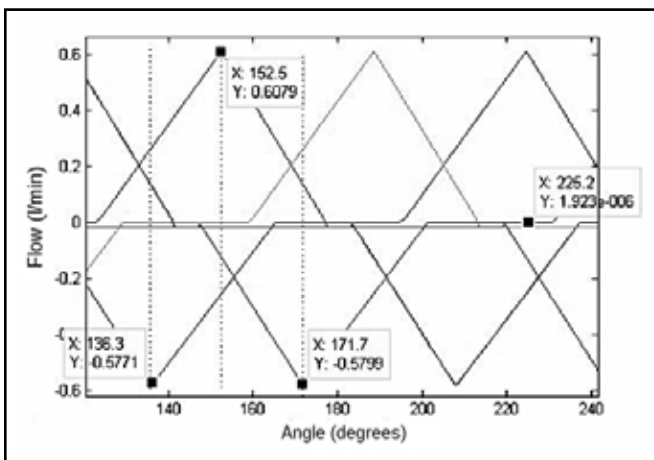**Figure 11.** Consecutive fluid chamber flows and some intersection points.

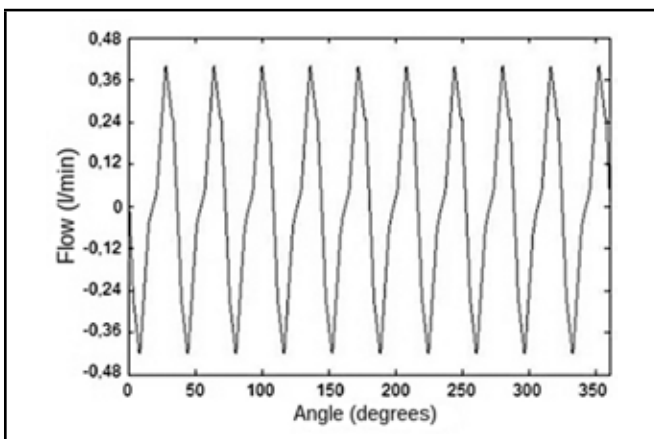**Figure 12.** The results for the flow under each of the 10 vanes.

Figure 13. The results of the total pump under-vane flow.

Figure 14. The outlet flow without leakage and the under-vane flows for different values of the fluid effective bulk modulus (1000 rpm at 50 bar).

Figure 15. The effect on the outlet flow with and without the internal leakages influence (1000 rpm at 50 bar).

viewed. Previous research[13] has shown the influence of the rotor leakage when the gap between vane and rotor slots increases beyond the drawing tolerances. In that case, the internal leakages have a large influence on the outlet flow.

6. NEW PUMP ROTATING GROUP

From the regular pump flow ripple analysis, a new rotating group design is proposed, aiming at the reduction of the outlet flow ripple amplitude. The new design is based on the following modifications:
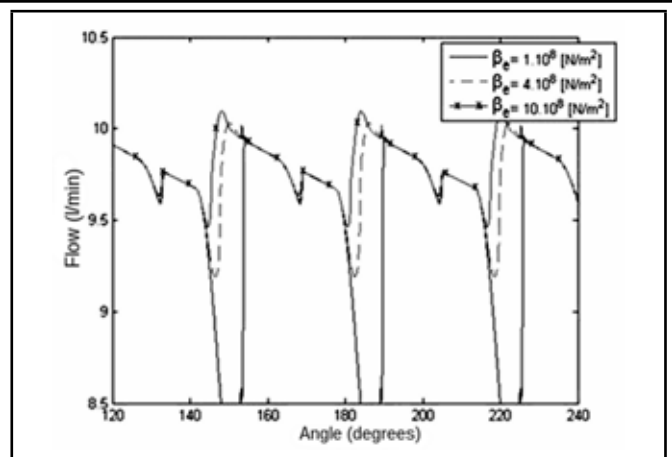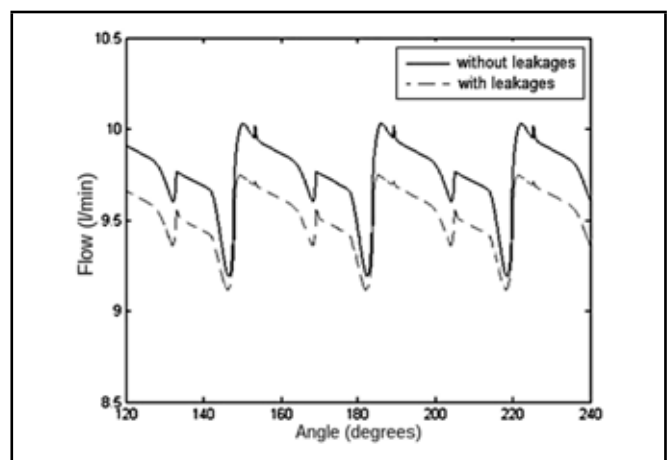
1. Rotating group for eight vanes.

2. Discharge and suction ports with same angular length found between two consecutive vanes, i.e., 360°/number of vanes. Thus, the beginning of a fluid chamber discharge flow will coincide with the maximum amplitude of a consecutive/trailing fluid chamber discharge flow, making the outlet flow, which is the sum of all fluid chamber flows, roughly steady (plane wave).

3. The intersection point of the parabolas that form the cam ring rising/decreasing shape occur in half of the length; thus, all parabolas that consist of those cam ring variations would have the same length.

4. Cam ring design modification that ensures that when a vane hits the beginning of a suction zone (first rising parabola) some other vane hits, at the same time, the beginning of a discharge zone (first decreasing parabola). In other words, the suction port opening must occur at the same time the discharge port opens. These mechanisms, working together with item 3, ensure that there always will be a pair of under-vane flows that will cancel each other, i.e., flows will have the same shape and am-
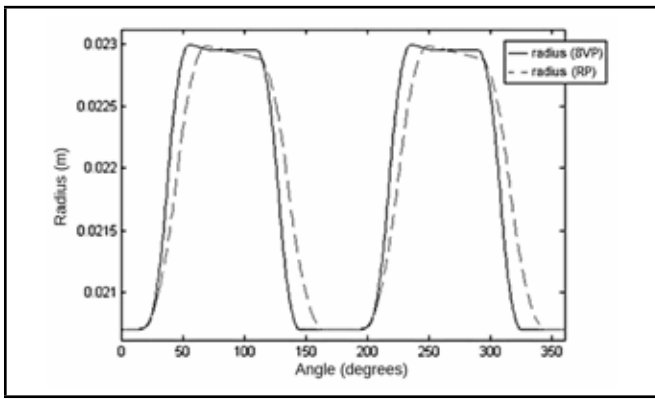
Figure 16. The cam ring profile for the regular pump (RP) and the eight-vane pump (8VP).
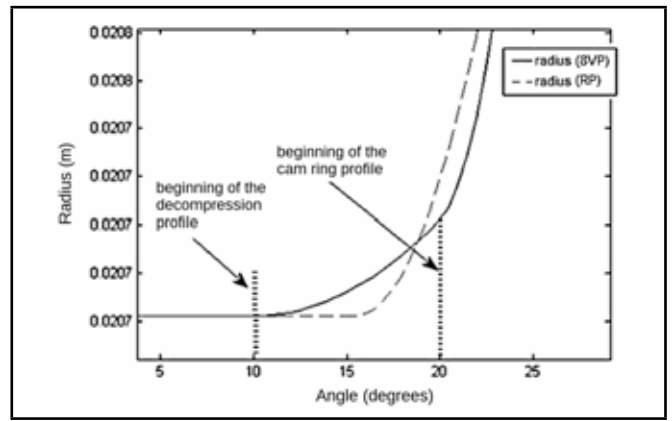

Figure 17. Details of the pre-compression zones for the regular pump and the new pump.

Figure 18. The decompression profile detailing the regular and new cam ring profile.

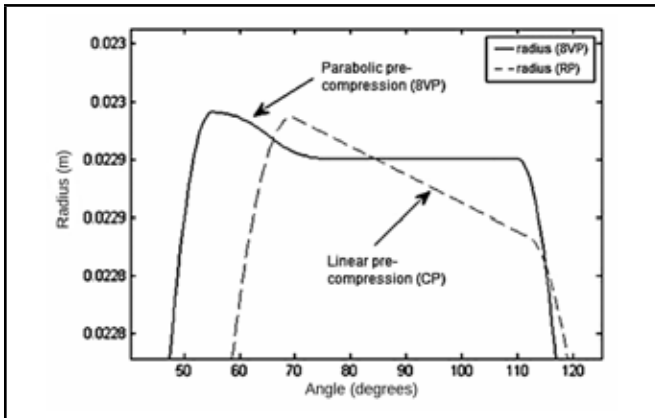**Figure 19.** The new pump outlet flow ripple showing spills caused by fluid compression effects.

plitude, but in opposite directions. Thus, the total under-vane flows, which are the sum of each under-vane flow, will be, theoretically, equal to zero.

5. To reduce the fluid compressibility effects, a parabolic pre-compression zone (formed by two parabolas, one positive and other negative) is added to the cam ring profile, positioned at the end of the suction zone. To keep the under-vane flow cancellation (as described in items 3 and 4), a parabolic decompression zone is created, formed exactly with opposite pre-compression zone parabolic shape, i.e., negative and positive, respectively, positioned at $360/N_v$ before that one. Thus, the fluid can be pre-compressed prior to the discharge port without disturbing the under-vane flow balance achieved.

It is important to say that this new pump rotation group design is independent of the number of vanes, i.e., it can be built from different number-of-vanes rotors. Thus, choosing an eight-vane rotor gives the possibility to not only reduce noise but to also decrease the pump costs.

Figure 16 shows the cam ring profiles of the regular pump (RP) and the new eight-vane pump (8VP). The differences between the pre-compression and the decompression zones, located at the beginning of the suction ports, are shown in Figs. 17 and 18, respectively.
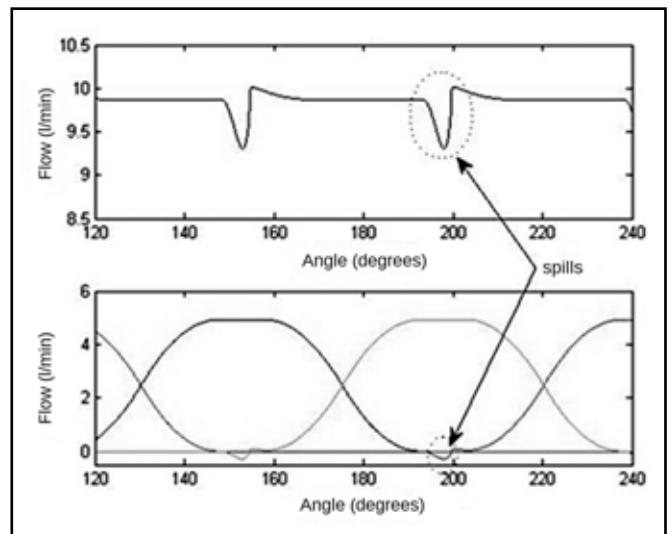
6.1. Simulation Results

As a consequence of the new rotating group timing, the outlet flow ripple became much more uniform when compared to the current pump one. Figure 19 shows the outlet flow ripple without the under-vane and leakage flows, and the fluid chamber flow packages that forms it. It can be seen that the shape of the outlet flow is planar, although some spills caused by the fluid compression effects are present. For a more realistic result, all flow ripple effects must be taken into account.

As it was discussed previously, the flow ripple caused by internal leakages does not significantly affect the overall pump outlet flow ripple. In fact, even in this new pump design, they show the same unimportant behaviour.

The new flow, under each of the eight vanes, is shown in Fig. 20. Despite very little flow appearings at the beginning of the compression zone, each under-vane flow has its corresponding equal and opposite direction flow, occurring at the same time. It leads the overall under-vane flow (sum of all of them) to be null, as shown in Fig. 21. The peaks present in that figure are just computational precision errors.

Finally, the fluid compression effect is reduced by tuning the pre-compression zone. Several simulations, with different pre-compression amplitudes (changing the slope of the parabola),
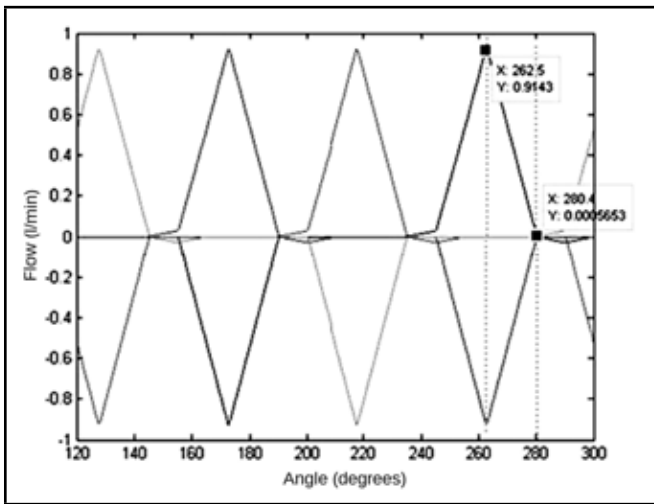
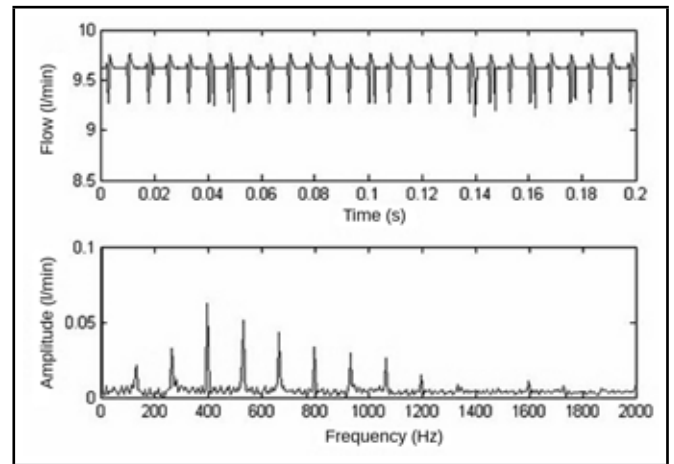**Figure 20.** The flow under each of the eight vanes in the new pump design.

Figure 21. The overall total under-vane flow.

Figure 22. The outlet flow ripple of the new pump in the time and frequency domain.

Figure 23. The harmonics amplitude reduction in the new pump design at 1000 rpm for different values of back-pressure.
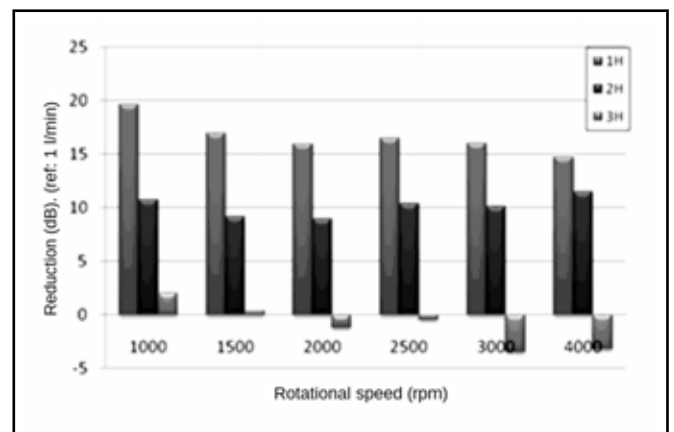
Figure 24. The harmonics amplitude reduction in the new pump design at 50 bar for different rotational speeds.
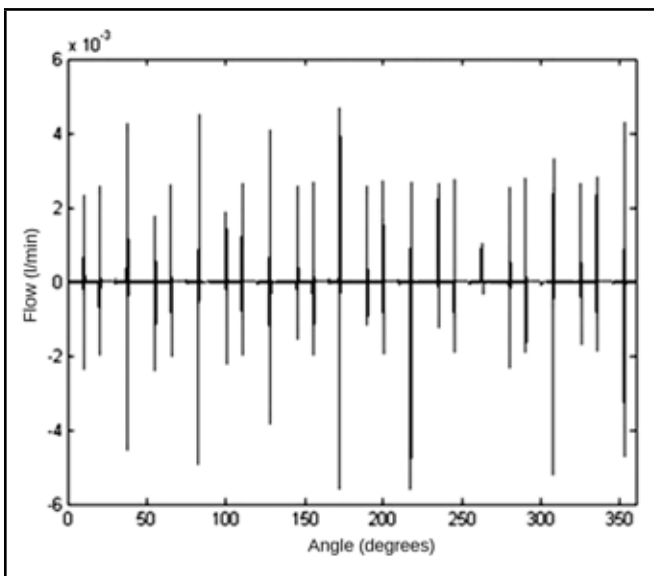
in a large range of bulk modulus values (from 4×10^8 to 14×10^8) was carried out to find the best pre-compression geometric amplitude that produces the lower fluid compression effects (lower flow spill). Once that geometrical value is found, the total outlet flow ripple could be determined. Figure 22 shows the new pump design outlet flow ripple. It can be seen that the flow ripple amplitude was drastically reduced when comparing it with the regular pump one (see Fig. 4).

From the spectral analysis, it can be seen that the new design reduces significantly the outlet flow ripple harmonics amplitude, mainly the lower harmonics, and changes the regular pump frequency pattern. In other words, all the noise harmonic content was shifted down in frequency. This effect, together with the harmonic amplitude reduction, can lead to a significant reduction in the noise observed inside the car.

Figures 23 and 24 show the simulated new pump reduction (in dB) when compared with the regular pump results. Figure 23 shows the results by keeping the rotational speed at 1000 rpm and varying the back-pressure. In Fig. 24, the results are presented, keeping the back-pressure at 50 bar and varying the rotational speed.

From the figures, we can observe that the best reduction is achieved when the new pump design is run at 1000 rpm at 50 bar, given an approximate value of flow ripple reduction of 20 dB, 12 dB, and 2 dB at the first (1H), second (2H), and third (3H) harmonic, respectively.

Finally, Figs. 25 and 26 show the details of the proposed new rotating group design.
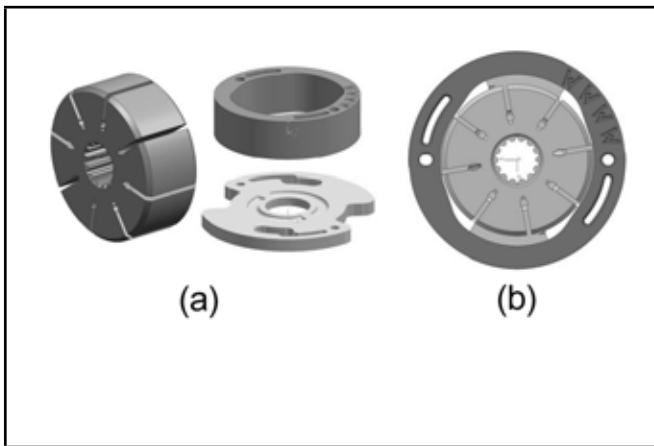
Figure 25. The details of the proposed new rotating group design: a) components, including rotor, cam ring, and thrust plate; and b) assembly.
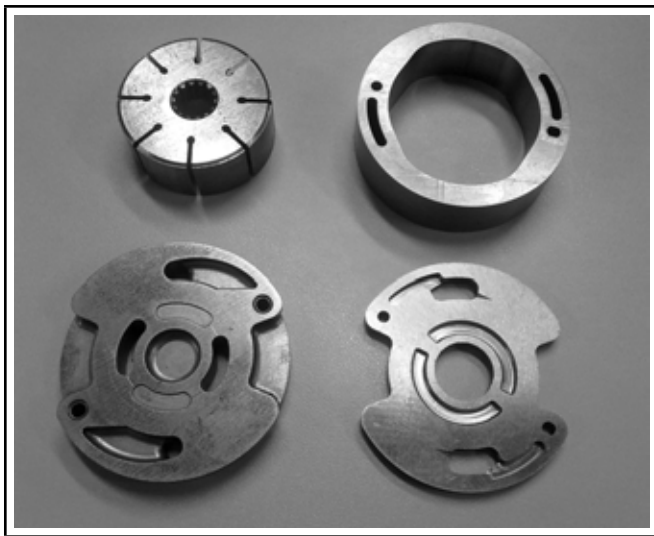
Figure 26. Photograph showing the components of the proposed new pump rotating group.

7. CONCLUSIONS

This work has shown a method to calculate and predict the outlet flow in an automotive positive displacement pump. Additionally, it has presented an experimental method (the secondary source method) to rate the pump flow ripple that was used to validate the numerical results. The main aspects of the pump flow ripple formation were considered and, from this analysis, a new rotating group design has been proposed aiming at the pump outlet flow ripple reduction.

The new rotating group design was simulated and its results were compared with the regular pump ones. The results have shown an excellent outlet flow ripple reduction in a wide range of pump operational conditions. The greatest reduction was achieved for 1000 rpm at 50 bar of back-pressure operational conditions, where the moan noise is perceived[13] to reach almost 20 dB of flow ripple reduction at the first harmonic, and over 10 dB at the second harmonic.

REFERENCES

[1] Zanetti-Rocha, L., Johnston, D.N. and Gerges, S.N.Y. Flow ripple reduction in power steering hydraulic pumps, *Proc. Fluid Power and Motion Control 2010*, Bath, (2010).

[2] Gerges, S.N.Y., Johnston, D.N. and Rocha, L.Z. Noise and vibration in fluid power systems, *Handbook of Hydraulic Fluid Technology*, Taylor & Francis Group, Florida, (2010).

[3] Skaistis, S. *Noise Control of Hydraulic Machinery*, Marcel Dekker, New York, (1988).

[4] Johnston, D.N. Measurement and prediction of the fluid borne noise characteristics of hydraulic components and systems, PhD Thesis, University of Bath, (1987).

[5] Edge, K.A. and Johnston, D.N. The "secondary source" method for the measurement of pump pressure ripple characteristics, part 2: experimental results, *Proc. Inst. Mech. Engrs.—part A*, **204**(1), 41–46, (1990).

[6] ISO 10767-1, Hydraulic fluid power- determination of pressure ripple levels generated in systems and components— part 1: precision method for pumps, International Standardization Organization, Geneva, (1996).

[7] Dickinson A.L., Edge, K.A. and Johnston, D.N. Measurement and prediction of power steering vane pump fluid-borne noise, *SAE Transactions - Journal of Passenger Cars*, **102**(6), 1753–1761, (1993).

[8] Chalu, C. Torque fluctuations and vibrations in a vane pump, Master of Philosophy Thesis, University of Bath, (2004).

[9] Yang, M. Modelling and analysis of pressure pulsations in hydraulic components and systems with particular reference to pump fault diagnosis, PhD Thesis, University of Bath, (2009).

[10] Edge, K.A. and Johnston, D.N. The "secondary source" method for the measurement of pump pressure ripple characteristics, part 1: description of method, *Proc. Inst. Mech. Engrs.—part A*, **204**(1), 33–40, (1990).

[11] BS 6335:1990, *Methods for determining pressure ripple levels generated in hydraulic fluid power systems and components, part 1: secondary source methods for pumps*, British Standards Institution, London, (1990).

[12] Johnston, D.N., Drew, J.E. Measurement of positive displacement pump flow ripple and impedance, *Proc. Inst. Mech. Engrs.—Part I*, **210**(1), 65–74, (1996).

[13] Rocha, L.Z., Paul, S., Jordan, R. and Gerges, S.N.Y. Sound quality evaluations of hydraulic pumps, SAE paper 2008-36-0583, So Paulo, Brazil, (2008).

Min Zhu received a BSc degree from East China Normal University, China, in 1983, and received a PhD degree from Akita Prefectural University, Japan, in 2013. She was a visiting researcher in Akita Prefectural University, Japan from 2008. Currently, she is an associate professor at East China Normal University, China. Her main research interests include blind signal processing, active noise control, adaptive control algorithms, intelligent computing, and intelligent systems.
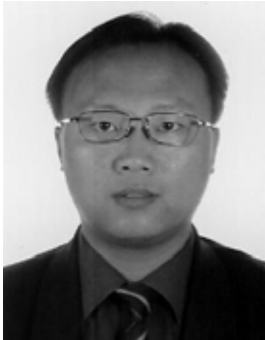
Huigang Wang received an MSc degree in Underwater Acoustic Engineering and PhD degree in Signal and Information Processing from Northwestern Polytechnical University (NPU), Xian, China, in 1999 and 2002, respectively. Currently, he is a professor at NPU, an IEEE member, and a member of the Acoustic Society of America. His main research interests include blind signal processing, array signal processing, and active noise control. He was a research fellow at Akita Prefectural University in 2004, 2005 and 2011.

Guoyue Chen received a BSc degree from East China Normal University, China, in 1983, where he worked as a research assistant in the Department of Computer Science until 1989. He received his MS and PhD degrees from Tohoku University, Japan, in 1993 and 1996, respectively. He worked as a research assistant in Tohoku University until 1999. He is presently a professor at Akita Prefectural University, Japan. His research interests include digital signal processing and its applications to active noise control, adaptive control algorithms, image processing, and medical image processing.

Kenji Muto received BE and ME degrees from Shibaura Institute of Technology, Japan, in 1991 and 1993, respectively, and received PhD degree from Tohoku University, Japan, in 1999. He was a research associate at the Tokyo Metropolitan College of Aeronautical Engineering beginning in 1993, where he was promoted to lecturer and associate professor in 1997 and 2000, respectively. In 2009, he joined the faculty of the Department of Communications Engineering, in the College of Engineering, at the Shibaura Institute of Technology, Japan, as an associate professor. His research interests include adaptive control and acoustic noise analysis.

Shishir Kumar Sahu received his undergraduate engineering degree in civil engineering from UCE, Burla, Sambalpur University, India. After earning his PhD from IIT, Kharagpur, on an MHRD fellowship, he completed post-doctoral research at the Institute of Sound and Vibration, Southampton University, UK, during 2007, on a British Council fellowship. He is now working as dean at the Planning & Development of the National Institute of Technology in Rourkela, India, and as a professor in the Department of Civil Engineering. His industrial experience includes the works department of the Government of Orissa and Indian Railways. He is the author of 50 research papers, including twenty five publications in reputed international journals. His research interests include structural dynamics, fracture mechanics, structural health monitoring, the stability of plate and shell structures, composite materials, and finite-element methods.

About the Authors

Uttam Kumar Mishra did his undergraduate programme in civil engineering at IGIT Sarang, Talcher, Odisha, and his postgraduate work in structural engineering at NIT Rourkela, India. He is presently working at NIT Rourkela as an assistant professor in the Department of Civil Engineering. He teaches engineering mechanics, engineering drawing, graphics, statics, mechanics of solids, and laboratory classes. His subjects of interest include vibration, buckling, the dynamic stability of structural members, finite element methods, and artificial neural networks. His research focuses on structural dynamics, fracture mechanics, structural health monitoring, and the stability of structural members.

Georges Kouroussis has held a masters degree in mechanical engineering from the Faculty of Engineering of Mons, Belgium, since June 2002. He earned a PhD in applied sciences on vibratory nuisances of ground vibrations in May 2009. He currently works as an assistant professor in the Department of Theoretical Mechanics, Dynamics, and Vibrations at the University of Mons. He takes part in the theoretical mechanics and dynamics labs, exercises, and courses. His research interests include railway-induced ground vibrations, geotechnical testing and engineering, dynamic analysis of complex structures, and vibration signal processing.

Laurent Van Parys has held a masters degree in architectural engineering from the Faculty of Engineering of Mons, Belgium, since June 2001. He also holds a PhD in applied sciences on structural assessment of masonry structures, earned in February 2008. He currently works as an associate professor in the Department of Civil Engineering and Structural Mechanics at the University of Mons, where he is responsible for teaching activities in soil mechanics and geotechnical engineering. His research interests concern geomaterial characterization and soil-structure interactions, namely in heritage conservation and retrofitting problems.

Calogero Conti earned a degree at the Faculty of Engineering of Mons, Belgium, where he graduated in 1978 as an engineer in metallurgy. After presenting a PhD dissertation in 1983 in the field of aluminium metallurgy, he became a Doctor of Applied Sciences. Professor Conti is today a full professor of theoretical mechanics and dynamics at the University of Mons. He is also the author of numerous articles in professional and academic journals and conference proceedings. Since 2009, he has held the position of Rector of the University of Mons.

Olivier Verlinden obtained a masters degree in mechanical engineering in 1988 and a PhD in applied sciences in 1994, both at the Faculty of Engineering of Mons, in Belgium. His research initially related to the numerical simulation of flexible multibody systems, naturally expanded to the simulation of biomechanical or mechatronic systems, and now extends to the education of multibody system simulation. He is presently a full professor and head of the Department of Theoretical Mechanics, Dynamics, and Vibration at the University of Mons.

About the Authors

Hamed Moradi received his BS in mechanical engineering in solid mechanics from Amirkabir University of Technology in 2005. He went on to earn his MS and PhD in mechanical engineering in applied mechanics from Sharif University of Technology (SUT) in Tehran, Iran, in 2008 and 2012, respectively. Currently, he is the post-doctoral associate at SUT, working on optimal nonlinear control of process in mechanical systems and installations to reduce energy consumption. From 20082012, he was the youngest invited faculty member in the Department of Mechanical Engineering at Hormozgan National University in Bandar-Abbas, Iran. His current research interests include modeling of dynamic systems; application of robust, nonlinear, and optimal control methods in various dynamics systems (such as manufacturing); bio-engineering; thermo-fluid industrial processes; and power plant engineering.

Gholamreza Vossoughi received his PhD from the Mechanical Engineering Department at the University of Minnesota, USA, in 1992. Since then, he has been a faculty member of the Mechanical Engineering Department at Sharif University of Technology. He has served as the Manufacturing Engineering and Applied Mechanics Division Directors from 19941998, and as the Graduate Dean of Mechanical Engineering from 19992003. He has also served as the founder/director of the Mechatronics Engineering Program at both Sharif's Main campus and Sharif's International Campus at Kish Island, beginning in 2004.

Firooz Bakhtiari-Nejad received BS degrees in electrical engineering and mechanical engineering in 1975, an MS degree in mechanical engineering in 1978, and a PhD in engineering in 1983, all from Kansas State University, USA. He was an assistant professor in the Department of Mechanical Engineering at Kerman University in Kerman, Iran, from 19831988, an associate professor from 19982004, and then professor of Mechanical Engineering from 2004 to present at Amirkabir University of Technology (AUT) in Tehran, Iran. He also was the director of research affairs and the secretary general of centers of excellence console for the Ministry of Science, Research, and Technology of Iran, from 20052010. His current research interests are the application of theoretical and experimental modal analysis for control and health monitoring of systems and structures; digital control and adaptive optimal control of continuous structures and multi variable systems, such as internal combustion engines and vehicle dynamics; and application of fuzzy and neural controls in mechanical systems.

M. T. Ahmadian received his BS and MS degrees in physics during 1972 from Shiraz University in Shiraz, Iran. He completed the requirements and earned his BS and MS degrees in mechanical engineering in 1980 from the University of Kansas, located in Lawrence, Kansas, USA. At the same time he completed his masters degree, he received a PhD in physics and a PhD in mechanical engineering in 1981, and 1986, respectively. These were also completed at the University of Kansas. His research interests are micro and nano mechanics, as well as bioengineering.

About the Authors

Ashkan Haji Hosseinloo is currently a research associate at Nanyang Technological University (NTU). He received his BS and MS from Amirkabir University of Technology (AUT) and NTU, respectively, in 2009 and 2012, both with first class honors with distinction. His research interests include random and nonlinear vibration; shock and vibration control using passive, semi-active, and active techniques; vehicle dynamics; and optimal control. He has published 8 journal and conference articles. He is a member of American Society of Mechanical Engineers (ASME) and Society of Photo-Optical Instrumentation Engineers (SPIE).

Nader Vahdati joined the Petroleum Institute (PI) in 2010, as an Associate Professor and Deputy Chair of the Department of Mechanical Engineering. He received his BS (Magna Cum Laude) and MS in mechanical engineering from the University of Portland, Oregon. In 1989, he graduated from the University of California, Davis, with a PhD in mechanical engineering with a specialization in dynamic systems and controls. Prior to joining the PI, he was an associate professor at Nanyang Technological University (NTU) in Singapore, and worked for the Lord Corporation, an aerospace and automotive company in Erie, Pennsylvania. His research interests include active and semi-active vibration and noise control using advance suspension systems, hard disk drive dynamic modeling, energy harvesters, and storage technology. He has published over 54 journal and conference articles. He is a member of American Society of Mechanical Engineers (ASME), and Society of Automotive Engineers (SAE).

Fook Fah Yap is currently an associate professor at Nanyang Technological University (NTU), a visiting professor at the University of Washington, and manager of the Centre for Mechanics of Micro-Systems at NTU. He received his BA (first class with distinction) and PhD from the University of Cambridge, UK, in 1989 and 1994, respectively. His main research interests are mechanics of micro-systems, in particular the dynamic analysis of multi-component systems for high capacity; high speed data storage; dynamics of damped structures and vibration control using MRF damping technology; and virtual prototyping and simulation of complex mechanical systems. He joined NTU in 1994 where he has published more than 50 journal and conference articles, written two books, and conducted more than 15 research projects. He is a member of American Society of Mechanical Engineers (ASME).

Leonardo Zanetti-Rocha obtained his bachelors degree in electrical engineering in 1999 and his master degree in mechanical engineering in 2004, researching room acoustics and audio systems. He obtained a doctoral degree in mechanical engineering in 2012, doing research on automotive, hydraulic, pump, fluid-borne, noise reduction. He worked for one year as visiting researcher at the Centre for Power Transmission and Motion Control, at the University of Bath/UK, during his doctoral studies. He has eight years of experience in the automotive industry, working as a product development engineer, project leader, and NVH internal/external consultant with clients such as Fiat, Ford, GM, Renault. Currently, he is an adjunct professor at the Taquary Valley University in Brazil, as well as a visiting professor at two universities. He has published several papers on fluid-borne noise reduction, room acoustics, and automotive sound quality. His current research interests include experimental and numerical pump fluid-borne noise analysis, conditioned-based maintenance using vibration analysis, and air- and structural-borne noise isolation/control in buildings.

Samir Gerges obtained his bachelors degree in mechanical/aeronautical engineering from Cairo University in 1964, and his masters in 1970. He obtained his doctorate from ISVR, Southampton University, UK, in 1974. He has been a professor on noise and vibration since 1978 at the Federal University of Santa Catarina (UFSC), Brazil. His current interests include industrial and construction noise, hearing protectors, experimental and numerical vibro-acoustics analysis for industrial and vehicle applications, and general room acoustics. He was the founder of the Industrial Noise Lab (LARI) at UFSC, a founding member of the Brazilian Acoustical Society (SOBRAC), and has also served as the president of SOBRAC. He is a member of the IIAV Board of Directors, an IIAV Fellow member, and an ASA Fellow. Dr. Gerges is also a member of the editorial board of the *Journal of Building Acoustics*, the *Journal of Noise Control Engineering*, and the *International Journal of Acoustics and Vibration*. From 2007–2010, he was the President of ICA. He has coordinated several technical research projects on NVH and sound quality for Ford, GM, Embraer, and Fiat, among others. He has more than 320 papers published in journals and congresses.

Nigel Johnston is a Senior Lecturer of Mechanical Engineering at the University of Bath, UK. He specialises in the areas of fluid-borne noise measurement and reduction in hydraulic fluid power systems, active noise control, numerical modelling of hydraulic components, unsteady turbulent flow, and pipeline and hose dynamics. Dr. Johnston has over 25 years of experience in hydraulic fluid power research and teaching. He obtained his PhD for research into fluid-borne noise characteristics of hydraulic systems. This work has since been used as the basis for an ISO standard for the measurement of pump pressure ripple characteristics. He has published about 70 refereed journal and conference papers and has collaborated with several companies, including Delphi Steering Systems, General Motors, Airbus, John Deere, Sun Hydraulics, Parker Hannifin, and BMW. He regularly teaches industrial fluid power courses in the UK, Europe, and USA. He is organiser and joint editor for the Bath/ASME International Fluid Power and Motion Control Symposium.

Jorge Arenas received a bachelors in acoustical engineering in 1988 and a masters in physics in 1996, both from the Universidad of Austral, Chile. In 2001, he obtained a PhD in Mechanical Engineering from Auburn University in the USA. Dr. Arenas was one of the recipients of the 2000 Harry Merriwether Fellowship at Auburn University. Currently, he is the director of the Institute of Acoustics and chair of the graduate program in engineering at the Universidad Austral. He has also been a visiting lecturer at several universities in Spain, Mexico, and Brazil. In addition, he has been actively co-operating as a consultant with industry and he has published several technical articles in international congresses and journals. Dr. Arenas is a member of the International Institute of Acoustics and Vibration (IIAV) and the Acoustical Society of America (ASA). In ASA, he has served as a member of the Technical Committee on Noise for several occasions. He is a member of the editorial boards of three journals, including the *International Journal of Acoustics and Vibration*. He has been a member of the scientific, organizing, and international advisory committee of several international congresses, including ICSV, Internoise, and FIA (Iberoamerican Federation of Acoustics). He has also served as a member of the Board of Directors for the IIAV and is currently serving as the Vice President for Communications for the IIAV.

Book Reviews

Digital Sonar Design in Underwater Acoustics - Principles and Applications

I chose to review this book out of curiosity into the Chinese perspective on sonar and underwater acoustics - all my previous reading being of work by US and European authors. Furthermore, the contents list of this book promises a comprehensive approach to the subject, covering all pertinent aspects.

From the outset this book is targeted at those involved in engineering sonar systems rather than those seeking an understanding of underwater acoustics. The first figure is a block diagram of a sonar system. The advent of computer technology and digital signal processing hardware is introduced alongside a detailed explanation of its impact on the practical implementation of sonar system design.

The book introduces the process of conversion of analogue signals into digital values in the first chapter then returns to the topic in several subsequent chapters to show how this basic engineering aspect affects design decisions. At the other end of the system, the display of sonar data is also introduced at a conceptual level then returned to in progressively more detail to the extent of mathematical expressions relating the limitations of screen dynamic range to system performance. Another recurring theme is the beam-forming process which is introduced in terms of geometry with progressively more detail in terms of engineering implementation options and consequences in terms of performance and robustness. There is some discussion of the science of underwater acoustics, but this is limited to that necessary to understanding the impact on sonar engineering design decisions.

A further example of the engineering perspective is the extensive conceptual discussion and mathematical analysis of component failure and system reliability. The exploration of this topic is evidence of the practical attitude towards sonar design that characterizes this book. The consideration of simulation techniques for system proving enhances the value of this book to those involved in system design.

Unfortunately, this book contains some obvious errors. For example on page 27 we have $60 \times 10 - 1.24 = 58.76$ and on page 178 the units of voltage and pressure are jumbled such that a voltage is quoted in micro Pascal rather than micro Volts. On page 203 the labelling of the sub-plots in Figure 4.43 appears to have been transposed, confusing longitudinal with transverse waves. I noticed some other inconsistencies whilst reading the book, but I have not produced an "erratum sheet". My concern is that there might also be errors in the more advanced formulae that are not immediately obvious. Hence I would seek to verify any formula before using it in a practical sonar implementation.

In summary this book will be of particular benefit to those involved in the design and procurement of sonar systems. The exploration of the impact of practical engineering issues on sonar performance also renders it a valuable supplement to the books used by those conducting research in sonar performance modelling and underwater acoustics. The curiosity that attracted me to this book has been replaced by a recognition that the author has provided me with a set of useful approaches to understanding basic sonar engineering issues.

Adrian Brown
Naval Systems Department
Defence Science and Technology Laboratory
United Kingdom

Noise Mapping in the EU: Models and Procedures

After the "Proposal for a Directive of the European Parliament and of the Council relating to the Assessment and Management of Environmental Noise COM (2000)468", the "Environmental Noise Directive 2002/49/EC" related to the assessment and management of environmental noise was adopted on 25 June 2002.

The European Noise Directive, usually known as the "END", defines the concept of "strategic noise map" as "a map designed for the global assessment of
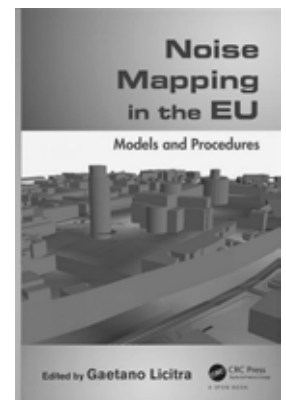
noise exposure in a given area due to different noise sources or for overall predictions for such an area" and requires competent authorities in EU Member States to produce strategic noise maps in their main cities for areas with the main noise sources (roads, rails, airports, harbours, industries, etc...).

The basic principles of the Directive (monitoring the environmental problem, informing and consulting the public, addressing local noise issues and developing a long-term EU strategy) are for the first time deeply discussed and analyzed in the five sections of this book, which also acts as guide for students, researchers and technicians who want to approach the topic for the first time or are already involved in it.

There is an impressive number of information in this book, ranging from the fundamental of the problem to the measurements methods, from the legislative aspects to the software simulations and their quality.

The editor along with the co-authors explained the role of European Commission's Working Group - Assessment of Exposure to Noise (WG-AEN) and its Good Practice Guide for Strategic Noise Mapping and the Production of Associated Data on Noise Exposure (GPG version 2). They also examined in depth the support that geographic information system can give to the noise mapping topic.

The book consists lots of examples, recommendations, and experiences reported from the authors of the various chapters who are experts coming from various professional fields and countries. It represents a sort of summary of the current "state of the art" in the field of noise mapping in the EU, and also gives a brief outlook on future plans and expectations.

The information is well documented and explained, also it is quite clear (for example for the technical nature of the first chapter) that the intended audience is of course more researchers and experts in the field rather than casual readers (e.g. politicians or administrators) interested in the topic. Nevertheless, taking apart from the most markedly scientific aspects, reading proves to be interesting and fruitful for readers coming from other cultural areas, who would by the way find useful an alphabetical list of the acronyms used within the text.

If a remark can be done, apart from the obvious observation regarding inaccuracies in citations and figure captions which are absolutely normal in a first edition, is the limited amount of information specifically regarding harbour noise. This is usually assimilated to the industrial one (as in the book), but recent studies and European Projects, for example EcoPorts, NoME-Ports, SIMPYC and the recently completed SILENV (Ships oriented Innovative solutions to reduce Noise and Vibrations) are focusing on this specific topic and aim to define guidelines in order to characterize the noise due to harbours on the basis of the European Directive 2002/49/EC. In the same projects, efforts have also been made to model a ship as a noise source, which is not a simple task because of the complexity of the ship's geometry and the difficulty in the characterization of the onboard sources which strongly increases the difficulty of the

modeling. These topics are likely to be treated in a second edition, which will probably also include information about what it has been done and which new results have been achieved during the time elapsed between the two editions.

In conclusion, the book is highly recommended, and for its uniqueness in the current editorial overview it can be seen as a "must have" for almost every academic and/or technical library.

Davide Borelli
Mechanical Engineering, Energy, Management and Transports Department
Polytechnic School
Università degli Studi di Genova

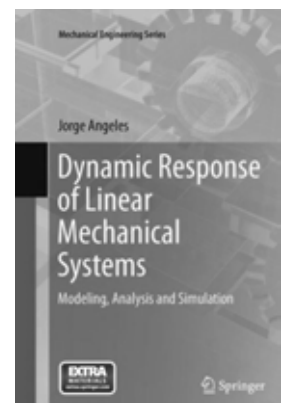# Dynamic Response of Linear Mechanical Systems: Modeling, Analysis and Simulation

The book discusses the modeling, analysis, and simulation of mechanical systems from the point of view of their dynamic response. The book is divided into eight chapters. Each chapter contains many examples (very carefully selected) and ends with a set of exercises. For this reason the book may be used as a support material for lecture courses as well.

The first three chapters are devoted to the modeling, response, and simulation of single degree of freedom (dof) systems. The first chapter presents the modeling of a single-dof mechanical systems using springs and dashpots, and then performs the analysis of the planar motions using the Newton-Euler and Lagrange equations. This chapter also describes the notions of hysteretic and Coulomb damping, equilibrium positions, and linearization about the equilibrium positions for linear time-invariant systems. The author presents a seven-step procedure for the modeling. Various examples are introduced for a better understanding of such a pro-

Book Reviews

cedure. In the second chapter, called "Time Response of First- and Second-order Dynamical Systems", the author treats zero-input and zero-state responses of linear time-invariant systems without and with damping. Further on, the author presents the analysis of the response in the case of abrupt and impulsive inputs and then evaluates the total time response. The last three sections of this chapter cover the harmonic and periodical responses using Fourier transformation, and the time response of the systems with dry friction. Chapter Three discusses the zero-order hold and simulations of first- and second-order systems (without and with damping).

The second half of the book is on multi-dof and continuous systems. Chapter Four is on the modeling of multi-dof linear systems. This chapter presents derivations of the equations of motion using Lagrangian formalism and the seven-step procedure described previously. It then linearizes the equations of motion about the equilibrium positions, and also studies the systems with rigid modes. Chapter Five is devoted to the vibration analysis of two-dof systems. This chapter starts with the derivation of natural frequencies and mode shapes using linear algebra and Mohr's circle methods. Next, it discusses zero-input and zero-state responses, and then the total responses for undamped and damped systems. The beat phenomenon, the classical modal method, and semi-definite and definite systems are also discussed. Chapter Six extends the vibration analysis to n-dof systems using almost the same structure as Chapter Five. Chapter Seven is on the simulation of n-dof systems in terms of the discrete-time responses of undamped and damped linear systems. The last chapter titled "Vibration Analysis of Continuous Systems" presents a set of examples of this kind for which the author presents the mathematical modeling, discusses the natural frequencies and modes and the properties of the eigenfunctions.

The book may be regarded as:

  i) an introduction to the theory of vibration (in which case the reader would use only the Chapters 1, 2, 3 and 5);

 ii) a textbook of vibrations (the reader would study all the chapters);

iii) supplementary material for other courses like linear mechanical analysis;

 iv) a connection between the theory of vibrations and the theory of dynamical systems, etc.

The author uses the properties of the linear systems of differential equation to derive the solutions by means of the superposition principle. Sometimes this approach is quite complicated and the readers need to have knowledge learned in courses on elementary theory of differential equations. Also, as the author uses the Lagrangian formalism to derive the equations of motion he assumes that the readers understand analytical mechanics. The book is very useful for mechanical engineering students of all levels from undergraduate to PhD.

Nicolae-Doru Stanescu
University of Pitesti, Romania